SAPIENZA
UNIVERSITÀ DI ROMA

DOTTORATO DI RICERCA IN SCIENZA DEI MATERIALI -
XXVI CICLO

Size-Dependent Properties of Iron Oxide Nanowires for Lithium Ion Batteries:

Morphological and Spectroscopical Characterization

CANDIDATE: MARCO ANGELUCCI

Supervisor

Prof. Carlo Mariani

PhD School Coordinator

Prof. Carlo Mariani

September 8, 2014

Dedica

Contents

Introduction

The present energy policy, still mainly based on burning of fossil fuels, inevitably poses a serious concern due to the CO_2-related global warming. Accordingly, efforts aimed to assure an efficient use of renewable energy sources, as well as the replacement of internal combustion engines with electric motors for the development of sustainable vehicles, such as hybrid vehicles (HVEs) and ultimately, full electric vehicles (EVs), are in progress worldwide.[1] The exploitation of alternative and green energy sources, such as solar, wind and geothermal, requires the side support of energy storage systems that can compensate their intermittent characteristic. It is now generally accepted that among the various possible choices, the most suitable are electrochemical batteries, namely portable devices capable to deliver the stored chemical energy as electrical energy with high conversion efficiency and without any gaseous emission. Particularly, rechargeable batteries, benefiting by high specific energy (high voltage joined with high specific capacity), high rate capability, high safety and low cost, offer the most promising option to support renewable energy plants, as well as to efficiently powered HVEs or EVs. Promising candidates are Li-ion batteries that, thanks to the high value of energy density, today exceed at least by a factor of 2.5 any competing technology.[2,3] These unique features make lithium-ion batteries the power sources of choice for the portable electronic market (including popular products such as cellular phone, lap-top computers, mp3's, as well as power tools) with an annual production amounts to several millions of units. In the most conventional configuration, a lithium battery is formed by a graphite anode, acting as a "lithium sink" negative electrode to accept and release back lithium ions provided by a "lithium source" transition metal oxide, *e.g.* lithium cobalt oxide positive electrode (cathode) and a liquid organic solution as electrolyte.[2] In charge, lithium ions, removed from the $LiCoO_2$ positive electrode,

travel through the electrolyte and reach the negative electrode where they are intercalated into the graphite structure. To compensate the transfer of the ionic charges, electrons are also exchanged between the two electrodes. Due to this reaction mechanism that involves transfer of lithium ions only, these electrochemical storage systems are called "lithium ion batteries".

The new trend in the field is that of moving from consumer electronics to electromobility by using lithium batteries for powering the electric engine of hybrid and/or electric sustainable vehicles. However, the present Li-ion batteries, although commercial realities, are not yet at such a technological level to meet the requirements of these vehicles, whose production is in fact still limited to few demonstration prototypes, mainly of the hybrid type. An effective evolution of the HVE and EV market requires the availability of batteries having lower cost, higher safety level and, especially, higher energy density, than those of the present ones. This important step forward may be obtained only by moving to new chemistries. In this respect, very promising anode materials alternative to graphite are transition-metal oxides, based on the conversion reaction with lithium,[4,5] not only for their natural abundance and non-toxicity, but primarily because they are expected to have a much higher specific capacity than conventional graphite anodes.[6] The conversion mechanism involves the exchange of more than one electron for redox center, thus allowing a higher specific capacity and energy density in comparison with the conventional electrodes based on lithium ions intercalation/deintercalation.

Among the transition metal oxides, Iron (III) oxide Fe_2O_3 is attracting an increasing interest, not only for its good electrochemical properties (theoretical specific capacity is about 1007 mAh/g) but also because it represents a low-cost and eco-sustainable material.[6]

In lithium cell, Fe_2O_3 electrode reacts through a complex mechanism consisting in the progressive intercalation of lithium ions in the three- dimensional electrode structure and, subsequently, in the conversion of Fe_2O_3 to metal Fe and Li_2O. The Fe_2O_3 electrochemical reaction can be described by the following steps[7]:

$$Fe_2O_3 + 6Li \leftrightarrows 2Fe + 3Li_2O + 6e^-$$
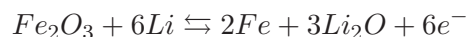
The overall electrochemical process implies the exchange of 6 electrons for

redox center and, therefore, a value of specific capacity much higher than the one shown by conventional anodes. However, Fe_2O_3 and other conversion electrodes are still far from being implemented as anodes in lithium ion batteries due to several problems limiting their performances in practical cells[8]. Structural reorganization experienced by the electrode during conversion reaction leads to de-cohesion and segregation of the Fe and Li_2O phases and, in the worst cases, to the pulverization of the electrode. This issue implies unsatisfactory charge-discharge efficiency of the cell and low capacity retention over cycling. In order to overcome these limits and make the transition metal oxide a viable electrode for lithium ion battery application many efforts have been recently made, mainly within the material engineering research field.

Research is focusing on developing nanostructured systems that can make even more stable and efficient batteries, optimizing the rate capability, limited by transport of both lithium ions and electrons at the electrodes. Size and shape of iron-oxide particles can induce different capacity and cycling lifetimes.[7,9–12] Fundamental factors that affect the capacity of lithium batteries are the exchange surface and the mean free path of the electrons traveling in the compound. In particular, nanostructured Transition Metal Oxides (nano-TMO)[5,13,14] have become important in the field of lithium batteries because they present a much higher specific capacity than conventional graphite anodes. The size and shape of nano-TMO[6,7,9,11,12,15–18] can highly improve the capacity of the Li-Ion batteries. However, capacity does not represent the only difficult issue, and the main goal of research is to find out a system with a high stability and long cycling performance at low cost.

In the search for low-cost preparation methods for obtaining nanostructured systems on a large scale, different synthesis procedures have been proposed for producing nano-objects with controlled size.[19–23]

Among those, the *hard-template method*, using a hard silica matrix as template to growth nanostructures, that can easily removed by chemical etching obtaining ordered nanostructeres[24], provides definite advantages, such as specific topological stability, veracity, predictability, controllability and large scale production. This method allows to control in principle size and macroscopic properties of nano-tubes, nano-flakes, nano-sheets and nano-particles.[25] Another important issue in Li-ion batteries is the stability of the chemical components and, in particular, the chemical and thermal stability. Fe_2O_3 presents a definite

chemical phase (Fe^{3+}) and high chemical stability, while the mixed chemical state of Fe_3O_4 ($Fe^{2+/3+}$) might induce instability for its use as an electrode.

Following this trend, this work is aimed at the characterization of the structure, morphology and stoichiometry of iron-oxide nanowires produced following the hard-template route. The study is carried out by a complementary X-Ray diffraction, microscopy and spectroscopy analysis, also addressed at the investigation of the chemical reduction of the nanowires, as induced by increasing temperature and lithium exposure in ultra-high vacuum condition.

Surface chemical state experiments in ultra-high vacuum allow to evaluate the evolution of the reduction phases, controlling thermodynamic parameters and avoiding water and contaminants condensed on the nanowire surface in order to discriminate the contributions due to the real surface with respect of the bulk of the nanowires. A mild annealing of the nanowires leads to an oxygen content reduction at low temperature (170 $°C$), confirming the role of the high surface area in the evolution of the iron oxide phases in the nanosized system. Furthermore, the mechanism of the Fe_2O_3 electrochemical lithiation process has not yet been entirely clarified. The study of the nanowires exposure to different amounts of lithium such as to mimic the electrochemical process in a lithium battery is a first step to understand the oxygen reduction process. The morphology, the crystallinity and the evolution of the nanowires electronic properties upon reduction have been compared to those of micro-sized bulk-like grains, to unravel the role of the reduced size and surface-volume ratio.

Research is also focusing on developing of new architectures for the carbon-based anodes more efficient and stable that the standard graphite anode. In this context Carbon-based Nanostructures (CNs)[26–28] were proposed as alternative in electrodes adapt for Li-Ion batteries[29–34]. Combining the high capability of nano-TMO and cycling performance of CNs, in the last few years, new generations of Carbon-Transition Metal Oxides were proposed[35–45]. In this contest, Graphene, thanks to its large surface to mass ratio, high electrical conductivity and high mechanical strength, is a promising material for electrodes in Lithium-ion batteries. This work is also aimed to characterize the structure and the behavior under lithium exposure of a new generation of graphene produced by graphite exfoliation, comparing the results with that obtained for standard graphite.

Chapter 1

Iron Oxides and Lithium ion batteries

In this chapter an overview of the different properties (crystal structures, electronic and magnetic properties) of the iron oxide compounds is presented. Furthermore the possible application in different research fields is analyzed and in particular in Li-ion battery field. The relationship between low dimensional structures and applicability in Li-ion batteries is also analyzed.

1.1 Iron Oxides

The transition metal oxides compounds are widely distributed in nature. The different compounds, characterized by different crystal structures and oxidation states, are the basis for many technological applications. In particular, the Iron Oxide compounds has attracted great interest in energy storage field of research due to its very low cost and eco-sustainability. Iron Oxides are widely used compounds with various applications in different research fields Fig. 1.1. In heterogenous catalysis iron oxide catalysts are used for instance in the dehydrogenation of ethylbenzene to styrene.[46–48] Furthermore Iron Oxides are of great interest with regard to the corrosion and oxidation processes of iron metal and steel.[49] Magnetic iron oxides nanoparticles are inherently biocompatible and are amenable to post-synthesis surface modification,[50–55] making them excellent candidates for many important applications. In particular biotechnological application include magnetic resonance imaging contrast agents,[56–58] targetable drugs carriers, hyperthermia-inducing agents, and magnetically controlled media

for sensitive separation and detection of biomolecules.[59] The Iron Oxide compounds are used also in technological filed as high-density magnetic recording media or as pigments, and recently as a promising alternative at the carbon-based anode in Lithium-Ion batteries research field.

Oxides have gained considerable importance in different research fields, due to the variety of structural and electronic properties they present, as investigated theoretically[60–64] and experimentally.[65–70]
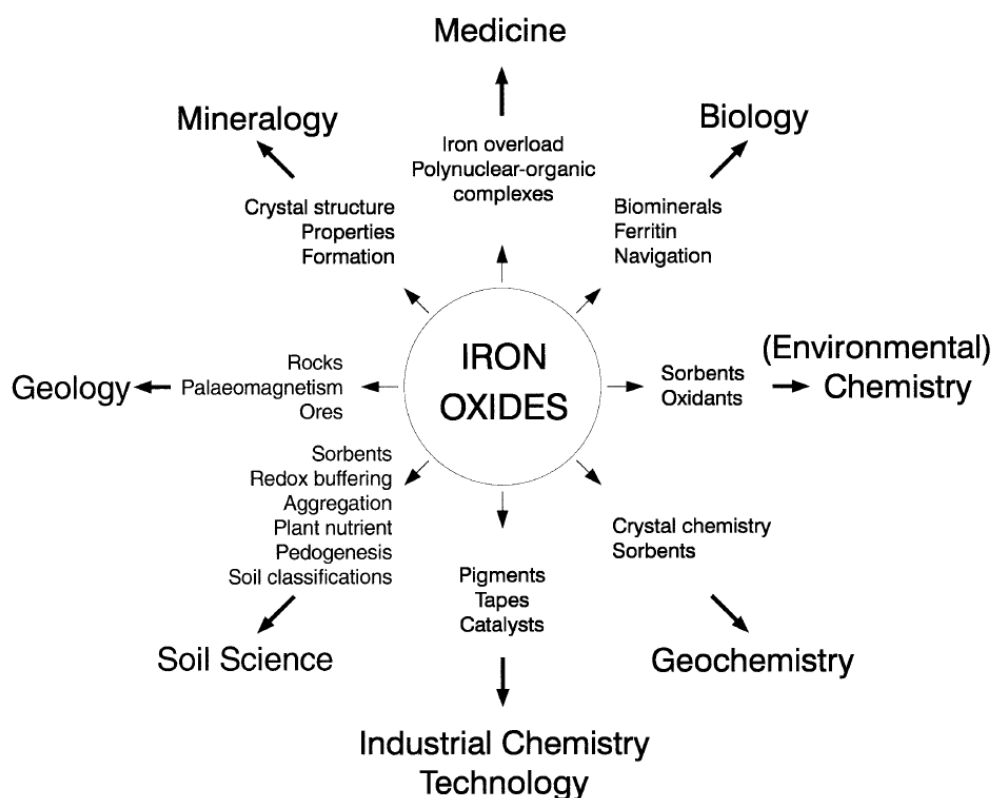
Figure 1.1: Schematic view of possible application of Iron Oxides.

There are 16 different iron oxides compounds and all are a stoichiometric mixture of Fe, O and/or OH ions. The most important in iron oxides compounds are FeO, Fe_2O_3, Fe_3O_4 and FeOOH. In FeO compounds the Iron Ions are in Fe^{2+} (divalent) oxidation state and in Fe_2O_3 are in Fe^{3+} (trivalent) oxidation state, in Fe_3O_4 there is a mixture of Fe^{2+} and Fe^{3+} Tab. 1.1. Different phases of the same oxide, as α and γ phase in Fe_2O_3, present a different crystal structure.

Wüstite FeO has a structure similar to that of NaCl and is base on cubic close packing (ccp) of anion. These iron oxide compound contains only divalent Fe ions (Fe^{2+}) witch occupy octahedral sites. It's black and is important in the reduction processes.

Goethite α-FeOOH has the diaspore (α-AlO(OH)) structure witch is based on hexagonal close packing (hcp) of anions. It is one of the thermodynamically most stable iron oxides at ambient temperature and is, therefore, the first oxide to form or the end member of many reactions.

Hematite α-Fe_2O_3 has the corundum (α-Al_2O_3) structure witch is based on a hcp anion packing. This compound has a blood-red color and like Goethite, hematite is extremely stable and is used also as pigment. The Fe ions are in trivalent ionic state (Fe^{3+}) in an orthorhombic unit cell and are antiferromagnetic below 260 K and weekly ferromagnetic over.

Maghemite γ-Fe_2O_3, with a red-brown color, is a different metastable phase of Hematite and presents a cubic structure. Differently from Hematite, Maghemite is ferromagnetic and finds application in recording tapes. Maghemite presents a structure in that all or most Fe ions are in the trivalent (Fe^{3+}) configuration.

Magnetite Fe_3O_4 is a black, ferrimagnetic compound. Iron ions are in both Fe^{2+} and Fe^{3+} configurations, and sometimes is formulated as $FeO \cdot Fe_2O_3$. The Magnetite has a cubic inverse spinel structure with a face-centered cubic unit cell based on 32 O^{2-} ions.

1.1.1 Crystal Structure

The structures of typical Iron Oxide compounds are reported in Tab. 1.1. It is possible to describe the crystal structures either in terms of the anion arrangement or as a linkages of octahedra and/or tetrahedra formed from a central cation and its nearest anion neighbors. In terms of anion arrangement, the iron oxides are made up of close packed array. The arrangement in the third dimension are hexagonal close packing (hcp), i.e. hematite, and cubic close packing (ccl), only for a few compounds there is a body-centered cubic (bcc) anion arrangement. In the linkage description the basic structural units is the Fe(O)$_6$ octahedron and the Fe(O)$_4$ tetrahedron.

Table 1.1: Crystallographic data for different Iron Oxide Compounds

Compound	Formula	Oxidation State	Crystallographic system	Space System
Goethite	α-FeOOH	II	Orthorhombic	Pnma
Wüstite	FeO	II	Cubic	Fm3m
Hematite	α-Fe$_2$O$_3$	III	Rhombohedral	R$\bar{3}$c
Maghemite	γ-Fe$_2$O$_3$	III	Cubic	P4$_3$32
Magnetite	Fe$_3$O$_4$	II, III	Cubic	Fd3m

Wüstite: the stoichiometric formula FeO is not stable at low pressure. The non-stoichiometry is accommodated by oxidation of a portion of the metal ions and the creation of cation vacancies. The FeO compound has a defective NaCl structure. The cubic unit cell a ranges from 0.428 to 0.431 nm, depending on the vacancy content.

Hematite: the unit cell is hexagonal with lattice parameters $a = 0.5034$ nm and $c = 1.375$ nm or in the rhombohedral system $a_{rh} = 0.5427$ nm and $\alpha = 55.3°$. In term of the anion arrangement hematite can be described as a hcp array of oxygen atoms stacked along the [001] direction. The arrangement of cations produces pairs of Fe(O)$_6$ octahedra that share edges with three neighboring octahedra in the same plane and a face with a octahedron in an adjacent plane.

Magnetite: the structure is that of an inverse spinel[71], with a face-centered cubic unit cell based on 32 O^{2-} ions which are cubic close packed along the [111]. The cell parameter is $a = 0.839$. The iron atoms are present in both divalent and trivalent oxidation states and occupy both tetrahedral and octahedral sites. In the stoichiometric magnetite the ratio between Fe^{2+}and Fe^{3+}is Fe^{2+}/Fe^{3+}=0.5.

Maghemite: the structure is cubic, similar to that of magnetite, with $a = 0.834$ and with all iron ions in the trivalent state. Cation vacancies compensate for the oxidation of Fe^{2+}. The cell of the maghemite contains 32O^{2-} ions, 21^1/$_3$ of Fe^{3+}ions and the 2^1/$_3$ vacancies.

The diffraction patterns of Hematite and Maghemite compounds are shown in Fig. 1.2 with a schematic view of the crystal structures. In the Hematite system the diffraction pattern is characterized by the peaks at 33.1, 35.5, 49.4, 54, and 64 *angle units*, meanwhile the characteristic peaks of Maghemite are located at 35.7, 30.2 and 63.1 2Θ. The diffraction patterns will used to discriminate the

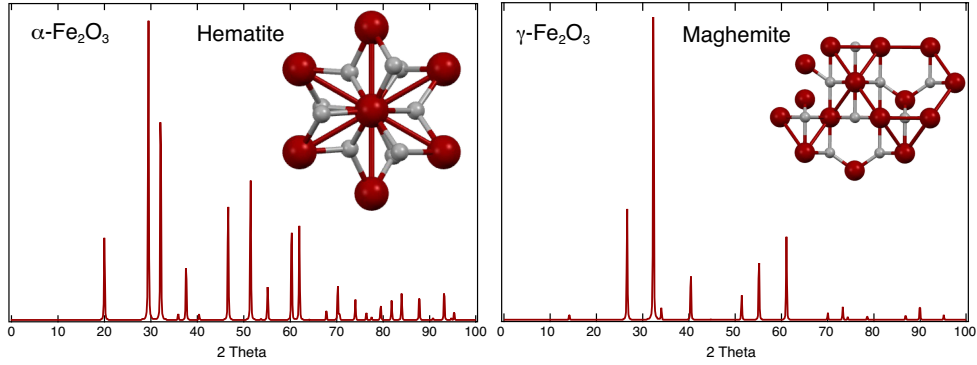crystal structure and phase of nanowires studied in this work.

Figure 1.2: Crystal structures and diffraction patterns of the Hematite (α-Fe$_2$O$_3$) and Maghemite (γ-Fe$_2$O$_3$) compounds.

1.1.2 Electric and Electronic Properties

The Electric properties are correlated to the band structure of the system. Classically the essential characteristic to discriminate a semiconductor is the presence of a gap between Valence Band (VB) and Conduction Band (CB); if the gap is less than 5 eV the system is a semiconductor whereas if the gap is larger the system is classified as insulator, if there is no gap between VB and CB the system has a metallic behavior. The semiconductors are divided in n-type and p-type; in an n-type semiconductor, conductivity is mainly via electron, whereas in a p-type it involves holes. Mobile electrons are the results of a non-stoichiometric compound or of the presence of a dopant in the structure.

Within this contest goethite, hematite, wüstite, maghemite and magnetite are semiconductors. Hematite and Maghemite are n semiconductors with a bang gap of 2.2 and 2.03 eV respectively, Wüstite is a p-type semiconductor with a gap of 2.3 eV. Magnetite, even if considered as a semiconductor, present a very small gap (0.1 eV) and the lowest resistivity of any oxides. The presence in the crystal structure of Magnetite, of two different species of Ions (Fe^{3+} and Fe^{2+}) gives it a slightly metallic behavior due to the vacancies on octahedral sites.

The classification of electric properties is more complicated taking in account the real band structure of systems and the interaction between the occupied and unoccupied d-orbitals in Iron Oxides.

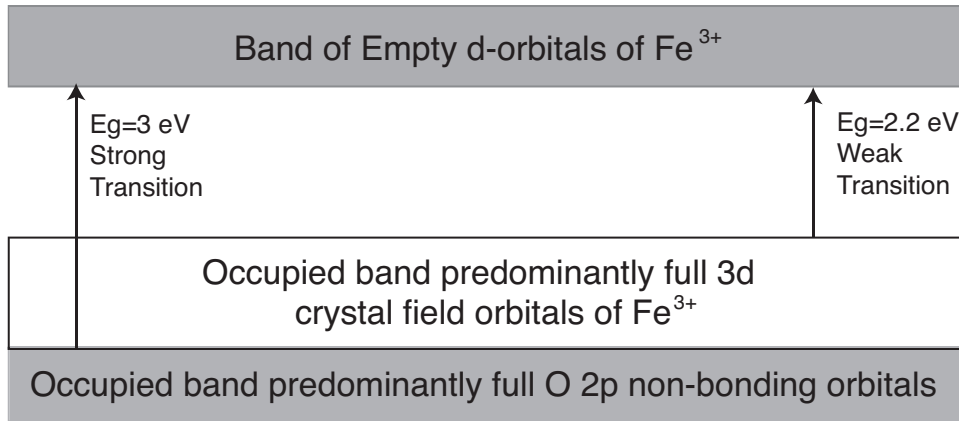The electronic properties are correlated with the occupied and unoccupied

Band of Empty d-orbitals of Fe $^{3+}$

Eg=3 eV
Strong
Transition

Eg=2.2 eV
Weak
Transition

Occupied band predominantly full 3d
crystal field orbitals of Fe^{3+}

Occupied band predominantly full O 2p non-bonding orbitals

Figure 1.3: Schematic representation of band Structure of Hematite (α-Fe$_2$O$_3$).[72]

states in the system. Iron is a transition metal of first row in table of elements. The electron configuration in Fe^{2+}ions is $1s^2 2s^2 2p^6 3s^2 3p^6 3d^6$ and in Fe^{3+}is $1s^2 2s^2 2p^6 3s^2 3p^6 3d^5$. In the Iron Oxides compounds the d orbitals is the most important and that determinate the electronic, magnetic and spectroscopic properties.

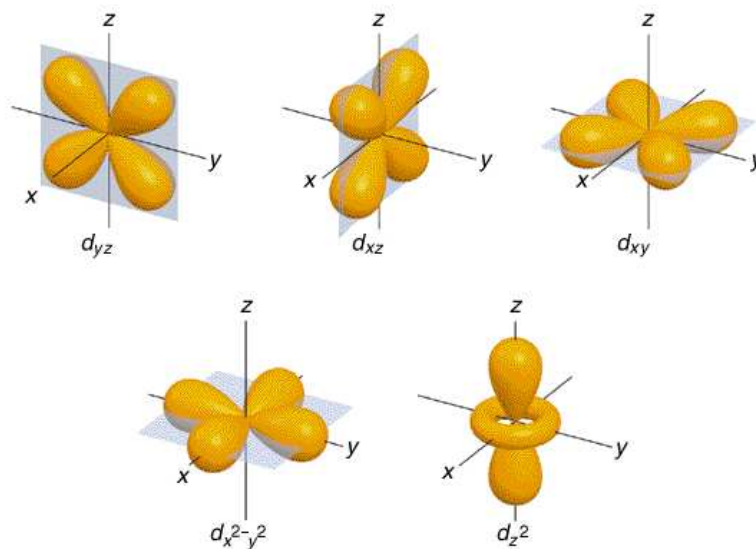**Figure 1.4:** Schematic view of the d orbitals with different symmetry.

There are five different available d-orbitals that consist in two sets: the d_{xy}, d_{xz} and d_{yz} orbitals (in the t_{2g} symmetry) with lobes directed between

the coordinate axes and the d_{z^2} and $d_{x^2+y^2}$ orbitals (in the e_g symmetry) with lobes directed along the axes. A schematic representation of these orbitals is reported in Fig. 1.4. In the ground state Fe^{2+} has two paired and four unpaired d electrons and Fe^{3+} has five unpaired electrons, written with *term symbols* the ground states are $^5D_4$ and $^6S_{5/2}$ respectively.

The available d orbitals, with degenerate energy in single atoms, are split in two set (t_{2g} and e_g) with different energies in the D_4. The splitting and relative energies between the two sets are a direct consequence of the arrangement of the iron ions in the crystal structures. In iron oxides the cations are octahedrally and/or tetrahedrally coordinated to negatively ions (see Par. 1.1.1); as a consequence of the distribution of the ions in the compound, in the octahedral $(Fe(O)_6)$ site the energy of t_{2g} set is lower than the energy of e_g set, whereas in the tetrahedral one $(Fe(O)_4)$ is opposite (Fig. 1.5).[73]
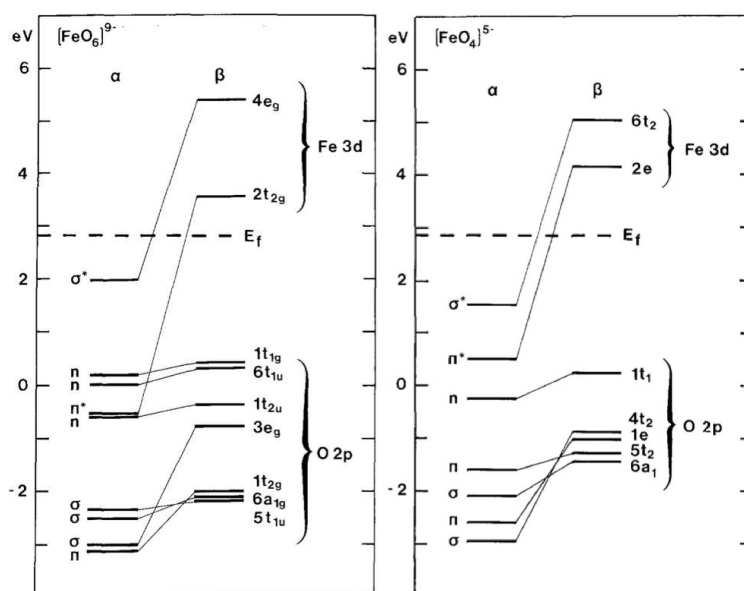
Figure 1.5: Molecular Orbital diagram of $(FeO_6)^{9-}$ cluster (left panel) and an $(FeO_4)^{5-}$ (right panel) clusters; the octahedral $(FeO_6)^{9-}$ configuration is characteristic of the α-Fe_2O_3 compounds and the tetrahedral $(FeO_4)^{5-}$ of the Fe_3O_4. ([73])

The electronic properties of these systems were investigated theoretically and experimentally. A classification of the iron oxides is given analyzing the different contribution of the charge-transfer effect for each compound. The different

contribution can be studied trough x-ray absorption (NEXAFS) and core-level photoemission (XPS) spectroscopies. The XPS techniques studies the the electrons photoemitted from the filled core-level; this technique is sensible to the atoms in the system and can distinguish the chemical states of the compound. Furthermore, this technique is also surface sensitive due to the low escape depth of photoemitted electrons with energy below 1000 eV. Otherwise the NEXAFS technique studies the promotion of photo-excited electrons from filled core-level states to empty valence band states. The energies of the valence band states depends to the crystal structure of the compound. Thus, the analysis of the L_{23} absorption edges, the $2p$ and $3p$ core-levels excitations of the Iron Ions and the K-edge of the Oxygen atoms give a complete characterization of the systems.

The processes involved in these techniques are described in the next chapter (Chap. 2) and the results obtained with iron oxide nanowires and microparticles are reported in the chapter 3.

Hematite: In α-Fe_2O_3 all the iron atoms are equivalent, Fe^{3+} leading to formally d^5 configuration, and occupy the octahedral sites symmetry very slightly distorted from perfect O_h (Sec. 1.1.1).

The Oxygen K-edge absorption spectrum (Fig. 1.6 left panel top spectrum[74]) presents two prevalent structures, the first one in the range between 530 and 535 eV, the second one between 535 and 550 eV. The first region presents two distinct peaks due to the transition from the O-$1s$ filled state to the O-$2p$ empty states; in particular the peaks are due to the projection of the Fe $3d$ character states (t_{2g} and e_g) onto the Oxygen $2p$ states. The splitting observed between t_{2g} and e_g states are due to the breaking of symmetry of the octahedral configuration in α-Fe_2O_3 (Fig. 1.5). In the higher photon energy region the absorption spectrum shows transitions to unoccupied states resulting from hybridization of O-$2p$ and Fe $4s$-$4p$ states. In particular there are different peaks at 539 and 543 eV and a characteristic peak for α-Fe_2O_3 at 546 eV.

The Fe-$2p$ core-levels photoemission spectrum (Fig. 1.6 central panel top spectrum) presents two main peaks located at 711.2 and 724.2 eV related to the Fe-$2p_{3/2}$ and Fe-$2p_{1/2}$ core-levels respectively, and the observed splitting of ≈ 13 eV is due to the spin-orbit interaction in the Fe ions. The two main peaks have a broadened and asymmetric lineshape; the asymmetric lineshape is due to the multiplet structure of core p-vacancy levels[61,62,75] and to the multiple ioniza-
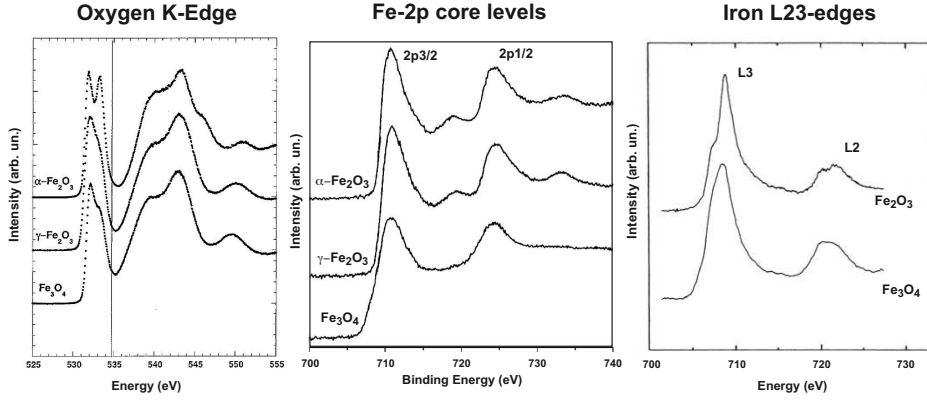
Figure 1.6: Characteristic Oxygen K-edge and Iron L_{23}-edges (left and right panel, respectively) NEXAFS spectra and XPS spectra (central panel) of different iron oxides compounds. α-Fe$_2$O$_3$ (top spectrum), γ-Fe$_2$O$_3$ (middle spectrum) and Fe$_3$O$_4$ (bottom spectrum).

tion of the inner-shell electron.[76,77] The spectrum also presents two additional satellites peaks, S_1 and S_2, located at ≈ 8 eV higher Binding Energy respect to the associated main peaks. These two satellites are associated at the screening processes of the d state in the $\underline{c}3d^6\underline{L}$ configuration ($\underline{c}$ denotes the core hole and $\underline{L}$ is the ligand hole).[67]

The Fe L_{23} absorption spectrum (Fig. 1.6 right panel top spectrum) presents two main structures located at 713 and 725 eV, L_3 and L_2 edges respectively; the two main structure correspond to the transition from Fe-$2p$ filled core-level to the $3d$ empty states divided by the spin-orbit coupling. Both edges present two different peaks, not directly related to the division of d orbitals in t_{2g} and e_g subset, and the splitting and the intensity ratio between these come from the interplay of crystal-field and electronic interaction. The $d^6\underline{L}$ configuration in α-Fe$_2$O$_3$ compound is quite important to show the consequence of the charge-transfer effect in the system. Charge-Tansfer acts on the spectral shape with two different effect. First, it reinforces the splitting of d orbitals by increasing the splitting in molecular orbitals than in the atomic ones. Second, Charge-Tansfer acts on the shape of the tails that can be seen on the higher-energy side of the edge, especially in the L_3.

The Charge-Tansfer effect in photoemission processes was well studied for Fe$_2$O$_3$ compound by Fujimori et al.[67] According to previous classification[78] the

main and satellites feature were assigned to screened $d^5 \underline{L}$ and unscreened d^4 final state and it was concluded that the Fe_2O_3 system is a Charge-Tansfer insulator according to the classification reported in Fig. 1.7.

Maghemite: In γ-Fe_2O_3 the Fe^{3+} ions are disposed in four different sites; three of them are in a pseudo-octahedral configuration and one is in a pseudo-tetrahedral configuration. Taking in account this atoms configuration, even if the oxidation number is the same of α-Fe_2O_3, there is some differences in the characteristic spectra. The adsorption spectrum is more influenced by the changes in the crystal structure, particular in the Oxygen K-edge

In the Oxygen K-edge (Fig. 1.6 left panel central spectrum), in the region between 530 and 535 eV, the t_{2g} and e_g states are closer and there is a modification in intensity ratio due to the pseudo-octahedral and pseudo-tetrahedral position of the iron ions. In the high energy region the spectrum presents only two distinguishable peak at 539 and 543 eV and the peak at 546 eV is not visible.

The Fe-$2p$ core-levels spectrum (Fig. 1.6 central panel bottom spectrum) has a lineshape similar to that observed for α-Fe_2O_3, the energy position and the asymmetry structure in photoemission spectrum is a consequence of oxidation state of Iron ions, that are the same of α-Fe_2O_3 system. The multiplet splitting and the Charge-Tansfer effect act on lineshape specially on the satellites feature that present a slight intensity modification.

The Fe L_{23} adsorption edges present the same structure of that observed in the α-Fe_2O_3 compound but with slight changes; the two peaks in L_3 and L_2 edges have different intensity ratio but the related energies are the same, the theoretical calculations show that the difference between peaks is due to the crystal configuration.[63]

All these phenomena contribute to identify the contribution of the Charge-Tansfer effect in the γ-Fe_2O_3 compound and to classify this system as a Charge-Tansfer insulator, according to the classification reported in Fig. 1.7.[63]

Magnetite: In Fe_3O_4 one-third of the Fe^{3+} ions are in octahedral symmetry, one third in tetrahedral symmetry and the remaining one-third are formally Fe^{2+} ions in octahedral sites.

The Oxygen K-edge adsorption spectrum of Fe_3O_4 presents (Fig. 1.6 left panel bottom spectrum) a lineshape similar to that observed for γ-Fe_2O_3. In the range between 530 and 535 eV the t_{2g} and e_g states in the Fe_3O_4 system are

farther, according to electronic structure calculated and reported in Fig. 1.5. At higher photon energy the spectrum presents only slight variation from that of γ-Fe_2O_3.

The Fe-$2p$ core-levels spectrum (Fig. 1.6 central panel bottom spectrum) presents the main features of the Fe_2O_3 compound; there are two main peaks corresponding to the Fe-$2p_{3/2}$ and Fe-$2p_{1/2}$ core-levels with a splitting due to the spin-orbit interaction and an asymmetric shape due to the multiplet-splitting[61,62,75] and multi-ionization process.[76,77] The two main peaks are located at 710.8 and 723.8 eV with a shift of 0.4 eV respect to that observed in Fe_2O_3. The S_1 and S_2 satellites, observed in pure Fe^3+ compounds, are quenched. The variations observed in Fe_3O_4 compound are a direct consequence of the coexistence of Fe^3+ and Fe^2+ ions.

In the Fe_3O_4 compound the L_{23} edges present two main structures corresponding to the transition from Fe-$2p$ filled core-level to the $3d$ empty states divided by the spin-orbit coupling; differently from the compounds with pure Fe^{3+} , the coexistence of Fe^{3+} and Fe^{2+} reduction state of the iron ions generates additional resonant pre-edges features located about at 705 and 718 eV. The differences from the Fe_2O_3 compounds are due to the change in iron-oxygen distance and to the distortion from the O_h symmetry.

1.1.3 Magnetic Properties

The magnetic properties of a compound are a consequence of the spin alignment in the solid. The parameter that connect the applied magnetic field H to the intensity of magnetization in solid M, is the *magnetic susceptibility*

$$M = \chi H$$

the behavior of the different compounds can be subdivided in four class taking into account the response at an applied external field:

Diamagnetism: It is a basic property that involves a slight repulsion by a magnetic field. The magnetic susceptibility is very small and negative.

Paramagnetism: The substance that are attracted towards a magnetic field are paramagnetic. Paramagnetic materials have a small, positive susceptibility. Differently from ferromagnets, paramagnets do not retain any magnetization in the absence of an externally applied magnetic field because thermal motion randomizes the spin orientations. Below a characteristic temperature the iron oxides
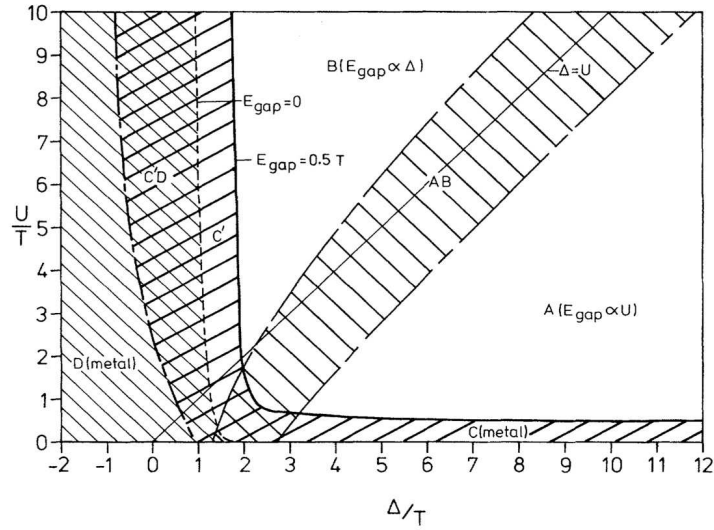
Figure 1.7: Classification of different metal-transition compounds as a function of U (exchange interaction) and Δ (charge transfer). The compounds with U$>$ Δ present a band gap of charge-transfer type while for U$<$ Δ the gap is $d-d$ (Coulomb interaction) type.[78]

undergo a transition to a magnetically ordered state and become ferromagnetic, antiferromagnetic, ferrimagnetic or speromagnetic. The transition temperature is termed the Curie temperature (T_C) for ferromagnetic and ferrimagnetic substances and the Néel temperature (T_N) for antiferromagnetic substances.

Ferro-Magnetism: Ferro-magnetic substances present the alignment of the electron spins parallel to the external magnetic field. Such substances have an overall net magnetic moment, a large magnetic permeability and a large, positive susceptibility. With rising temperature, the ordered arrangement of the spins decreases owing to thermal fluctuations of the individual magnetic moments and the susceptibility falls rapidly

Antiferro-Magnetism: Antiferro-magnetic substances present the alignment of the spins parallel to the magnetic field but with a zero overall magnetic moment.

Super-Paramagnetism: arises as a result of magnetic anisotropy, i.e. the existence of preferred crystallographic directions along which the electron spins are most readily aligned and the substance most easily magnetized. The preferred direction for easy magnetization is along some crystallographic axis or set

of axes, e.g. for magnetite, along the [111] directions. If sufficient energy is supplied, magnetism can be reversed along these axes. Because the appearance of the superparamagnetic effect depends on the particle size and on the anisotropy constant, it is often displayed at room temperature by iron oxides ¡10 nm in size, for example, soil iron oxides.
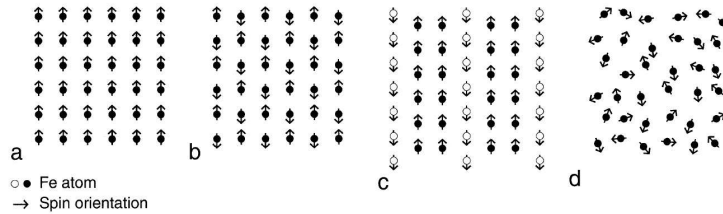

○● Fe atom
→ Spin orientation

Figure 1.8: Schematic illustration of different magnetic order

The magnetic properties of Iron Oxides are a consequence of crystal structure of systems. The interaction between the unpaired electron of Fe ions and the adjacent atoms generate the characteristic magnetic properties of the crystal structure.

Table 1.2: Magnetic Properties for different Iron Oxides

Compound	Formula	Magnetic Structure
Goethite	α-FeOOH	antiferromagnetic
Wüstite	FeO	antiferromagnetic
Hematite	α-Fe$_2$O$_3$	paramagnetic
Maghemite	γ-Fe$_2$O$_3$	ferrimagnetic
Magnetite	Fe$_3$O$_4$	ferrimagnetic

The hematite compound presets the shared Fe^{3+} ions on the *c*-axis; under the Morin temperature (T_M, 260 K) the iron ions are antiferromagnetically coupled and at room temperature present a phase transition to a weak ferromagnetic state above T_M. Above T_C hematite is paramagnetic. Particles smaller than about 8 nm display superparamagnetic relaxation at room temperature.

Differently from the hematite, in the magnetite and maghemite the two different ionic state of Fe atoms, that occupy the tetrahedral and octahedral sites, form two magnetic sub-lattices. Below T_C, the spins of the two different ions are

antiparallel and with different magnitudes; this causes ferrimagnetism. Particles smaller than 6 nm are super-paramagnetic at room temperature. The Curie temperature of magnetite is 850 K while the T_C of maghemite is estimated between 820-986 K because maghemite transforms to hematite at temperatures above ca. 800 K.

1.1.4   Iron Oxides Nanostructeres

Morphology-controlled synthesis of low dimensional nanostructures is an important research subject in nanoscience and nanotechnology because of the unique size and shape dependent properties of these systems. Different geometrical configuration and elemental composition are the bases for different application in a wide range of research fields like energy and data storage, catalytic and optoelectronic devices, biomedicine, nanomagnetism and so on. In particular, among the inorganic materials, iron oxides, such as hematite, maghemite and magnetite, have received a great deal of attention due to their optical, magnetic properties and biocompatibility. In the search for low-cost preparation methods for obtaining nanostructured systems on a large scale, different preparation procedures have been proposed, including Soft-Template method, Flame Vapor Deposition,[20] Colloidal Chemical Synthetic procedure,[19] Hydrotermal method,[21] Thermal Decomposition,[22] Thermal Reduction[11] or Thermal Oxidation.[23]

Recent results obtained on α-Fe_2O_3 nanostructures, synthesized by hydrothermal method, showed that the magnetic and electrochemical properties were shape and size-dependent[79]. α-Fe_2O_3 nanorods, synthesized by low-temperature hydrothermal method by Zeng et al.[80], present shape and size-dependent optical absorption, electrochemical, and magnetic properties.

Table 1.3: Band-Gap, Capacity and Residual magnetization results obtained for nanorods with different size.[80]

Diameter (nm)	Length (nm)	Band Gap (eV)	Capacity (mAh/g)	Res. Magnetization (emu/g)
20-30	40-50	2.65	1040	0.00007
20-30	400-500	2.60	1002	0.0024
30-40	700-800	2.45	859	0.039

In Tab 1.3 the results for nanorods with different size and shape are reported. All the parameters present a trend as a function of size and shape. Compared with the standard value of Band Gap in hematite (2.2 eV[81]), the results exhibit a progressive increasing of band gap with decrease of the samples size in according with the results observed in many semiconductor nanoparticle systems[82–85]. The residual magnetization observed in the nanorods is due to the shape of the systems; the sample with the smallest size presents a shape very close to that of the symmetrically shaped nanoparticles, witch do not present any residual magnetization under application of magnetic field. The shape and crystalline anisotropy observed in the other samples give the alignment of the magnetic spin along the long axis and subsequence increasing of the residual magnetization.

1.2　Lithium Ion Batteries

The exponential growth of electronic devices, development of alternative energy sources and research into clean energy resources have required a major development in storing and redistribution of energy. Due to their high-capacity of energy storage, lithium-ion batteries are used as power sources for many popular devices, including mobile phones, laptops and Mp3 players. Lithium batteries have a large range of application and are not confined to the consumer electronics devices. Sustainable transportation is another suitable field where Lithium batteries may have a very important role.[1,2,4,5,86]

A battery is a transducer that converts chemical energy into electrical energy and vice versa. It contains an anode, a cathode, and an electrolyte. Lithium ion batteries are light and compact, conventionally its structure contains a graphite anode, a cathode formed by a lithium metal oxide ($LiMO_2$) and an electrolyte consisting of a solution of a lithium salt (e.g. LiPF6) in a mixed organic solvent imbedded in a separator felt (Fig. 1.9).
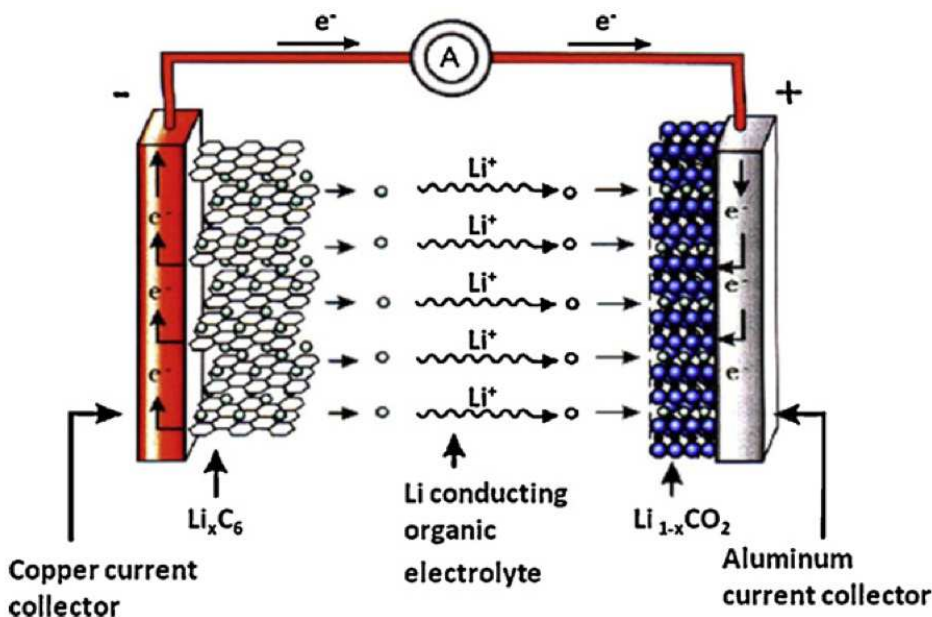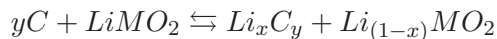

Figure 1.9: Schematic illustration of a common lithium ion battery.[2]

In most common case these batteries operate on a process

$$yC + LiMO_2 \leftrightarrows Li_xC_y + Li_{(1-x)}MO_2$$

$$x = 0.5, y = 6, voltage = 3.7V$$

involving the reversible extraction and insertion of lithium ions between the two electrodes with a concomitant removal and addition of electrons. The electrochemical process witch governs the exchange of lithium ions and electron between the two electrodes is based on the redox process at the anode and cathode. These processes evolves in specific V *vs.* Li range for different anode and cathode materials, in a standard mesocarbon microbeads (MCMB) graphite anode the redox process evolves around 0.05 V *vs.* Li and for the $LiCoO_2$ cathode evolves at about 4.0 V *vs.* Li (Fig. 1.10-A).
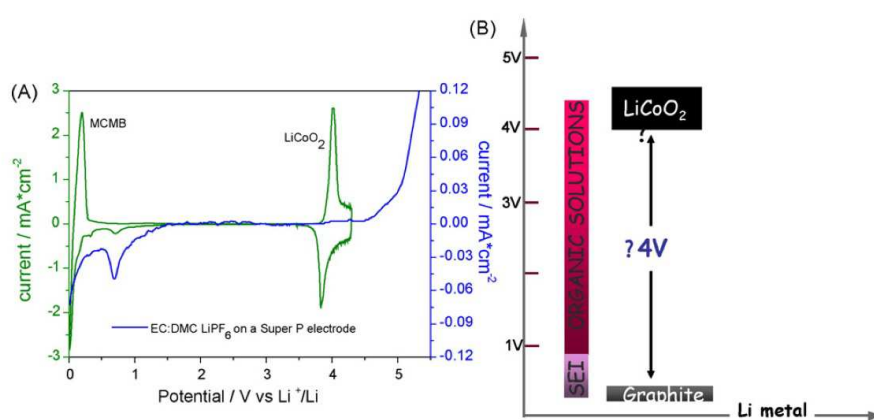

Figure 1.10: A) Cyclic voltammetry profiles of a $MCMB - LiCoO_2$ standard battery. The activation energies for MBCM and $LiCoO_2$ are visible at 0.05 and 0.4 V (green line). B) Schematic representation of working range of standard electrolyte solutions in comparison with the activation energies of MCMB and $LiCoO_2$ electrodes.[2]

A standard electrolyte solution works in a range between 0.8 and 4.5 V *vs.* Li, the MCMB anode operates outside the stability of the electrolyte and the cathode operates at the upper limit of stability (Fig. 1.10-B); considering these features the MCMB/LiCoO2 batteries could be thermodynamically unstable. However, the anode surface is protected by the formation of a film that provides the condition to ensure the continuation of its charge and discharge processes. Under proper conditions the battery operates below the oxidative limit of the electrolyte however, if by unexpected events, such as accidental overcharge, this limit is exceeded, no protecting film is formed on the cathode and the electrolyte continues to oxidize, this contributes to accelerate cell failure.
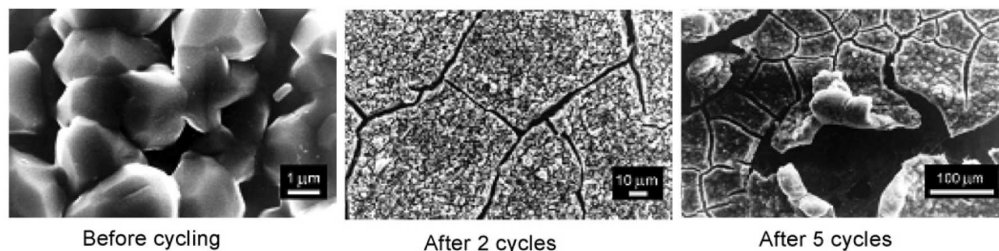
Before cycling   After 2 cycles   After 5 cycles

Figure 1.11: Volume change effects associated to the charge and discharge process of metal alloy electrodes in lithium cells. Evolution of Lithium alloy anode surface after different charge-discharge cycles.[87]

Because of the relatively low capacity of carbon materials, research in the field of lithium batteries has led to consider alternative solutions for anode materials.[2,14,19,88–95] The graphite-based anodes have a specific capacity of 370 mAh/g.[2] Lithium metal alloys, e.g. lithium-silicon (Li-Si), and lithium-tin (Li-Sn), alloys, are among the most promising negative electrodes to replace common carbon based materials. These alloys have a specific capacity which largely exceeds that of lithium-graphite, i.e. about 4000 mAh/g for Li-Si[96] and 990 mAh/g for Li-Sn.[97] Unfortunately, lithium alloys cannot be used as such in lithium cells, the main issue being the large volume expansion-contraction which occurs during the charge-discharge processes; these volume changes induce mechanical stresses and the resulting disintegration of the electrode and consequent failure in the round of cycles[87,98].

Transition-metal oxides have become important in lithium-based batteries fields for their high capacity (1007 mAh/g), non toxicity and large diffusion.[4,5,15,99] Fe_2O_3 system is one of the most promising transition-metal oxides compound; the iron ions, in Fe^{3+} ionic state, can store six lithium ions *per* Fe_2O_3[7]

$$Fe_2O_3 + 6Li \leftrightarrows 2Fe + 3Li_2O + 6e^-$$

Compounds at the nanosize scale, and iron-oxides are among the most promising systems.[10,86,89,91,100] In particular, research is focusing on developing nanostructured systems that can make even more stable and efficient batteries. The size and shape of the oxides are important parameters for the efficiency of energy storage devices. Different sizes of iron-oxide particles induce different capacity and cycling lifetimes.[10,11,101–103] Micro-size Hematite (α-Fe_2O_3) particles present

a good capacity but show a low capacity-cycling behavior. Fundamental factors that affect the capacity of lithium batteries are the exchange surface, present in the oxides, and the mean free path that the electrons have to travel in the compound. In Fig. 1.12 the electrochemical behavior of bulk and nanostructured α-Fe_2O_3 with voltage-composition curves is reported.[7]
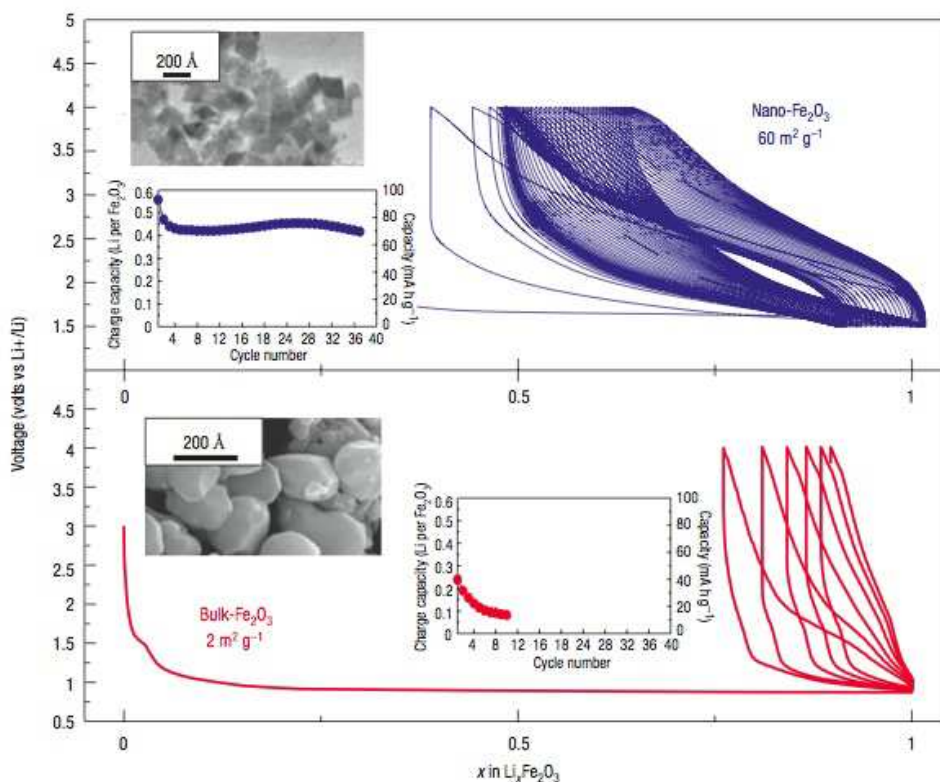

Figure 1.12: Electrochemical behavior of bulk and nanostructured α-Fe_2O_3 with voltage-composition curves. In the insets, the capacity retention and scanning electron micrographs of both samples are shown.[7]

Different methods for producing nanostructures with controlled size are presented in literature (Sec. 1.1.4)[11,19–23,104]. Among them, the *hard template method* has attracted great interest; this method uses a hard silica matrix as template to growth nanostructures with different size. The silica matrix can be easily removed by chemical etching obtaining ordered nanostrucutre.[24] This method presents definite advantages: specific topological stability, predictability and controllability. The preparation allows to control the size and the macroscopic properties of these systems, but it does not provide direct information on

the crystalline and electronic properties of the produced nanowires. In particular, nanotubes, nanoflakes, nanosheets and nano particles of various shape of iron oxide have been recently synthesized and characterized[25].

These materials demonstrated superior electrochemical behavior in lithium cells in comparison with the corresponding bulk material in view of the free space created by their particular structure, allowing a buffering action against volume change experienced by the material upon lithiation-delithiation process.[8,105]
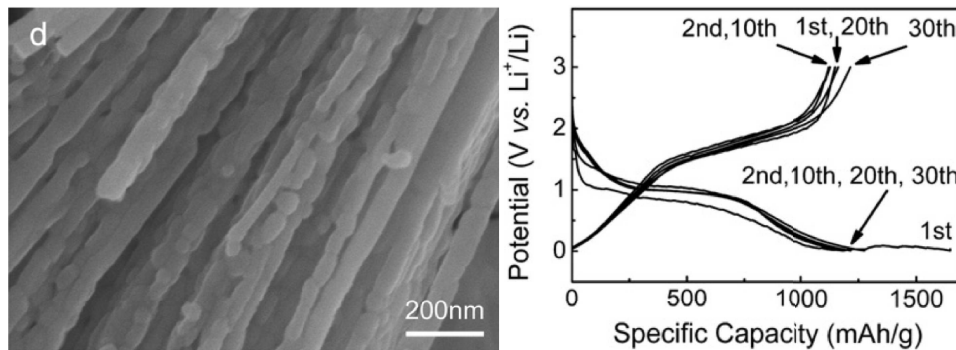

Figure 1.13: SEM image (left panel) and electrochemical performance, galvanostatic charge/discharge profile, (right panel) of porous of α-Fe$_2$O$_3$ nanorods.[95]

Another consequence of reduce dimensions of these systems is the higher capacity of the smallest samples[7]. During the lithiation process in a cell of Li/α-Fe$_2$O$_3$ the Lithium ions intercalate and interact with the hematite surface; taking into account the size and shape of the systems, the samples with the smallest size and with the highest surface area present the highest capacity. An example of iron oxide nanostructure is reported in Fig. 1.13; porous α-Fe$_2$O$_3$ nanorods show a very high specific capacity at the first cycle (over 1500 mAh/g) and can deliver a capacity of 1275 mAh/g after 30 cycles.[95] The ad-hoc designed structures may lead to iron oxides with significantly improved performances both in term of specific capacity and of rate capability, i.e. very important parameters in order to evaluate the suitability of the materials for battery applications[30].

An improvement of performances can be achieved combining the high capacity of the iron oxide with the properties of the carbon atoms.[17,29–31,33,34,100,106–110] A TEM image of Fe$_2$O$_3$/C composite is shown in Fig. 1.14 (left panel); in this system, irregular Fe$_2$O$_3$ nanoparticles are embedded in a carbon matrix.[111] Such carbon-isolating structure may prevent particle agglomeration and accommodate
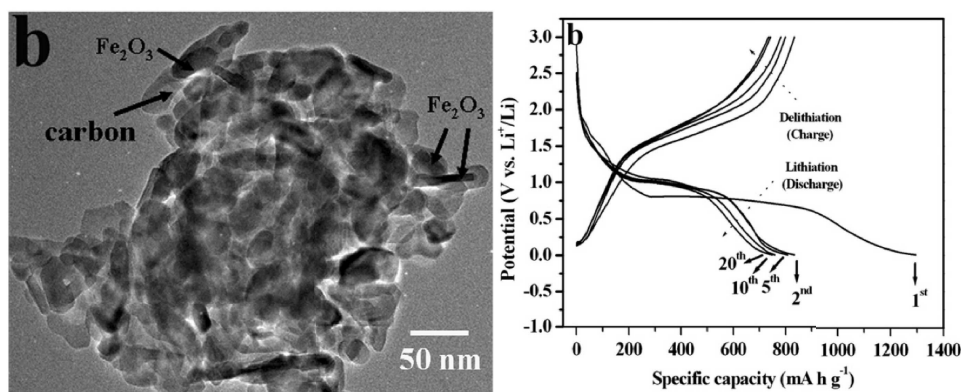
Figure 1.14: TEM image (left panel) and electrochemical properties (right panel) of Fe2O3/C.[106]

large volume change on repeated cycling, thereby ensuring good electrical contact between Fe_2O_3 and the conductive carbon matrix.[112] The charge/discharge capacities of this electrode, evaluated form the galvanostatic curves (Fig. 1.14, right panel), are 749/735 mAh/g for the 20th cycle and 1295/834 mAh/g for the first cycle, respectively. These results indicate good cycling stability and reversibility. The irreversible capacity during the first cycle may be related to SEI formation.[113,114]
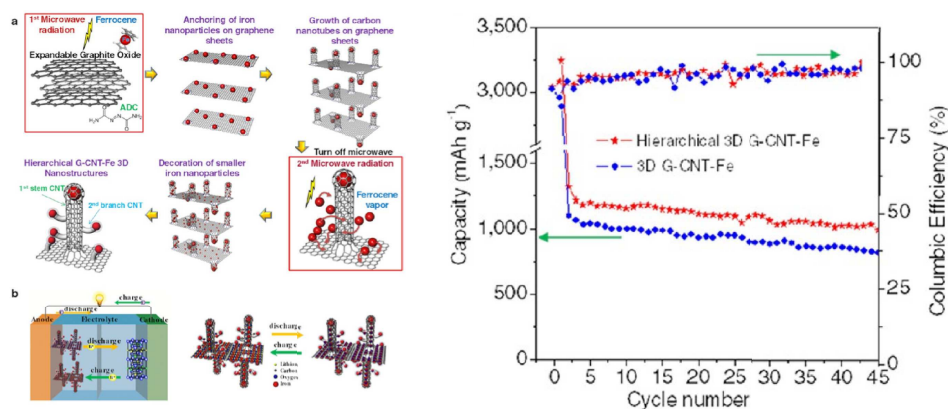

Figure 1.15: Left Panel: a) Two-step synthesis of hierarchical G-CNT-Fe 3D nanostructure and its application to anode material in lithium ion batteries. b) Schematic diagram for charge and discharge in G-CNT-Fe 3D anode material. Right Panel:specific capacity and Coulombic efficiency of anode electrodes for both baseline and hierarchical 3D G-CNT-Fe nanomaterial.[40]

Another way to take advantages from the high stability of the carbon structures is to use Graphene-based structures. Graphene, a free-standing two-dimensional (2D)[115,116] carbon material,has been exploited in a wide range of applications, including supercapacitors,[117] batteries,[118] solar cells,[119] actuators,[120] sensors,[121] composites,[122] and hydrogels.[123] Graphene thanks to its large surface to mass ration (exceeding 2600 m^2/g)[117], high electrical conductivity[116] and high mechanical strength[124] with the added value of mass production,[125] is a promising material for electrodes in Lithium ion Batteries.[33,109,126–139]

The iron oxide nanoparticles can be integrated in graphene structures to create different ad-hoc structures.[37–45,140,141] A example is reported in Fig. 1.15[40]; the graphene structure improve the stability of the system and the transport of the electrons from iron oxides nanoparticles to electrodes.

Chapter 2

Experimental Details

In this chapter, an overview on the different experimental techniques and sample synthesis used in this work, is presented.

In order to obtain a complete characterization of the system, different spectroscopies and microscopies techniques have been used. Electron spectroscopies, as *X-Ray Photoemission Spectroscopy* (XPS) and *Near Edge X-Ray Absorption Fine Structure* (NEXAFS), studying the responses of the system to irradiation with x-ray, give information about the electronic structure and chemical state of the system. Microscopies, as *Atomic Force Microscopy* (AFM) and *Scanning Electron Microscopy* (SEM), investigate the morphology and arrangement of the surface with high resolution.

The procedures for the synthesis of the Fe_2O_3 nanowires and of the graphene nanoflakes are presented. Iron oxide nanowires and graphene nanoflakes have been prepared for morphological and spectroscopical characterizations and for electrochemical experiments; the synthesis procedures for the two systems are chosen in order to obtain nanostructures with controlled size on large scale production and the best configuration for the electrodes. The Iron Oxide nanowires have been synthesized by Hard-Template method. The graphene nanoflakes are prepared from graphite exfoliation via low-power ultrasonication.

2.1   Electron Spectroscopies

The most important techniques to study the electronic structure of a compound are based on the electron spectroscopies. The electrons generated by photoexcitation processes, with photons in a energy range between 10 and 1000 eV, have a small mean feee path in the solids (Fig. 2.1)[142]. The small mean free path of

the electrons makes photoelectron spectroscopies the most suitable techniques
to investigate the surface properties of the system. Here the main models and
properties of photoemission and photoabsorption based techniques are described.
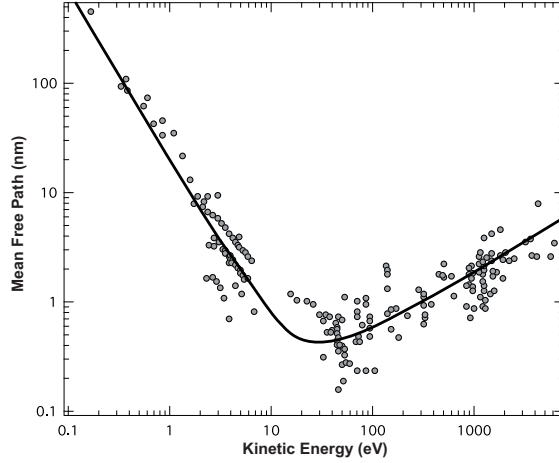

Figure 2.1: Main Free Path of photo-excited electrons at different energies. [142]

2.1.1 Interaction of radiation with matter

The basic representation of photoemission and pho-absorption processes are pic-
tured in Fig. 2.2. In the photoemission process, the electron in Valence Band
(VB) or Core Levels (CL) states are photoemitted and the final state is a free
electron. [143] In the photoabsorption the excitation take place from a core level
to a free bound state of the system.

The interaction cross section of both processes σ is defined as the number of
excited electrons *per* unit time, normalized by the incident flux of radiation I:

$$\sigma(h\nu) = \frac{\Gamma_{i,f}(h\nu)}{I(h\nu)} \tag{2.1}$$

where $\Gamma_{i,f}(h\nu)$ is defined as the probability of the transition from the initial
i state to the final f state, and it can be written in terms of the Fermi golden
rule as:

$$\Gamma_{i,f}(h\nu) = \frac{2\pi}{\hbar}|\langle f|H_{int}|i\rangle|^2\rho(E_f)\delta(E_i - E_f - h\nu) \tag{2.2}$$

where H_{int} is the interaction with the electromagnetic field and is assumed
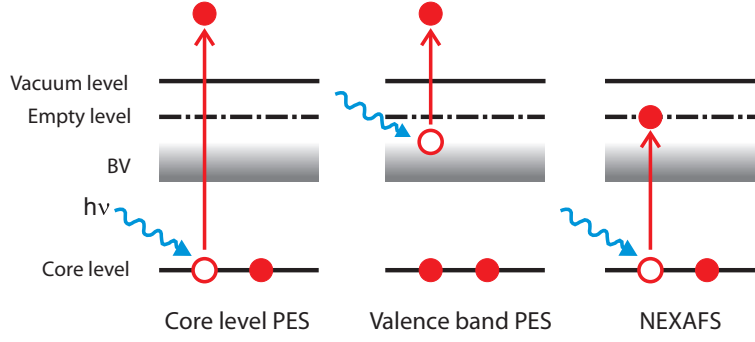to be a small perturbation to the atomic hamiltonian. In the semi-classical

Figure 2.2: A schematic view of the photoexcitation processes. First and second panel represent the photoemission from a core level to an empty state. In the third panel is depicted the near edge absorption given by the transition of a core electron to an empty bound level of the system.

approximation, the electromagnetic field is described by a vector potential $\mathbf{A}$ while the matter is treated quantistically. The interaction Hamiltonian can be written as:

$$H_{int} = \frac{e}{2mc}(\mathbf{A} \cdot \hat{\mathbf{p}} - \hat{\mathbf{p}} \cdot \mathbf{A}) + \frac{e^2}{2m}\mathbf{A}^2 - e\varphi \tag{2.3}$$

where φ is the scalar potential of the field. Exploiting the gauge freedom and choosing the Coulomb gauge defined by $\varphi = 0$ and $\nabla \cdot \mathbf{A} = 0$ the H_{int} can be rewritten as:

$$H_{int} = \frac{e}{mc}\mathbf{A} \cdot \hat{\mathbf{p}} + \frac{e^2}{2m}\mathbf{A}^2 \tag{2.4}$$

and taking into account only the linear term in the perturbation field:

$$H_{int} \simeq \frac{e}{mc}\mathbf{A} \cdot \hat{\mathbf{p}} \tag{2.5}$$

the interaction cross section becomes:

$$\Gamma_{i,f}(h\nu) = \frac{2\pi}{\hbar}\left(\frac{e}{mc}\right)^2 |\langle f | \mathbf{A} \cdot \hat{\mathbf{p}} | i\rangle|^2 \rho(E_f)\delta(E_i - E_f - h\nu) \tag{2.6}$$

and in term of the electric field ($\mathbf{A} = -c\mathbf{E}/\omega$):

$$\Gamma_{i,f}(h\nu) = \frac{2\pi}{\hbar}\left(\frac{e\mathbf{E_0}}{m\omega}\right)^2 |\langle f | e^{j\mathbf{kr}}\hat{\mathbf{e}} \cdot \hat{\mathbf{p}} | i\rangle|^2 \rho(E_f)\delta(E_i - E_f - h\nu) \tag{2.7}$$

Dipole Approximation

The exponential component of the electric field ($e^{j\mathbf{kr}}$) can be expanded in series as:

$$e^{j\mathbf{kr}} \simeq 1 + j\mathbf{k} \cdot \mathbf{r} + \ldots$$

The dipole approximation consists in neglecting all the terms but the first. In this approximation Γ is given by:

$$\Gamma_{i,f}(h\nu) = \frac{2\pi}{\hbar} \left(\frac{e\mathbf{E_0}}{m\omega} \right)^2 |\langle f\, |\hat{\mathbf{e}} \cdot \hat{\mathbf{p}}|\, i\rangle|^2 \rho(E_f)\delta(E_i - E_f - h\nu) \qquad (2.8)$$

The term neglected in this approximation represent the quadrupole interaction $|\langle f\, |(j\mathbf{kr})(\hat{\mathbf{e}} \cdot \hat{\mathbf{p}})|\, i\rangle|^2$. In the case of optical transitions the wavelength of the radiation is very long with respect to the the initial and final state, and the exponential factor doesn't change in the region of functions integration. In this case the dipole approximation is a very good one.

In the case of X-ray transition the wavelength is of the same order as the extension of the atomic orbitals (few Å). Generally the spatial extension of the core states reduces as $1/Z$ with increasing Z number; on the other side the energy of the absorption edges increases as Z^2. The wavelength of the radiation needed to excite a core level decreases as $1/Z^2$. For the element with high Z the quadrupole term is not negligible and became appreciable in the K-edge of 3d elements.

Dipole Moment

The matrix element of the Fermi Golden rule is described in term of $\hat{\mathbf{p}}$ operator. Using the well known result of the quantum mechanics, according to which the time derivate of any operator $\mathbf{F}$ is given by the commutator of the same operator with the hamiltonian of the system:

$$\hat{\dot{F}} = \frac{1}{j\hbar} \left[\hat{H}\hat{F} - \hat{F}\hat{H} \right]$$

the matrix element of the equation 2.8 can be rewritten as:

$$\langle f\, |\hat{\mathbf{e}} \cdot \hat{\mathbf{p}}|\, i\rangle = \langle f\, \left| \hat{\mathbf{e}} \cdot m\frac{d\mathbf{r}}{dt} \right|\, i\rangle = \frac{m}{j\hbar}\langle f\, \left| \hat{\mathbf{e}} \cdot \left[\hat{H}\mathbf{r} - \mathbf{r}\hat{H} \right] \right|\, i\rangle =$$

$$= \frac{m(E_f - E_i)}{j\hbar}\langle f\, |\hat{\mathbf{e}} \cdot \mathbf{r}|\, i\rangle = \frac{m\omega_{if}}{j\hbar}\langle f\, |\hat{\mathbf{e}} \cdot \mathbf{r}|\, i\rangle \qquad (2.9)$$

with this formulation the relationship between the cross section and the electric dipole matrix element is clear

$$\sigma \propto \langle \psi_f \left| \hat{\mathbf{e}} \cdot \mathbf{r} \right| \psi_i \rangle \rho(E_f) \delta(E_i - E_f - h\nu) \tag{2.10}$$

The cross section in 2.10 is proportional to the matrix element involving the initial and final state of the system. The different electron spectroscopies can be described using the right approximation to the final state.

2.1.2 Photoemission Spectroscopy

In the photoemission experiments, electrons are excited from filled level (core levels or valence band levels) and photoemitted to an empty not-bound level (Fig. 2.2 first and second panel respectively).

In order to understand the photoemission phenomena in a solid system, it is assumed that the system under investigation has N electrons. In the photoemission process the final state is a $N - 1$ electrons state, with $N - 1$ in the solid plus one excited free electron. The binding energy (E_B) of the photoemitted electron can be calculated from

$$E_B = h\nu - E_K - \phi \tag{2.11}$$

where E_K is the kinetic energy measured after the photoemission process, $h\nu$ is the incident photon energy and ϕ is the work function of the solid that represent the energy difference between the vacuum level and the Fermi level.

Depending of the photon energy, different initial state can be measured. With ultraviolet photons (5-100 eV), the electrons are photoemitted from the valence band, with X-ray photons (with energy in the range of $100 - 1000$ eV for soft x-ray and >1000 for hard x-ray) the electrons in core-level states are photoemitted. Considering the different binding energies of electrons in the different elements of the periodic table, studying the photoemitted electrons from the core-level states, this technique gives specific information about the atoms and chemical state.

Three Step Model

In the single particle picture, the photoemission current can be written taking into account three different independent contributions:

1. Excitation: the photo-excitation of the electron from the initial state;

2. Transmission: the travel of the photo-electron from the photo-excitation site to the sample surface;

3. Emission: the emission of the electron from the surface.
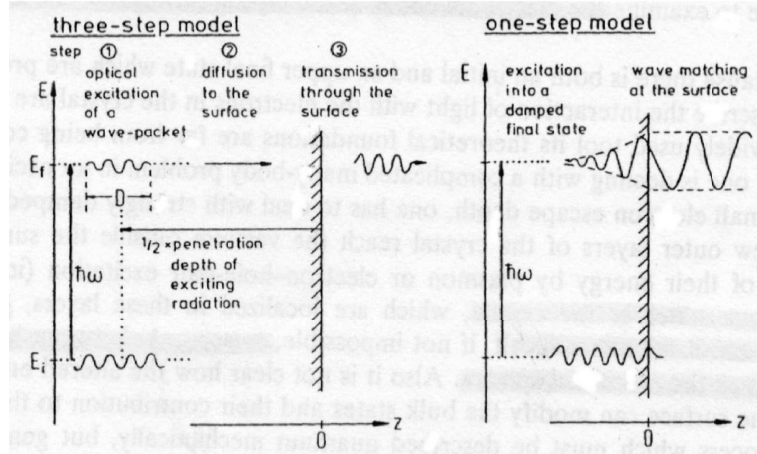
and this method is called *Three Step Model*[144,145].

Figure 2.3: Schematic view of the models adopted to picture the photoemission process. In the right panel is schematized the one-step model in witch the electron are directly photoemitted from the initial state without interaction. In the left panel the three-step model is represented: the photo-excited electrons diffuse trough the material and are emitted from the surface.[146]

Excitation: the first step gives the photocurrent of the electrons and holds all the information on the electronic structure of the material, and can be written as

$$I \propto \sum_{i,f} |M_{i,f}|^2 \delta(E_f - E_i - h\nu)\delta(E_{kin} - [E_f - \phi])\delta(\mathbf{k}_f - \mathbf{k}_i + \mathbf{G}) \qquad (2.12)$$

where $|M_{i,f}|$ is the matrix element of the Fermi Gold's rule, and the Dirac deltas take into account the conservation laws for:

• the energy in the excitation process inside the crystal,

• the energy between the excited state and the free electron,

• the momentum.

Transmission: the photo-excited electrons travel from the photo-excitation site to the surface trough the bulk. Due to the scattering with impurities, electrons and phonons not all the excited electrons conserve unaltered their final energy and reach the surface. To consider these energy variations, the second step can be described by an energy dependent diffusion factor:

$$d(E_f, k) = \frac{\alpha\lambda}{1 + \alpha\lambda} < 1 \tag{2.13}$$

where α is the optical absorption coefficient and λ the electron mean free path.

Emission: the photo-excited electrons can now overcome the potential barrier and escape from to vacuum. To overcome the potential barrier at the surface the photoelectrons perpendicular moment must obey, out of the surface, to

$$k_\perp^{ext} = \frac{1}{\hbar}\sqrt{2mE_{kin}}cos\theta \tag{2.14}$$

where $k_\perp^{ext}$ is the momentum component perpendicular to the sample surface out of the sample and θ is the polar emission angle. The emission factor can be defined as

$$T(E_f, \mathbf{k}) = \frac{1}{2}\sqrt{1 - \frac{E_F - \phi}{E_f}} \tag{2.15}$$

that is valid only if $E_f > E_F - \phi$.

In conclusion the photoemission current can be rewritten as:

$$I \propto \sum_{i,f} |M_{i,f}|^2 d(E_f, k) T(E_f, \mathbf{k})$$
$$\times \delta(E_f - E_i - h\nu)\delta(E_{kin} - [E_f - \phi])$$
$$\times \delta(\mathbf{k}_f - \mathbf{k}_i + \mathbf{G})\delta(\mathbf{k}_{i\parallel} - \mathbf{G}_\parallel + \mathbf{k}_\parallel^{ext}) \tag{2.16}$$

where the last Dirac delta gives the conservation of the parallel moment component during the surface transmission process.

2.1.3 Near Edge X-Ray Absorption Spectroscopy

The x-ray absorption spectroscopy studies the trend of the absorption coefficient of photons as a function of energy.[147] Differently from the photoemission processes in the absorption process the electrons are excited from a filled core level

to an empty bound level of the system (Fig. 2.2 right panel). The incident photon cross section is a smooth decreasing function of the photon energy when the energy is far from a core level binding energy. When the photon energy is near the energy of occupied core level, core electrons will be excited to unoccupied states of the valence band, giving rise to sharp peaks (*Near Edge X-Ray Absorption Fine Structure*, NEXAFS). At higher photon energies, the photoelectron is excited to a continuum of states and the absorption structures are affected by the scattering environment (Extended X-ray absorption fine structure, EXAFS). The XAS spectroscopy is intrinsically a synchrotron radiation technique as photons with variable energies are required to perform absorption measurements. The details of Synchrotron Radiation are reported in 2.7.

The intensity of the transition depends from the cross-section and the transitions obey to the dipole selection rules. Writing the operator $\hat{\mathbf{e}} \cdot \mathbf{r}$ using the spherical harmonics representation

$$\hat{\mathbf{e}} \cdot \mathbf{r} = \sqrt{\frac{4\pi}{3}} \left(\epsilon_z \Upsilon_{1,0} + \frac{-\epsilon_x + i\epsilon_y}{\sqrt{2}} \Upsilon_{1,1} + \frac{\epsilon_x + i\epsilon_y}{\sqrt{2}} \Upsilon_{1,-1} \right) \qquad (2.17)$$

It is then possible to deduce the following selection rules for an impinging linearly polarized or circularly polarized radiation:

$$\Delta j = 0, \pm 1 \quad \Delta l = \pm 1 \quad \Delta s = 0 \quad \Delta m = \begin{cases} 0 & Linear\,Pol. \\ \pm 1 & Circular\,Pol.(R, L) \end{cases} \qquad (2.18)$$

In this work we will study the absorption from an initial $1s$ state (K-shell excitation), whose final state is a p orbital and $L_{2,3}$ excitations, from a $2p$ orbital to a d or s orbital final state.

X-ray absorption needs a continuum of photon energies in energy range of X-rays and a highly collimated flux in order to detect absorption signal. The intensity of photoelectrons, primary excitation channel, is the most direct method for measuring the absorption coefficient. But in this way we loose all information about the bound state excitation. A secondary process of core hole annihilation is the emission of an Auger electron or a fluorescent photon from the system.

Three ways for detecting electron decay are possible: Auger electron yield, partial electron yield and total electron yield. In total yield all electrons (not only Auger electrons, but also photoelectrons) that hit the detector are registered. In
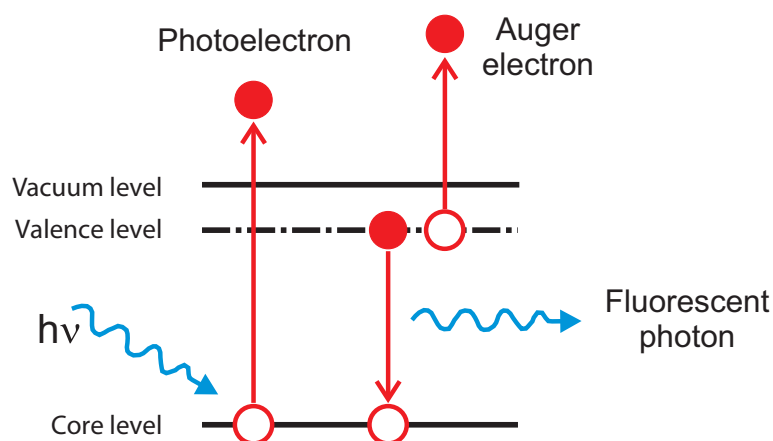
Photoelectron ● **Auger electron**

Vacuum level

Valence level

hν

Fluorescent photon

Core level

Figure 2.4: Schematic view of the processes after photon absorption: the primary channel is the production of photoelectrons, the secondary channel consists of Auger and fluorescent decays.

partial yield, a retarding voltage in front of the XAS detector is set in order to cutoff low kinetic energy electrons. In Auger yield a hemispherical analyzer is used in an energy window (with a high and a low kinetic energy cut-off) defined by the energy of the Auger electrons expected for the defined transitions.

2.2 Experimental Details

In this section the experimental apparatus for XPS and NEXAFS analysis will be described. In particular the setup at the LOTUS laboratory of Università di Roma 'La Sapienza' where the XPS characterization measurements have been performed and at BEAR beamline where NEXAFS measurements have been performed.

2.2.1 In-situ XPS

The standard *in situ* source for XPS experiment is pictured in Fig. 2.5 (Left part). The X-ray source consists of a cathode (filament), which emits thermal electrons through heating, and an anode to which the electrons are accelerated by applying a high voltage of typically 12 kV. These electrons produce core holes in the anode target materials by electron impact ionization. The vacancies can relax by emission of characteristic X-rays that illuminate the sample. The energy of the main emission line for a aluminum source is $K_{\alpha_1} = 1486.6 \ eV$
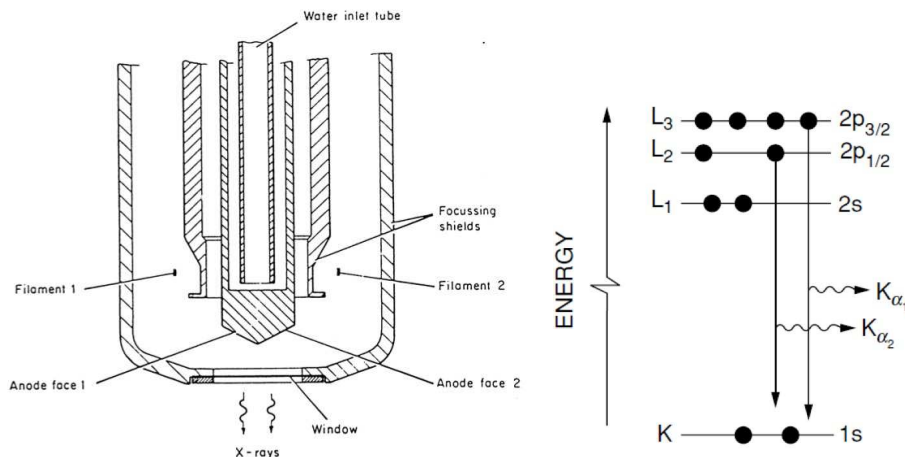
Figure 2.5: Left panel: schematic view of a standard X-ray source. Right panel: schematic view of the decay processes and production of photons with characteristic energies.

LOTUS Setup

All the measurements at LOTUS have been performed in UHV chamber. The chamber is equipped with Ar^+ ion bombardment gun, quartz microbalance (microB), residual gas analyzer (RGA) and with a LEED apparatus, a XPS source and an electron-energy analyzer (CLAM-2 VG Microtech). The samples have been mounted on a manipulator with four degree of freedom.

The electrons analyzer, 100 mm average radius, was used with a pass energy of 100 eV, with an overall energy resolution of 1 eV. For the XPS measurements the samples have been positioned under the XPS source oriented with an angle of 45° between incident radiation and sample, (Fig. 2.6) in order to obtain the normal emission and to maximize the detectable photoelectron flux in the electron analyzer. The Binding Energy (BE) was calibrated with respect to clean Au in electrical contact with the sample, by measuring the $Au - 4f_{7/2}$ core level at 84.0 eV and the XPS peak shift has been evaluated also by using first derivative of data

Lithium exposure has been carried out in-situ in UHV, by means of commercial SAES Getters dispensers, which deliver the alkali metal enclosed into a sealed metal vessel, by heating the vessel with a current of about 7.5 A. Before the first alkali metal deposition on the samples, dispensers have been carefully outgassed at current values close to evaporation for several hours. As it con-
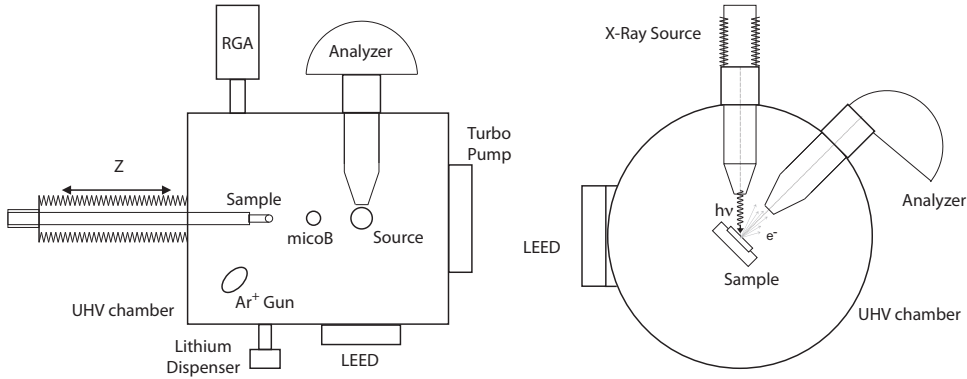
Figure 2.6: Schematic representation of LOTUS chamber and experimental setup used in this work.

cerns the experimental measurements as a function of annealing temperature, the samples were heated by resistively heating the sample holder at different temperature steps for 10 min and measured after recovering room-temperature (RT).

2.2.2 Synchrotron Radiation

When a charged particle is forced to move on a curve trajectory it radiates electromagnetic radiation in a cone in the direction of its motion, called synchrotron radiation. In a Synchrotron charged particles move with relativistic speed and generate radiation highly collimated, extremely intense and extends over a broad energy range from the infrared through the visible and ultraviolet, into the soft and hard x-ray regions of the electromagnetic spectrum.

At the beginning the synchrotron radiation was considered only as a problem for particle physics experiments since it is the major source of energy loss in high energy particle accelerators. The first generation synchrotron radiation facilities were used in a parasitic way. The charged particles (electrons or positrons) accelerated in a linear accelerator with an energy of several millions of electron (MeV), were injected in a circular accelerator, like storage ring. In the storage rings, the particles were accelerated to higher energy by the radio frequency electric field and forced to follow circular paths under the action of magnets placed along the circumference (bending magnets) and loose part of their energy, emitting synchrotron radiation. The energy lost in this way is fully regained in passing through the radio frequency cavities. A schematic picture of a storage
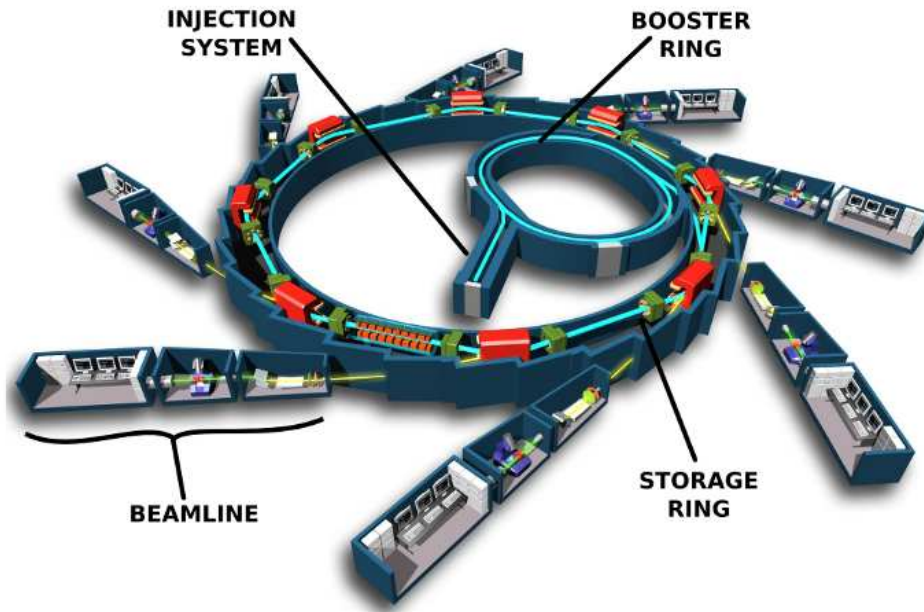
ring is reported in Fig. 2.7.

Figure 2.7: Schematic picture of a synchrotron radiation light source.

From the second generation of synchrotron radiation facilities the storage ring were made to generate synchrotron light using bending magnet. The use of structures with high magnetic field, like wigglers and undulators, placed in straight sections has made possible the realization of the third generation of synchrotron radiation sources like European Synchrotron Radiation Facility (E.S.R.F.) and ELETTRA.

The main properties of the emitted radiation depend on the characteristics of the storage ring and can be summarized in:

- high intensity;

- very broad and continuous spectral range from infrared up to the hard x-ray region;

- natural narrow angular collimation;

- high degree of polarization;

- high brilliance of the source.

In order to estimate the collimation of a synchrotron radiation source, we first consider a non relativistic electron, with a speed much lower then the speed of light $(v \ll c)$. In this case the emitted pattern is similar to the one of an oscillating dipole with its maximum of intensity in the direction perpendicular to the acceleration and do not depend on the electron speed. When the speed of charged particles is near the speed of light $(v \approx c)$ the radiation is collimated into a cone in the direction of motion (Fig. 2.8)[143], and the vertical half-opening can be written as

$$\psi \approx mc^2/E = \gamma^{-1}$$

It is easy to see that the angle decreases increasing energy, for an storage ring of energy $E = 1$ GeV the angle is $\psi \approx 0.5 \; mrad$.
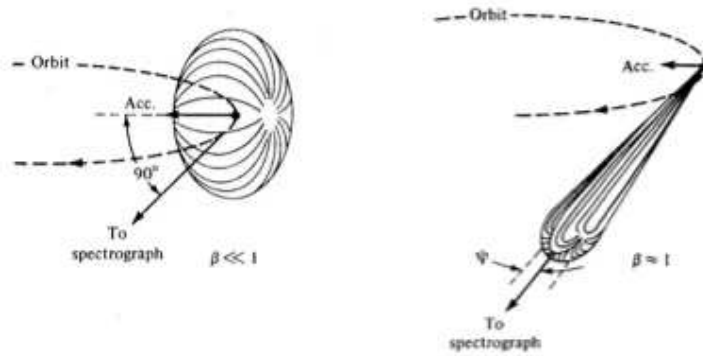

Figure 2.8: Collimation of emitted light from accelerated electrons with different energies.[143]

Another important characteristic of synchrotron radiation is the continuos and broad spectral range. In Fig. 2.9 (right panel) the spectral distributions, as a function of energy of the storage rings, are reported.

Supposing to have a single electron in the storage ring and to record the emitted light during the motion, a short pulse of radiation will illuminate the detector when the electron passes through that point of the orbit with a frequency equal to the frequency of the period of the motion $\omega = v/2\pi R$. At high frequency a cutoff will be present because the detector will receive the radiation emitted by the electron along the arc $2/\gamma$ (Fig. 2.9, left panel). This originates a pulse of non zero duration given by the difference between the time for the elec-
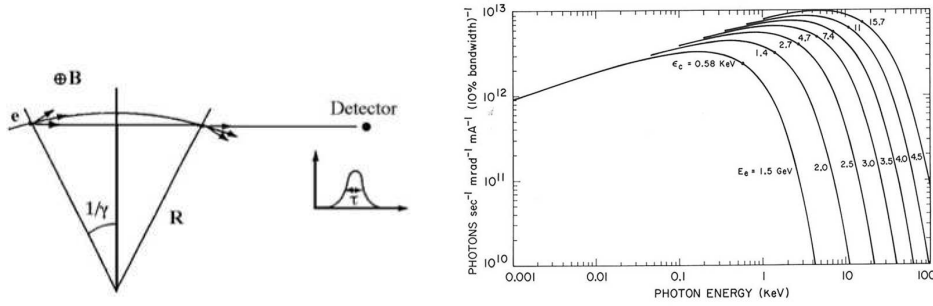
Figure 2.9: Left panel: schematic view of electron path and emitted light that illuminates the detector. Right panel: spectral distributions as a function of energy of the storage rings

tron to travel along the arc and the time for the light to travel along the chord subtended by this arc. The frequency cutoff associated at this configuration can be written as

$$\omega_{cutoff} \approx c\gamma^3/R$$

. Therefore, in principle, synchrotron radiation from one electron consists of a discrete spectrum of closely spaced lines up to ω_{cutoff}. In practice, the spectral distribution coming from many electrons is continuous due to the statistical oscillations of the electrons around the main orbit, to the fluctuations in their kinetic energy and to the statistical nature of the emission itself, all effects that lead to a line broadening of each harmonic.

2.3   Microscopies

Differently from the electron spectroscopy, that study the electronic configuration of the system, the microscopies investigate the morphology and arrangement of the surface. The microscopy field con be divided in three different branches, based on three different kind of probe: optical, electron and scanning probe microscopy. In the first and second techniques electromagnetic radiation (optical) or electron beam interact with samples and the subsequent collection of scattered radiation (for diffraction, reflection, or refraction effect) or another signal creates an image. Scanning probe microscopy involves the interaction of a scanning probe with the surface of the object of interest.

In this section the techniques used for the morphological characterization are presented.

2.3.1 Atomic Force Microscopy

The *Atomic Force Microscopy* (AFM) technique was developed from the *Scanning Tunneling Microscopy* (STM). The STM needs conductive samples to employ the tunneling current generated between sample and probe. The AFM investigates the morphology at the nanometric scale using the interaction forces between sample and probe. The characteristic allows to use this technique with non conductive samples like ceramic thin films, amorphous materials, glass, biological or synthetic membranes, polymers, semiconductors and also metals.

The AFM technique is based on the interaction between the sample and probe. The probe is composed by a micro-metric cantilever and a tip. The tip is composed by hard conductive materials and interacts with the surface of the sample; the interaction forces (F) produce a deflection of the cantilever (Δz), that responds like a spring with elastic constant k ($F = k\Delta z$). Measuring the deflection it is possible to obtain the morphology of the surface. The geometry of cantilever and tip are pictured in Fig. 2.10. To measure the deflection of cantilever the top part is covered with a high reflective material and illuminated with a laser beam; the reflected beam is measured by a photodiode with four quadrants and it is possible to estimate the variation in cantilever position measuring the beam position on the photodiode.

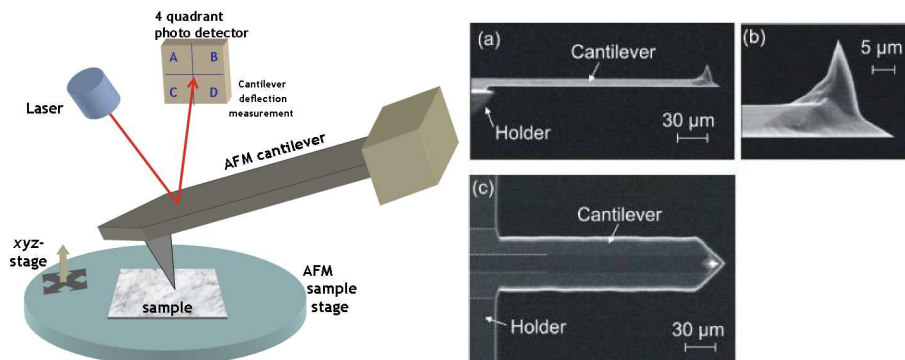**Figure 2.10:** Left panel: setup and components of a AFM instrument. Right panel: SEM view of a cantilever with tip.

Working Mode

The interaction between tip and sample depends by the distance. There are three different operating modes for AFM;

- *Contact:* the tip is in *contact* (short distance) with the sample and the forces are repulsive,

- *Non-Contact:* the interaction is weakly attractive and the tip vibrates at fixed distance to the sample,

- *Intermittent (or Tapping):* the tip oscillates at different distances from the sample and the interaction depends to the distance.
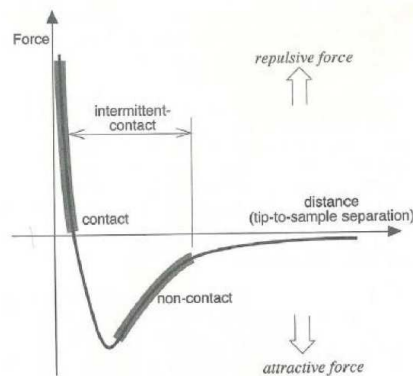

Figure 2.11: Lennard-Jones potential as a function of atoms distance and characteristic AFM operating modes.

The interaction between tip and sample is "governed" by Lennard-Jones potential (Fig. 2.11).

In the *Contact mode*, the tip and the sample are at distance below the equilibrium point (first part of Lennard-Jones potential, Fig. 2.11), and the forces between tip and sample are completely repulsive. This operating mode is used with hard samples because the lateral forces between tip and sample can damage the surface of the sample.

In the *non-Contact mode*, the tip oscillates above the sample at its resonant frequency and the amplitude of oscillation is typically a few nanometers. The Van der Waals forces acts to decrease the resonance frequency of the cantilever. In order to maintain a constant oscillation amplitude of frequency, the average distance between tip and sample is adjusted; measuring this distance a topographic image of the surface can be obtained.In ambient conditions, most samples develop a liquid meniscus layer, then this mode is used in particular with soft, hydrophobic samples and in vacuum environment.

In the *Tapping mode*, the cantilever is driven to oscillate up and down at near its resonance frequency with an amplitude of 100-200 nm. The interactions between tip and sample, when the tip is close enough to the surface, cause a variation of the oscillation. Measuring the deflection and variation produced during the contact phase, the morphological image of the surface is produced. This method is the best compromise in order to obtain high resolution without damaging the surface sample and is used in this work to measure the arrangement and the size of the iron oxides nanowires.

Resolution and tip convolution
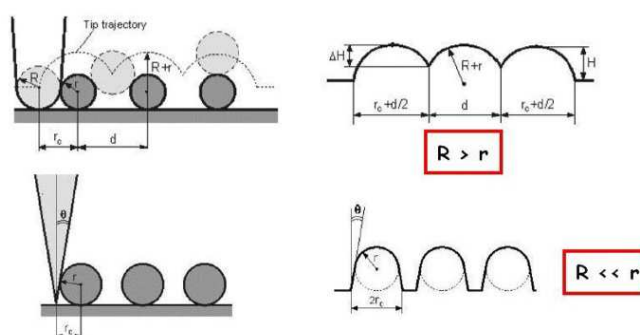
Figure 2.12: Schematic representation of AFM resolution as a function of the radius of curvature of the tip.

The resolution in z direction is correlated to the beam deflection and it is possible to obtain resolution in z direction about 0.1 nm. In the x, y plane the most important factor that influences the lateral resolution in AFM technique is the radius of curvature of the tip. In Fig. 2.12 is reported an example of the images produced by tips with radius of curvature larger and smaller than the size of sample.

In the first case the tip does not resolve the single particle on the surface and the image is a convolution between the dimension of the tip and particle. In the second case, the radius of curvature of the tip is much smaller than the particle size and the obtained image gives directly information about the size of particles. The radius of curvature of the tip depends on the fabrication. In standard tips, the radius of curvature is about $5 - 60$ nm.

In this work all the AFM images were acquired with standard SiO_2 tips with nominal radius of curvature of 8 nm.

2.4   Sample Synthesis

2.4.1   Nanowires synthesis

A wide range of synthetic pathways have been exploited for the development of nanostrucures due to their potential applications.[148–153] Research is focused on the development of soft[154–162] and hard[163–186] templates in order to control nanostructures properties. For preparation of ordered nanostructure arrays, a hard template has some advantages in comparison with other synthesis method. In particular, the Hard-Template method provides definite advantages such as specific topological stability, veracity, predictability, controllability, and large scale production. This method allows to control in principle size and macroscopic properties of nano-tubes, nano-flakes, nano-sheets, and nano-particles.[24,25] Furthermore, ad-hoc designed structures may lead to iron-oxides with significantly improved performances both in terms of specific capacity and of rate capability, i.e., very important parameters in order to evaluate the suitability of the materials for battery applications. Between different materials, supramolecular templated mesoporous silica materials have been indicated as perfect candidates to serve as hard templates due to their uniform mesocavums, large surface areas and lare pore volumes.[169–182,187]

Hard-Template, mesoporous silica (SBA-15) was synthesized by the sol-gel method using a nonionic surfactant (EO20PO70EO20, average Mw=5800, Aldrich), where EO and PO denote the ethyleneoxide and propyleneoxide units. Tetraethyl orthosilicate was added to the surfactant aqueous solution in which the pH was adjusted to 1.0 using 36 % HCl. The mixture was then stirred at 35 °C for 24 hours, and kept in a convection oven at 80 °C for 24 hours. The reactant was filtrated, and the precipitate was annealed at 600 °C in a muffle. For embedding Fe_2O_3 in mesoporous silica, $Fe(NO_3)_3 \cdot 9H_2O$ 0.01 M was dissolved in 50 ml of ethanol and added to 1 g of SBA-15. The slurry was stirred at room-temperature (RT) and then dried at 40 °C for 1 week. The so obtained brown colored powder was sintered at 550 °C for promoting NO_x decomposition and dehydration. The powder was afterwards etched by 2M NaOH solution for 6 hours, washed and filtered several times. Finally, pure nanowires-agglomeration of Fe_2O_3 was obtained after drying at 60 °C.

For the spectroscopic and microscopic investigations, the nanowired powder was dissolved in ethanol solution, put in a ultrasound bath for 5 minutes and
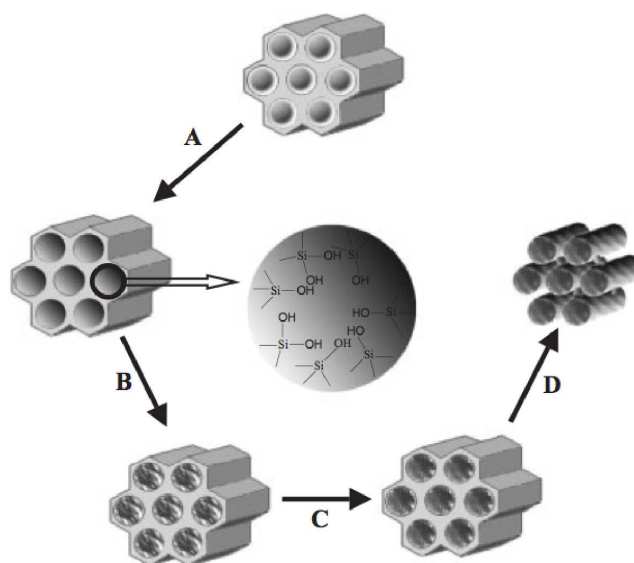
Figure 2.13: Reconstruction of the different steps of the hard-template method. A) Microwave digestion [188], B) infiltration with inorganic precursors, C) calcination, D) etching by HF or NaOH. [24]

deposited, by Pasteur pipettes, on different substrates. For the spectroscopic characterization two different substrate have been used: polycrystalline Cu foil and freshly cleaved HOPG. The solution was dried out in air before insertion in UHV chamber. In order to remove the residual ethanol and to clean the sample, once inserted in UHV the system was kept at 80°C overnight.

In order to simulate the reaction in the Lithium-ion batteries, the iron oxide nanowires were exposed to lithium vapor, in UHV environment, depositing Li alkali metal from commercial Li dispenser (SAES Getter), described in the previous section (Sec. 2.2). The Cu substrate does not interact with deposited Lithium and the obtained results (presented in Chap. 3) give informations about the interaction between Lithium atoms and iron oxide nanowires. The HOPG is the classical anode in lithium-ion batteries and has been used as substrate with nanowires to simulate a new kind of electrode.

2.4.2 Graphene Nanoflakes

Graphene nanoflake inks are prepared via low-power ultrasonication of graphite in N-Methyl2Pyrrolidone (NMP). The choice of graphite exfoliation in NMP is set by the need of having the best contact at the inter-flake junctions upon de-
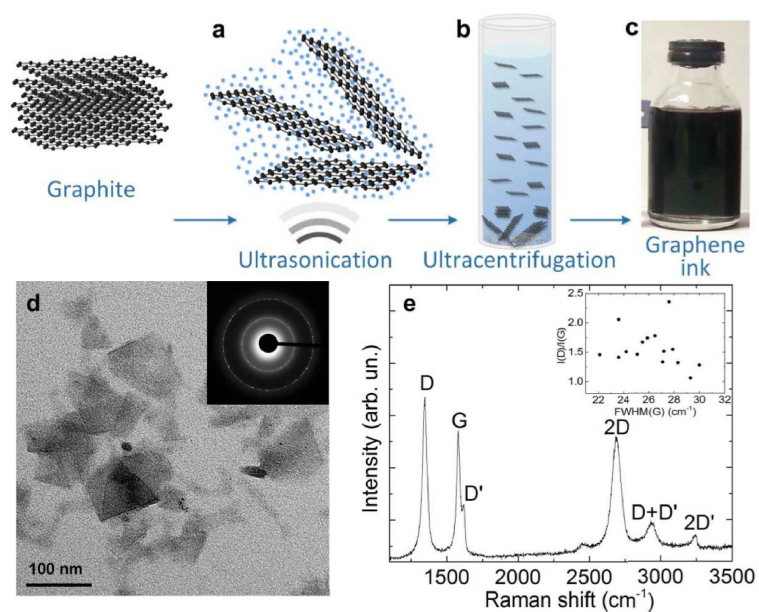
Figure 2.14: Production and characterization of graphene nanoflakes ink. a) Liquid phase exfoliation of graphite via ultrasonication b) separation of Small lateral size flakes from thick and large flakes via ultracentrifugation c) Ink solution d) Bright field TEM image of graphene flakes at higher magnification e) Raman spectrum measured at 532 nm laser excitation wavelength for a representative flake obtained via sedimentation-based separation.

position on the electrode, which could be affected by the surfactant coverage in aqueous solutions.[189,190] During the ultrasonication process, the strong hydrodynamic shear-force, created by the propagation of cavitons, i.e., the creation and subsequent collapse of bubbles or voids in liquids due to pressure fluctuations, induces exfoliation of the graphitic flakes[191]. However, the exfoliation process produces a heterogeneous dispersion of thin/thick and small/large graphitic flakes[125]. In order to obtain graphitic flakes with small lateral size, after exfoliation, the solvent-graphene interaction needs to balance the inter-flakes attractive forces that cause re-aggregation. The sorting of small lateral size graphene nanoflakes is carried out by sedimentation-based separation (SBS).[125,189,192] The SBS technique separates graphitic flakes into fraction on the basis of their sedimentation rare. This step enables the control of the lateral dimension of the nanoflakes. The graphene ink, Fig. 2.14-c, contains flakes having variable dimensions in the range 30-100 nm as shown by the TEM analysis, reported in Fig. 2.14-d. The diffraction pattern shows polycrystalline rings demonstrating that the flakes are crystalline.[193] Fig. 2.14-e plots a typical Raman spectrum of the flakes deposited on Si/SiO2. The spectrum shows significant D and D' intensity and the combination mode $D + D'$ and the G and 2D peaks that are fingerprints of graphene.[193]

Chapter 3

Iron Oxide Nanowires Characterization

In this chapter, the morphologic and spectroscopic characterization of the Iron Oxide nanowires is presented. The size and the arrangement of the nanowires were studied through microscopy techniques, *Atomic Force Microscopy* (AFM) and *Scanning Electron Microscopy* (SEM), that are able to show the morphology of the nanowires surface with high resolution. The spectroscopical characterization was carried out through *X-Ray Photoemission Spectroscopy* (XPS) and *Near Edge X-Ray Absorption Fine Structure* (NEXAFS) measurements. The XPS technique gives information about the chemical state of the compound through the photoemission of electrons from filled states, whereas the NEXAFS technique, studying the transition between the filled and empty state, gives information also on the different phases of the system, reflected in absorption lineshape.

3.1 Morphological and Structural Characterization

The morphological characterizations were performed with *Atomic Force Microscopy* and *Scanning Electron Microscopy* at the SNN-Lab. The nanowires were deposited on mica (Muscovite mica, $KAl_2(AlSi_3O_{10})(OH)_2$), substrate for the AFM measurements and on Si for the SEM measurements. The mica substrate presents very low roughness and a polar surface that interacts weakly with sample and guarantees good stability during the measurements. The Si substrate is indicated for SEM measurements in order to have good conductivity between

the sample and ground.

3.1.1   Atomic Force Microscopy

The AFM images from different areas of the iron oxide nanowires are reported in Fig. 3.1 and Fig. 3.2. The images show aggregated particles with micrometer size. An 3D image of micro-sized agglomerate is reported in Fig. 3.1 (left panel): the micro-agglomerate shows three different parts, a disordered part that covers half of the visible surface (top part) and two well distinguishable high ordered parts, one with nanowires aligned parallel to each other and parallel to the substrate (right bottom part) and the other with vertically aligned nanowires (triangular structure on left bottom part) (Fig. 3.1 left panel). The magnification of the vertically aligned nanowires is shown in the 2D image (Fig. 3.1 right panel) that shows the parallel-vertical alignment of the nanowires.
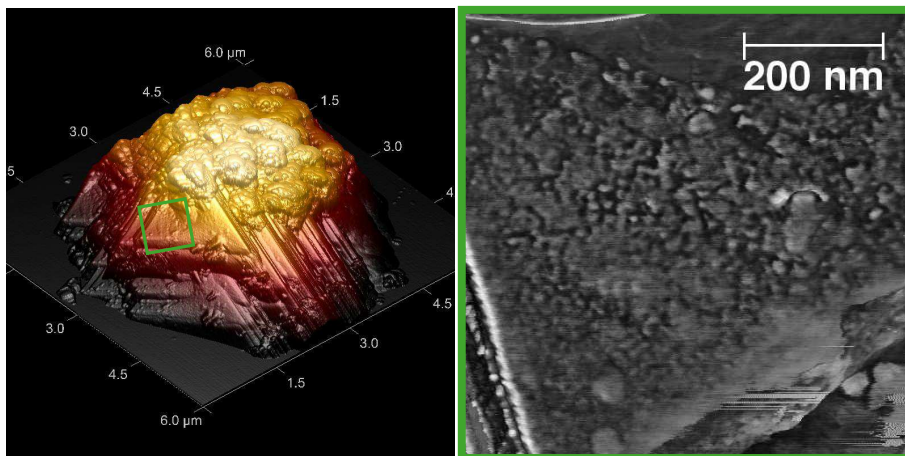
Figure 3.1: AFM image for iron oxide nanowires: tridimensional view of micro-agglomerate with ordered parts (left panel), magnification of vertical aligned nanowires (right panel).

Different agglomerates show different ordered parts on the surface. An example of ordered part at different magnifications is reported in Fig. 3.2. The images show a 1 μm x 1 μm area (left panel) with nanowires in parallel configuration and, in the top-right panel, the high resolution image shows the alignment and the size of the nanowires. The distribution size of the nanowires is reported in Fig. 3.2 (right panel): the distribution shows an average size of 12 nm $\pm$ 2 nm. Taking into account the convolution of the expected wire cross-section

(8 nm) with the tip radius (nominally 8 nm) within the errors, this result is in agreement with the expected size after the chemical preparation. It is possible to observe that the distribution shows nanowires with a 18 *nm* size: it can be explained by considering the overlap of some nanowires that the tip does not resolve.

Figure 3.2: **AFM image of ordered iron oxide nanowires at different magnifications (left and central panel), distribution width of observed nanowires (right panel).**

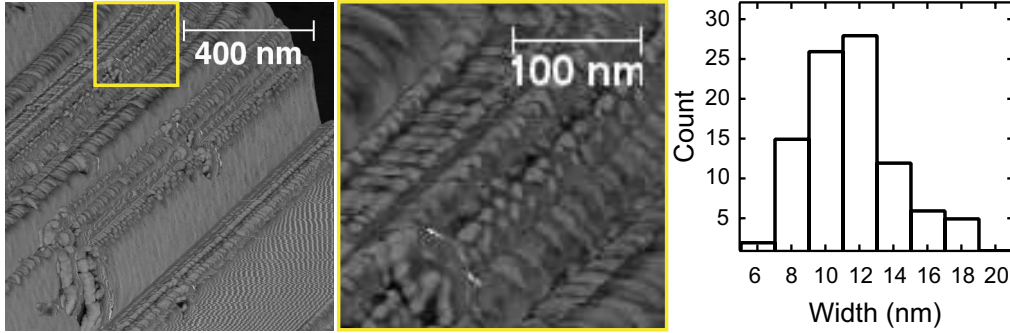### 3.1.2 Scanning Electron Microscopy and X-Ray Diffraction

The SEM images acquired at different magnifications of the nanowires on Si are reported in Fig. 3.3 and 3.4. The images show different aggregation of the nanowires. We observe bundled structures with an average width of 400 *nm*, as result of the hard-template procedure. The absence of single isolated nanowires suggests that the aggregation in bundles is a direct effect of the preparation procedure. The length of the bundles is variable in a wide range, from hundreds of nanometers to several microns. In Fig. 3.3 (left panel) an example of an aggregation in bundle with a length of 8 *μm* is reported. A zoomed image of the central part of that bundle is reported in Fig. 3.3 (right panel). The *thick-bundle* is composed by *micro-bundles* composed themselves by aggregated and ordered parallel nanowires. On the bundle surface, we can distinguish disordered fragments of the nanowires; this is in agreement with the AFM measurements that show some disordered parts on the sample surface.

In Fig. 3.4, another example of nanowires agglomerate is reported; in particular, the surface is composed by disordered nanowire fragments, as observed before. At higher magnification (Fig. 3.4 right panel) it is possible to observe
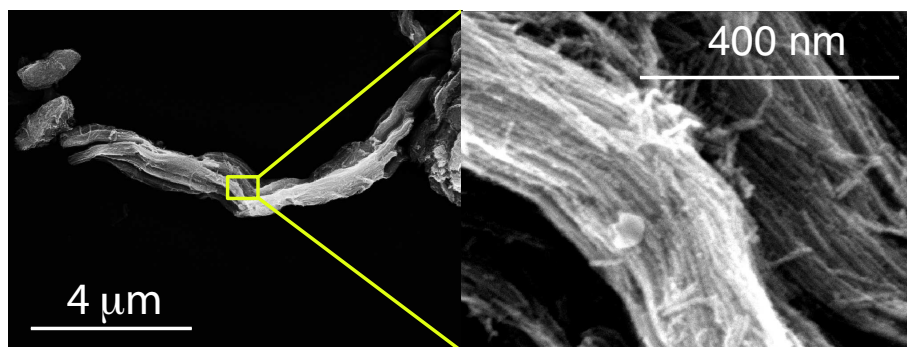
Figure 3.3: **SEM image for iron oxide nanowires bundles at different magnifications.**
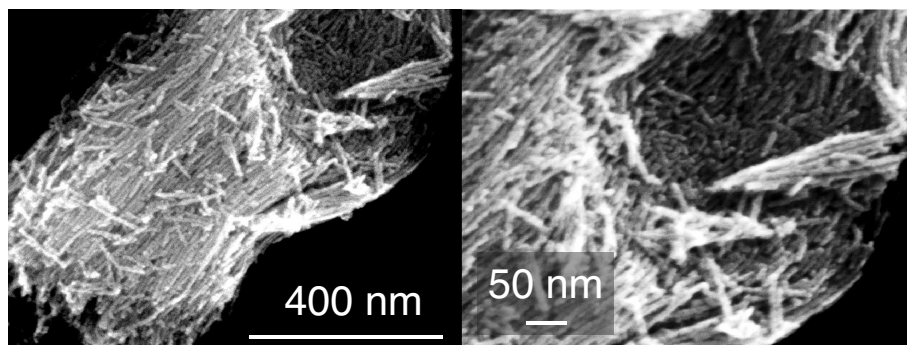
Figure 3.4: **SEM image for iron oxide nanowire at different magnifications.**

that the internal part of the agglomerate presents ordered structure with parallel nanowires. This result is in agreement with the observed ordered part in AFM, and also suggests that the hard-template method can be used to produce ordered nanowires.

Fig. 3.5 (left panel) shows a SEM image of another ordered part of the sample, where the nanometric size of the nanowires is visible. A statistic evaluation of the size, performed on the SEM image of Fig. 3.5, is reported in Fig. 3.5 (right panel). The nanowires produced by the hard-template method should in principle have a size of 8 nm. Analyzing the size distribution it is possible to estimate the width of nanowires as 8.0 ± 0.5 nm. This result is in excellent agreement with the expected size of the nanowires.

In order to determine the crystalline structure of the nanowires, an XRD
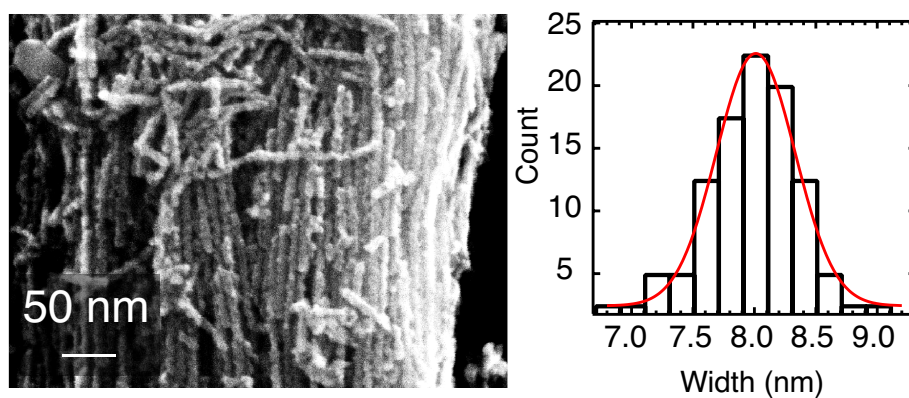
Figure 3.5: SEM image (left panel) and Statistic of nanowires width (right panel)
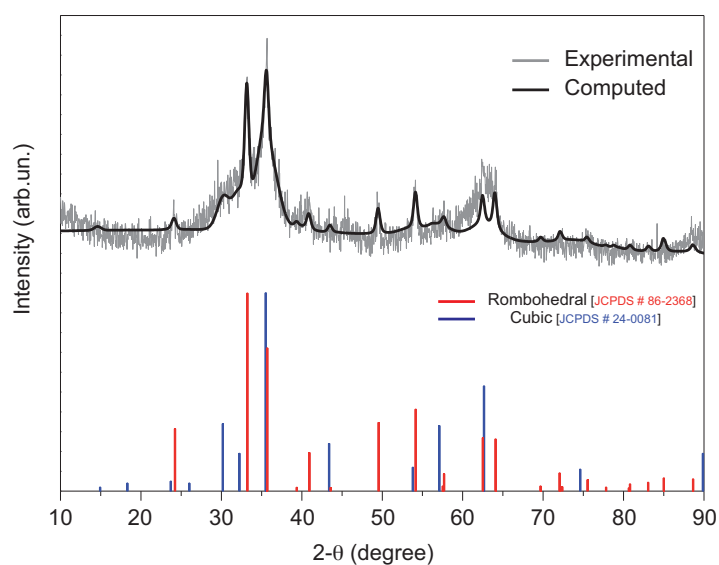
Figure 3.6: XRD experimental (gray spectrum) and computed spectra (black spectrum); expected XRD patter for the rhombohedral (red bars) and cubic (blu bars) crystalline phases (bottom).

characterization was performed at the Chemistry Department with a Cu K-α source. Considering the chemical procedure to obtain the nanowires, they should present a Fe_2O_3 stoichiometry. The Fe_2O_3 compounds can present two different crystalline structures, *alpha* (α-rhombohedral) and *gamma* (γ-cubic) phases. The pattern of the two crystalline phases are reported in Fig. 3.6 with red and blue bars, for the rhombohedral and the cubic phases, respectively. The XRD pattern acquired on the nanowires and the Rietveld refinement are reported in Fig. 3.6 with gray points and black solid line, respectively. The Rietveld refinement on the experimental data reveals a mixed phase with a 50:50 ratio between the α and γ phases.
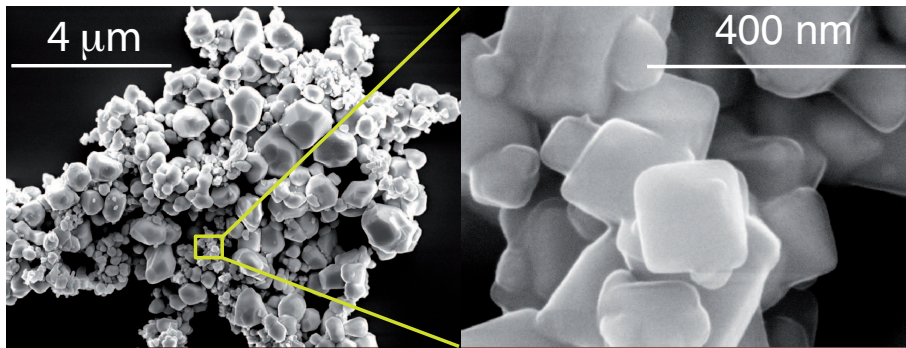
Figure 3.7: SEM image for Fe_2O_3 bulk-like powder.

The SEM and XRD characterization was performed also on a Fe_2O_3 bulk-like powder deposited on Si. The SEM images (Fig. 3.7) show a system composed by microparticles with different sizes and irregular structure. Because the irregular shape, the microparticles' surfaces were approximated with a circumference in order to estimate the average size of the powder. The distribution of microparticles' width is presented in Fig. 3.8 (right panel): analyzing the distribution we can estimate the average diameter around 300 nm and a wide range from 100 to 1000 nm. The XRD measurements (Fig. 3.8) obtained for the microparticles (left panel) presents a highly crystalline pattern where the observed peaks correspond to the characteristic peaks of a rhombohedral phase.

The SEM images and the statistical analysis of the nanowires reveal that the hard-template method is the right procedure to produce highly-ordered nanowires with the same size within a narrow distribution. The XRD pattern of the nanowires presents a mixed α/γ-phase differently from the bulk-like
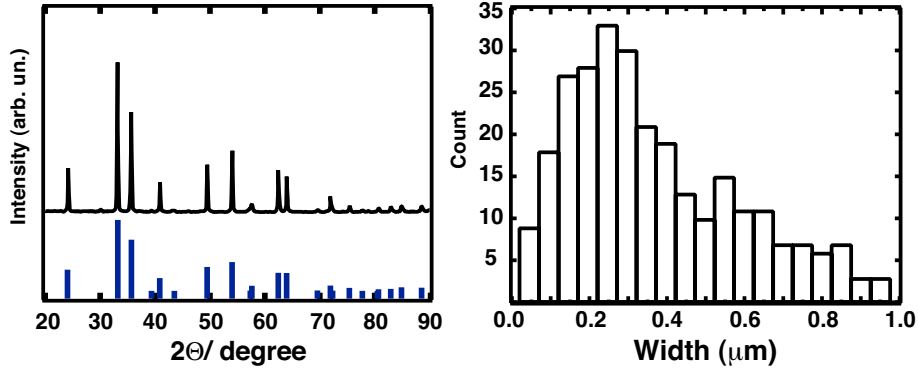
Figure 3.8: XRD experimental (black line) and expected rhombohedral phase (blu bars) pattern (left panel) and size distribution (right panel) of Fe$_2$O$_3$ bulk-like powder.

microparticles that presents a perfect α-phase.

The mixed phase observed in the nanowires can be attributed to a variation of the crystal structure from the bulk to the surface due to growth procedure and to the nanometric size of the nanowires. The XRD technique is bulk sensitive for this size, because the x-rays probe the whole wire body, such as to single out also the bulk-like signal associated to the core of the NWs with the expected α-phase. We will see in the following section how the very surface sensitive x-ray spectroscopy technique will confirm the attribution of the γ-phase to the NW surface.

3.2 Spectroscopic Characterization

The chemical state of a compound can be obtained by analyzing the XPS and NEXAFS spectra. The different ionic state and phases of the Iron Oxide compounds will be studied, by performing a detailed comparison between our experimental data and the theoretical and experimental data reported in literature, to attribute the right ionic state and to discriminate the crystalline phases of the system. In Iron Oxide compounds, from the Fe-2p, Fe-3p core levels and Fe L_{23}-edge absorption spectra it is possible to obtain information about the ionic state of Iron and to discriminate if the system is a Fe$_2$O$_3$, Fe$_3$O$_4$ or FeO[194], and from the Oxygen K-edge absorption spectrum it is possible to discriminate the different α and γ phases of the Fe$_2$O$_3$ compound. An analysis of the Iron Oxide nanowires is reported in this section with the aim of obtaining a complete

overview of the properties of the system.

3.2.1   XPS of the Fe core-levels

The XPS measurement of the Fe-$2p$ core levels of the nanowires is reported in Fig. 3.9 (left panel). The Fe-$2p$ spectrum presents two main peaks at 711.26 and 724.64 eV, and two satellites S_1 and S_2 at 719.26 and 732.64 eV, respectively: the two main peaks represent the Fe $2p_{3/2}$ and $2p_{1/2}$ core levels and the splitting of 13.4 eV is due to the spin-orbit interaction. The two main peaks present an asymmetric and broadened lineshape due to the contribution of two different processes, a multiplet splitting induced by the photo-hole in the $2p$ initial state[75], and multiple ionization typical of oxides[76,77,195]. The S_1 and S_2 satellites, located at ≈ 8 eV higher binding energy with respect to each main peak, are associated to the charge-transfer processes in the final states after photo-excitation, because of the attraction on the d orbitals which generates a screened final state in the system.[67,196]
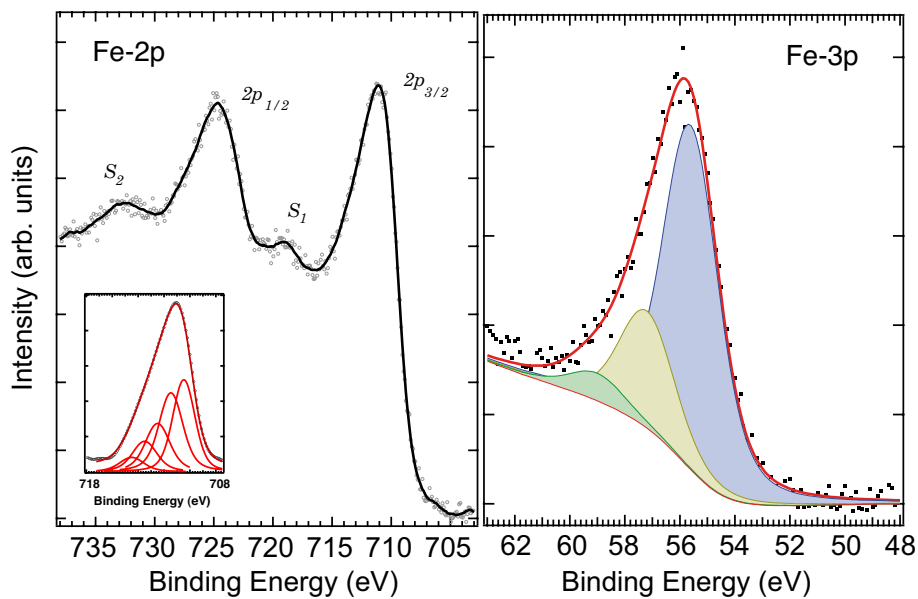
Figure 3.9:   XPS measurements of Iron $2p$ (left panel) and $3p$ (right panel) core levels of the nanowires.

In the Fe-$2p$ core levels, the contribution of multiple ionization is negligible and the multiplet splitting is the most important effect in the asymmetry of the peaks. In order to take in account this effect, the Fe-$2p_{3/2}$ was fitted with five

peaks following subtraction of the background (inset in Fig. 3.9, left panel). We used Gaussian curves because the intrinsic lifetime of each $2p$ core level is high, thus the Lorentzian contribution in the lineshape is negligible with respect to the intrinsic experimental resolution (Gaussian width $\approx$ 1.2 eV). The two main peaks of the fit are separated by 1 eV and have approximately the same width and shape; the other peaks are fitted with a decreasing intensity and have to similar shape and width. The intensity distribution of these peaks depends on the multiplet splitting of the Fe-$2p$ core line. The result obtained for this compound is in agreement with the multiplet structure expected for p core levels in the Fe^{3+} ion.[61,75]
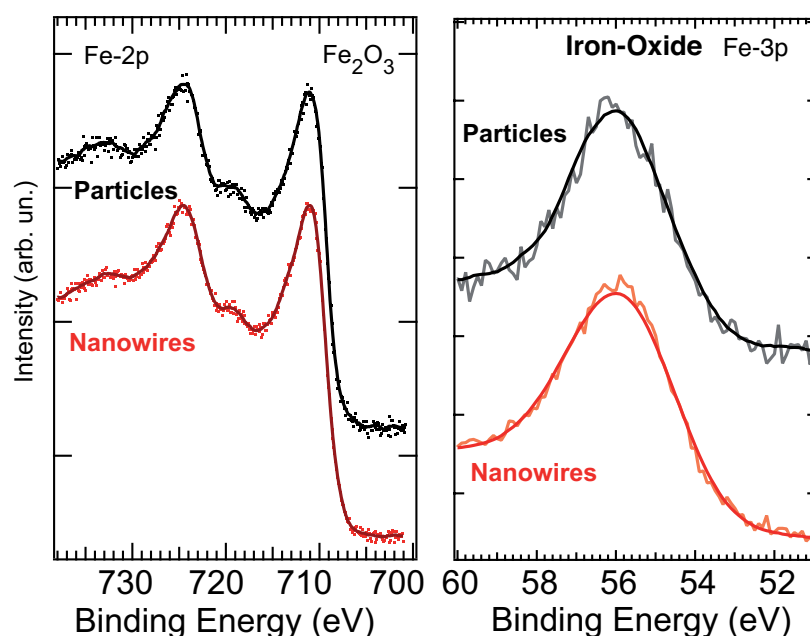
Figure 3.10: **XPS measurements of Iron** $2p$ **(left panel) and** $3p$ **(right panel) core levels of microparticles (black curves), compared with nanowires (red curves). Experimental data (dot) and smoothed curved (continuos line).**

The spectrum of the Fe-$3p$ core level is reported in Fig. 3.9 (right panel). The Fe-$3p$ spectrum presents an asymmetric broadened peak centered at 56 eV. The Fe-$3p$ line shape is asymmetric and broadened towards high binding energy because of many effects, including spin-orbit interaction, multiplet splitting and multiple ionization.[195] Among all these phenomena, the dominant one

is the spin-orbit interaction, which gives rise to an energy splitting of about 1 eV between the $3p_{3/2}$ and $3p_{1/2}$ peaks, comparable to the experimental energy resolution. Taking into account all these phenomena, and considering that differently from the $2p$ core-levels, in the $3p$ core-level the lifetime of the state is low and the Lorentzian contribution is not negligible, the Fe-$3p$ core level was fitted with three Voigt curves (Gaussian-Lorentzian lineshape) peaks presenting 1.0 eV Lorentzian width and 1.2 eV Gaussian width. The fitting curve well reproduces the experimental lineshape.

The XPS data for the bulk-like microparticles are reported in Fig. 3.10, in comparison with the nanowires. The Fe-$2p$ spectrum of the microparticles presents the Fe $2p_{3/2}$ and $2p_{1/2}$ core levels and the associated satellites at the same energy of those observed in the nanowired system. The broadened and asymmetric lineshape of Fe-$3p$ core level, centered at 56 eV, observed for the microparticles is the same of that observed in the nanowires.

The lineshape of iron oxide spectra are characteristic for different oxidation states of Fe, in particular the energy position of the Fe-$2p$ core levels and the satellite peaks are different for different compounds. Our analysis of these features allow us to determine the exact oxidation state of Iron. In particular the Fe-$3p$ core level is characteristic for Fe^{3+} and the lineshape of Fe-$2p$ is characteristic for the Fe_2O_3 compound, confirming the expected stoichiometry.[194]

3.2.2   Near Edge X-Ray Absorption Fine Structure

The NEXAFS measurements at the Fe-L_{23} and O-K edges were carried out at beam line BEAR at Elettra, Synchrotron Radiation Facility in Trieste. The spectra obtained for both nanowires and microparticles are reported in Fig. 3.11.

The absorption spectra obtained from the Fe L_{23}-edges are reported in Fig. 3.11 (Left Panel). The spectra, acquired with photon energy spanning between 700 and 730 eV, present two main features centered at 710 and 723 eV: these two main structures represent the transition from the Fe-$2p_{3/2}$ and Fe-$2p_{1/2}$ filled states to hybridized empty states, and the energy splitting of 13 eV is due to the spin-orbit interaction in Fe-$2p$ levels. Both resonances present two peaks at 710.5 and 709 eV for the L_3, and 722.8 and 724.5 eV for the L_2, respectively. These two main peaks cannot be directly related to the Fe-d empty orbitals in t_{2g} and e_g subsets. The intensity ratio, the splitting and the sharpness of these peaks are dependent on the crystal field and electronic interactions, the

lineshape is also influenced by charge transfer processes reinforcing the splitting of the d orbitals and modifying sharpness and intensity of the peaks, especially at the L_3 edge.

The lineshape of bulk-like microparticles shows, at the L_3 edge, two sharp peaks located at 710.4 and 709 eV. In the nanowires, the two peaks are located at 710.5 and 709 eV. Taking in account the relationship between the atomic arrangement in solids, crystal field and in accord with the XRD results, the variation of the lineshape can be attributed to the size of the nanowires and their quasi-$1D$ structure.

The Iron L_{23} absorption spectral features observed in both systems indicate the same oxidation state; furthermore, the Iron L_{23}-edges reproduce perfectly the lineshape of the Fe_2O_3 system[63] and confirm the results obtained with XPS.
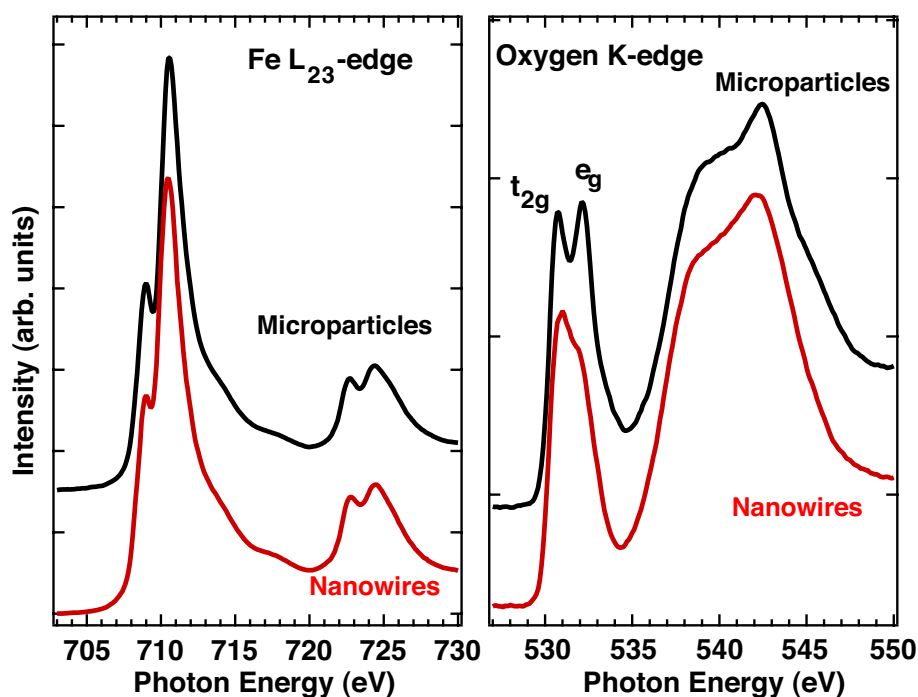

Figure 3.11: NEXAFS measurement of Iron L_{23}-edge and Oxygen K-edge for the nanowires (red curves) and the bulk-like microparticles (black).

In Fig. 3.11 (right panel) the absorption spectra from the Oxygen K-edge for the iron oxides nanowires and microparticles are reported.

The absorption spectrum of Oxygen K-edge shows, in the range between

530 and 534 eV, transitions from the O-1s level to unoccupied states resulting from O-2p and Fe-3d valence band hybridization. In particular the O-2p/Fe-3d hybridized states present mostly 3d character and are split into t_{2g} and e_g states by the ligand field. In the second region, between 534 and 550 eV, the spectrum shows the transition from O-1s state to unoccupied states resulting from O-2p and Fe-4s ad 4p states hybridization which originates from a scattering resonance due to the multiple scattering processes of the final state photoelectron within the cage of the first oxygen shell around 540 eV.[74,197]

The Oxygen K-edge spectrum from the bulk-like microparticles shows a splitting of 1.4 eV between t_{2g} and e_g states, located at 530.7 and 532.1 eV respectively. In the nanowires the t_{2g} state is located at 531.0 eV and the e_g state at 532.1 eV, with a splitting of 1.1 eV. In the higher energy region the lineshape of the spectrum of the nanowires and microparticles system is very similar, in both systems it is possible to recognize the same peaks located at 538.5 and 542 eV. In the microparticles an additional characteristic peak around 545 eV can be well identified. The different energy of the t_{2g} and e_g states is associated to the different crystalline phases and different contribution from the ligand field[74,197,198]; in according with the XRD measurements, the nanowires show a characteristic lineshape for the γ-phase in the cubic crystal system and the microparticles show a characteristic lineshape for the α-phase in the rhombohedral crystal configuration.[74,197,198]

3.3   Final Considerations

The morphologic and spectroscopic characterization performed on the iron oxide nanowires reveals the size, shape and chemical composition of the system. The AFM and SEM analysis show ordered structures composed by parallel nanowires with a variable length, from hundreds of nanometers to several microns, and 8 nm width, furthermore the XRD results show a mixed $\alpha + \gamma$ crystalline phase of a Fe_2O_3 compound. The analysis of the Iron and Oxygen core-levels, with XPS and NEXAFS techniques, confirm the Fe_2O_3 stoichiometry and the γ phase of the nanowires. The differences observed between NEXAFS and XRD results can be attributed to the different sampling depth associated to their respected photon energy. The XRD experiment shows the signal of the whole nanowire from the surface to the bulk. In the NEXAFS measurements the escape depth of excited electron is $\approx$ 2 nm, thus we can assume that the NEXAFS technique

gives information about the coordination state of the iron and oxygen atoms near the surface. Thus, as anticipated in the XRD analysis, the two different α and γ phases obtained for the nanowires can be attributed to the coordination state of the iron in bulk and near the surface, respectively.

Chapter 4

Reduction processes

In the previous chapter, the iron oxide system was described from the morphological and spectroscopical point of view and a complete overview on the arrangement and the crystalline phase was obtained. In this chapter, the results of the reduction processes under thermal treatment and lithium vapor exposure in UHV are presented. The nanowires can be considered as new important alternative in lithium batteries technologies, thus an accurate analysis of the behavior of interaction with lithium ion and the behavior at different temperatures is necessary. Furthermore, the size and shape of the nanowires can influence the kinetics of the reduction processes so a comparison between the nanowires and bulk-like microparticles is presented in order to clarify the role of the size in the kinetics of the reduction processes. The nanowires were deposited on inert substrates, clean polycrystalline Cu foil and cleaved HOPG (standard material for anode in lithium-ion batteries) in order to study also the contribution of the substrate in the lithiation process.

4.1   Temperature-induced Reduction

The reduction process and the phase transition of the iron oxides under annealing are known in literature for three-dimensional (3D) structures.[199] The same properties have never been studied for low-dimensional systems, in particular the reduction process could proceed with a different kinetics due to the reduced size of the system. In this section a study of the oxidation state of the iron oxide nanowires is presented, by analyzing the Fe $2p$ and $3p$ core levels, and the Fe $L_{2,3}$-absorption edges.

The γ-Fe$_2$O$_3$ nanowires, deposited on cleaved HOPG, have been annealed at

increasing temperature steps up to 380 °C, and the spectroscopic features have
been measured after recovering room-temperature (RT) for each temperature
step: the Fe-2p spectral evolution as a function of temperature is shown in Fig.
4.1 (left panel). At RT, the spectrum presents the characteristic feature of the
Fe_2O_3 as presented in the previous chapter: the Fe-2p spectrum presents the
Fe-2$p_{3/2}$ and Fe-2$p_{1/2}$ core-levels at 711.26 and 724.64 eV respectively, and the
associated satellites S_1 and S_2 located at $\approx$8 eV higher BE. Upon reaching 170
°C, the Fe-2$p_{3/2}$ core-level peak shifts from 711.26 eV to 710.96 eV, the satellites
(S_1 and S_2) associated to the main core-level peaks disappear, and the lineshape
of Fe-2$p_{3/2}$ and Fe-2$p_{1/2}$ structures becomes broader. By annealing to 380 °C
the Fe-2p core-levels reach a saturation lineshape and shift towards lower BE
with a total shift of 1.2 eV. At saturation new satellites appear, located at $\approx$6
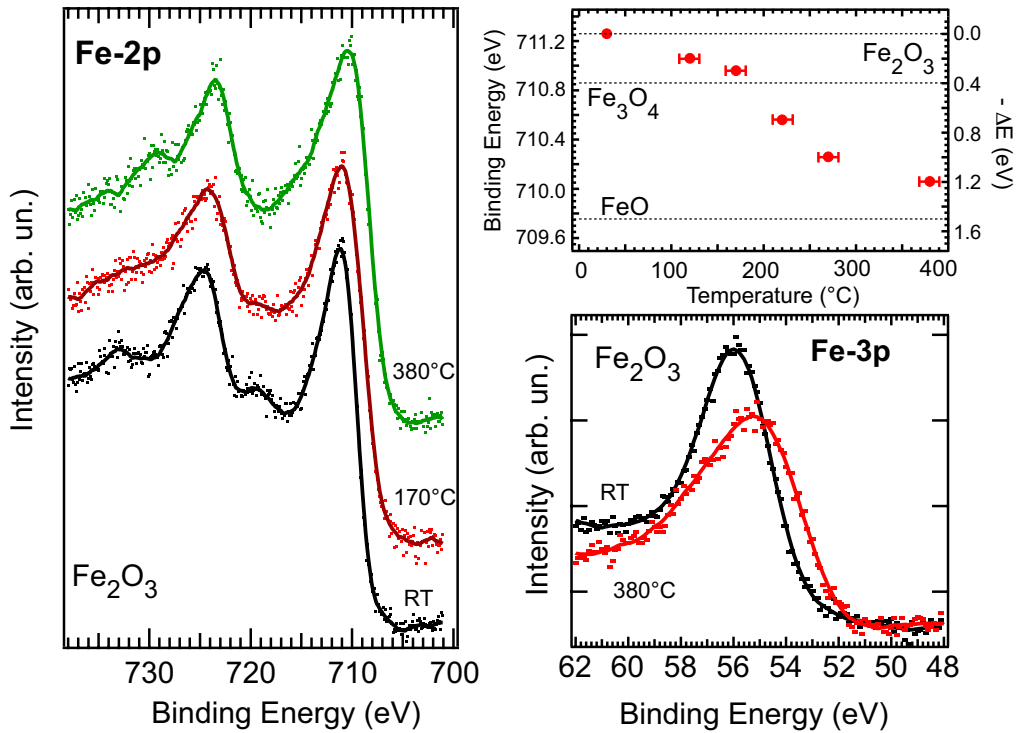eV higher binding energy with respect to the main peaks.

Figure 4.1: Fe-2p (left panel) and Fe-3p (right-bottom panel) core levels evolution at
significant temperature steps.Fe-2p energy shift as function of temperature (right-top
panel).

The Fe-3p core-level at RT presents a single broadened peak centered at
56 eV (Fig. 4.1, right bottom panel). Its lineshape is in agreement with the

presence of Fe^{3+} ion of the Fe_2O_3 compound (studied in the previous chapter). At saturation point, there is a change of the Fe-$3p$ lineshape, with a broadening of the structure towards lower binding energy, compatible with the emerging of a chemically shifted component associated to Fe^{2+} reduced ions, whose $3p$ binding-energy is expected at 54 eV.[61,65,194]

The shift of the Fe-$2p$ states and the modification of the satellites, and of Fe-$3p$ lineshape after annealing are compatible with a variation in the oxidation state of the iron ion. In the Fe_2O_3 compound, all the ions have a 3+ oxidation state. After the annealing, the lineshape of Fe-$2p$ and $3p$ core levels confirms the presence of 2+ ions. These modifications are compatible with the formation of the Fe_3O_4 compound. In particular, in the configuration achieved after annealing to only 170 $°C$, the Fe-$2p$ lineshape corresponds to the typical lineshape of the Fe_3O_4 compound.[194] We can assume that in the nanowired system there is a modification to the oxidation state of the iron ion due to a transition from Fe_2O_3 to Fe_3O_4, and a consequently loss of oxygen, at relatively low (170 $°C$) temperature.

Upon increasing temperature, the Fe^{2+} component becomes more relevant. A quantitative analysis of the Fe-$3p$ core-levels was done to estimate the percentage and the ratio between Fe^{3+} and Fe^{2+} ions at different increasing temperature steps (reported in Fig. 4.2). The Fe-$3p$ core-level at RT presents a broadened and asymmetric lineshape because of many effects, including spin-orbit interaction, multiplet splitting and multiple ionization. As reported in the previous chapter, taking into account all these phenomena the Fe-$3p$ core-level was fitted with three Voigt curves (Gaussian-Lorentzian lineshape) peaks presenting 1.0 eV Lorentzian width and 1.8 eV Gaussian width (light colored curves). At higher temperature the same three-peaks manifold is used to fit the new Fe^{2+} component at lower BE. The Fe^{2+} components become relevant at 170°C (dark colored curves) when the ratio between Fe^{3+} and Fe^{2+} is 70:30 ($\approx$2.3). The ratio and the lineshape achieved are in good agreement with the characteristic of the Fe_3O_4 compound in which the perfect ratio between Fe^{3+} and Fe^{2+} is 2:1. At higher temperature, the Fe^{2+} component increases and the system achieves a 40:60 percentage for Fe^{3+}/Fe^{2+} ratio at 380°C.

The Fe-$L_{2,3}$ NEXAFS data for the nanowires at RT and after annealing at 170 $°C$ are shown in Fig. 4.3. Important modifications in lineshape take place after annealing, namely the main absorption peaks shift by 0.1 eV to lower
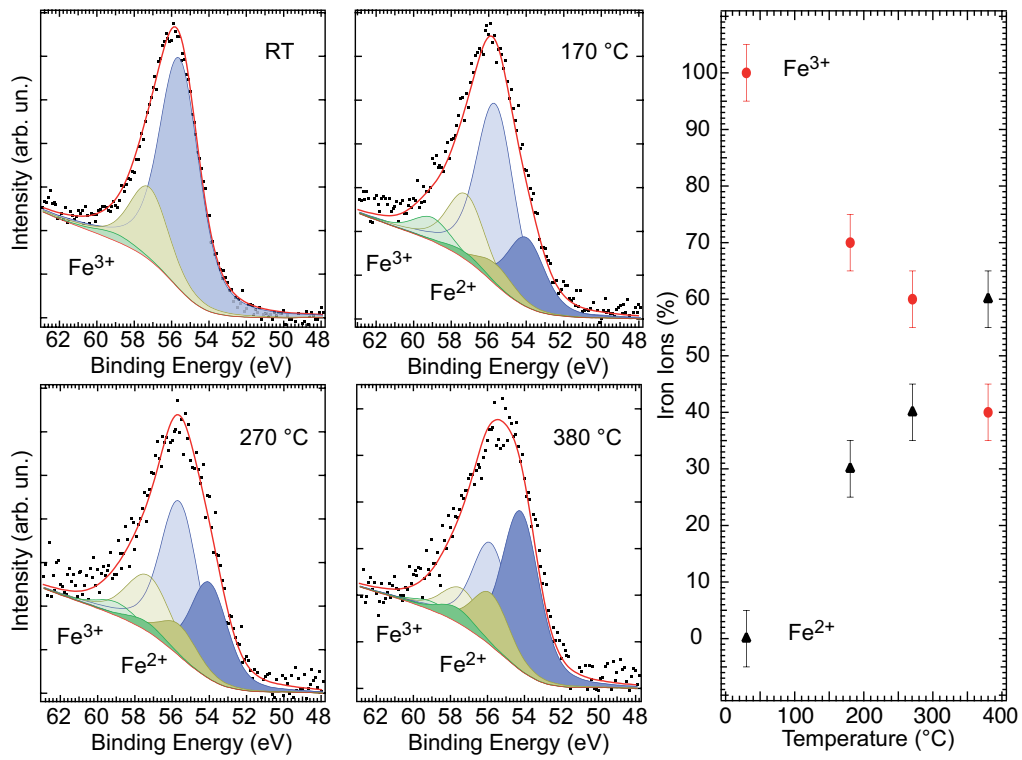
Figure 4.2: XPS data for the Fe_2O_3 nanowires as a function of annealing temperature. Fe-$3p$ XPS core-levels at different temperatures with the two manifolds for Fe^{2+} and Fe^{3+} ions (left panel), percentage of Fe^{2+} and Fe^{3+} ions (right panel).
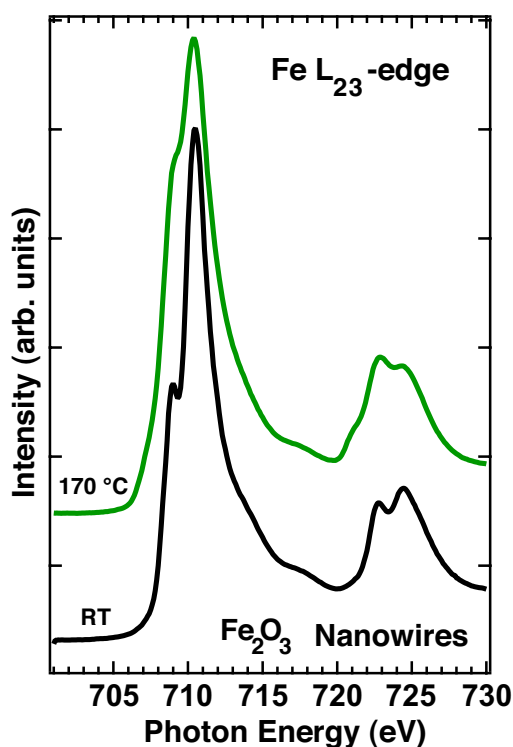
Figure 4.3: NEXAFS data for the nanowires at RT and after annealing at 170°C.

photon energy, the intensity ratio between the two main peaks at both the L_3 and L_2 edges changes, and a pre-edge shoulder appears at lower photon energy (708 eV, 3.6 eV below the main L_3 resonance). The new observed lineshape is characteristic of the Fe_3O_4 compound and confirms the transition from Fe_2O_3 to Fe_3O_4 compound of the nanowire observed with XPS technique.[194]
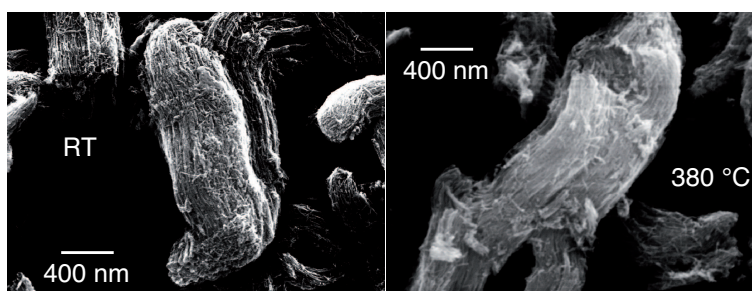
Figure 4.4: SEM images of the nanowires before and after thermal treatment.

The iron-oxide nanowires have been deposited onto a Si surface and imaged by SEM at RT before and after the thermal treatment at 380°C, to observe whether any morphology modification took place, as shown in Fig. 4.4. The

nanowires assemble in a few hundreds of nm-thick and μm-long bundles. After the thermal treatment that changes the ionic state of the Fe ion into the nanowires, they do not change either shape or morphology in the bundled structure. Thus, the thermal treatment causes a chemical reduction, while not affecting the assembling of the system.

4.2   Exposure to Lithium

The mechanism of the Fe_2O_3 electrochemical lithiation process has not yet been entirely clarified. The study of the nanowires exposed to different amounts of lithium in UHV such as to mimic the electrochemical process in a lithium battery is a first step to understand the reduction process and the correlation with the nanometric size of the system.

The reduction process under exposure to lithium vapors has been studied analyzing the Fe-$2p$, Fe-$3p$ and O-$1s$ core-levels of the γ-Fe_2O_3 nanowires deposited on the Cu substrate. The Fe_2O_3 nanowires were exposed to lithium vapor and the Fe-$2p$ spectral evolution at significant steps is reported in Fig. 4.5 (left panel).

The Fe-$2p$ spectrum for the clean system presents the characteristic features of the Fe_2O_3 compound as shown before. Upon increasing lithium exposure, the Fe-$2p$ core-levels shift towards lower binding energy (Fig. 4.5 right top panel). In particular, for the first exposure step the two main Fe-$2p$ peaks shift by $\approx$0.4 eV and the satellites are visibly quenched (red spectrum in Fig. 4.5 left panel), both effects signature of a transition of the system to a Fe_3O_4 compound.

At higher Li exposure the Fe-$2p_{3/2}$ main peak is found at 710.3 eV and at the maximum exposure (saturation point, Θ_{sat}) presents a total shift of 1.3 eV with a binding energy of 709.9 eV. At this step, new satellite features are well visible at $\approx$6 eV higher binding energy respect to the main peaks. The shift of the Fe-$2p$ main peaks and the presence of the new satellites are characteristic spectral features of the FeO compound.

The XPS Fe-$3p$ core-level spectrum for the γ-Fe_2O_3 nanowires presents a single broadened peak centered at 56 eV (Fig. 4.5, lower right panel). Its lineshape is in agreement with the presence of Fe^{3+} ion of the Fe_2O_3 compound. At increasing Li exposure, the Fe-$3p$ lineshape evolves, with a progressive broadening of the structure and an energy shift towards lower binding energy, compatible with the emerging of a chemically shifted component associated to the Fe^{2+} ions.

Figure 4.5: Fe-$2p$ (left panel) and Fe-$3p$ (right-bottom panel) core-levels evolution at significant exposure steps. Fe-$2p$ energy shift as function of Lithium exposure (right-top panel).

In fact, the Fe-3p binding-energy is expected at about 54 eV for the Fe^{2+} reduced ions,[65,194] and the lineshape observed after saturation with Li can be explained with the presence of a dominant Fe^{2+} signal, superimposed to a minor Fe^{3+} component. We notice that the Li-1s core-level is expected at 55.7 eV BE, superimposed to the Fe-3p peak. However, due to the very low photo-excitation cross-section of the Li-1s with respect to the Fe-3p core-levels,[200] its presence is absolutely undetectable.
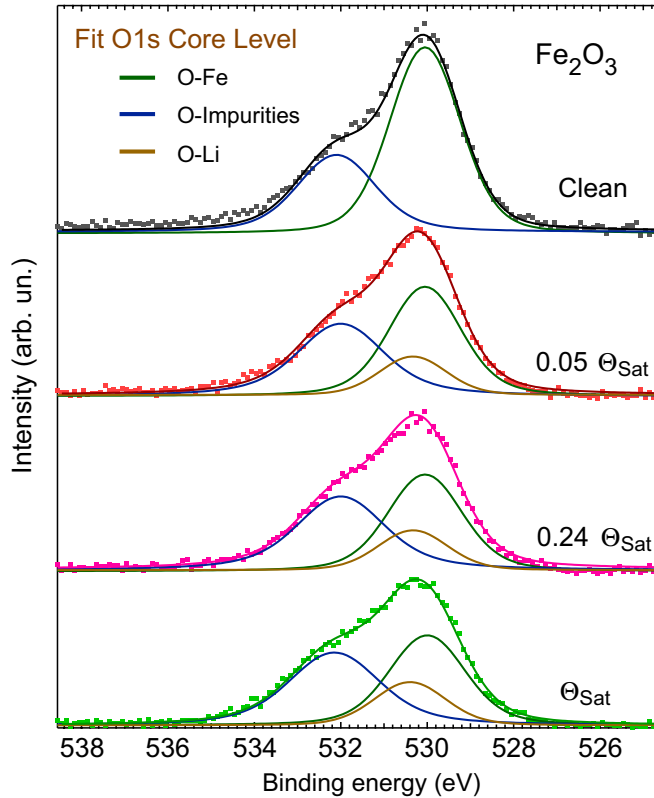
Figure 4.6: XPS data of the O 1s core-level taken on the Fe_2O_3 nanowires as a function of Li exposure; XPS data (dots) and fitting peaks (continuous lines). Data vertically stacked for clarity.

The O-1s core-level data measured on the clean Fe_2O_3 nanowires and as a function of exposure to Li, up to saturation coverage, are plotted in Fig. 4.6, along with a fitting analysis performed using gaussian functions. On the clean nanowires, we can observe the major component associated to O bound to the Fe ions at 530.1 eV BE, in very good agreement with the literature,[65] and a minor component due to oxygen contamination at 532.1 eV BE. Upon

exposure to Li, the lineshape of the O-1s core-level presents an intensity ad width variations of the peak related to the O-Fe bond. Considering the the reduction process of the Fe ions, an important new component can be attribute to Li$_x$O compounds; fitting the spectrum with three gaussian functions, considering the conservation of the total amount of oxygen atoms, the new component appears centered at 530.4 eV BE, whose signal reaches its saturation value while the other components are reduced in intensity. The Li-O peak takes into account a manifold of structures associated to the different Li$_x$O species.[201,202] These data confirm the reduction of the nanowires as a function of exposure to Li, as determined by the analysis of the Fe-2p and 3p core-levels.

The above described phases upon lithiation are due to the reduction of Fe$_2$O$_3$ towards FeO, *albeit* a complete reduction to metallic Fe, even at Li saturation coverage, is not observed. Taking into consideration the electron mean free path and the escape depth in the photoemission process for these energies,[142] we can conclude that the nanowires undergo transition towards a Fe^{2+} phase at least within a depth of 2-3 nm, thus involving a consistent portion of the bulk of each nanowire. Furthermore, it is worth noting that the direct Li exposure in UHV induces an oxidation process that cannot be strictly compared with the electrochemical Li intercalation, anyway this system can be considered as a model in order to analyze the first phases of chemical interaction and reduction.
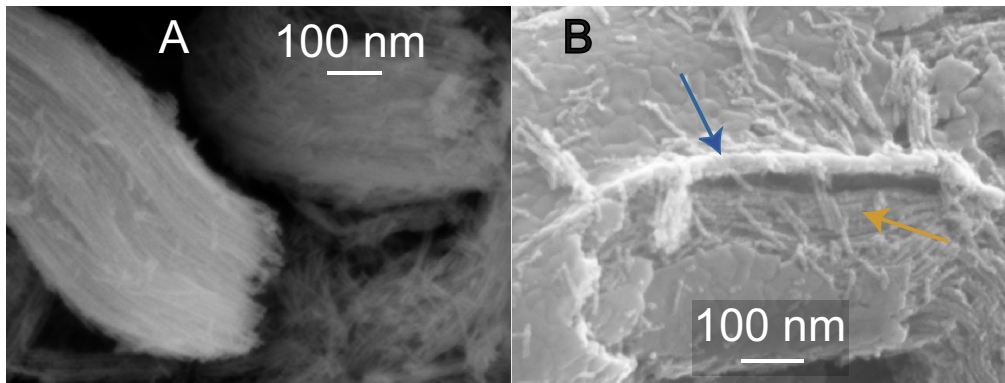
Figure 4.7: SEM images of the nanowires before (left panel) and after lithiation process (right panel).

The iron-oxide nanowires have been deposited onto a Si surface and imaged by SEM at RT before and after the lithiation process, to observe whether any morphology modification took place, as shown in Fig. 4.7 (A and B panel re-

spectively). The nanowires assemble in a few hundreds of nm-thick and μm-long bundles. From the morphological point of view the formation of Li_xO compounds are detectable looking at the presence of a new narrow structures (blu arrow) in the external part of the bundles.

4.2.1   Nanowires on Graphite substrate

The nanowires were deposited also onto a graphite (HOPG) substrate in order to simulate a new kind of electrode for lithium batteries. The final goal of this experiment is to clarify the role of the substrate in the reduction process and lithium storage upon lithium exposure.
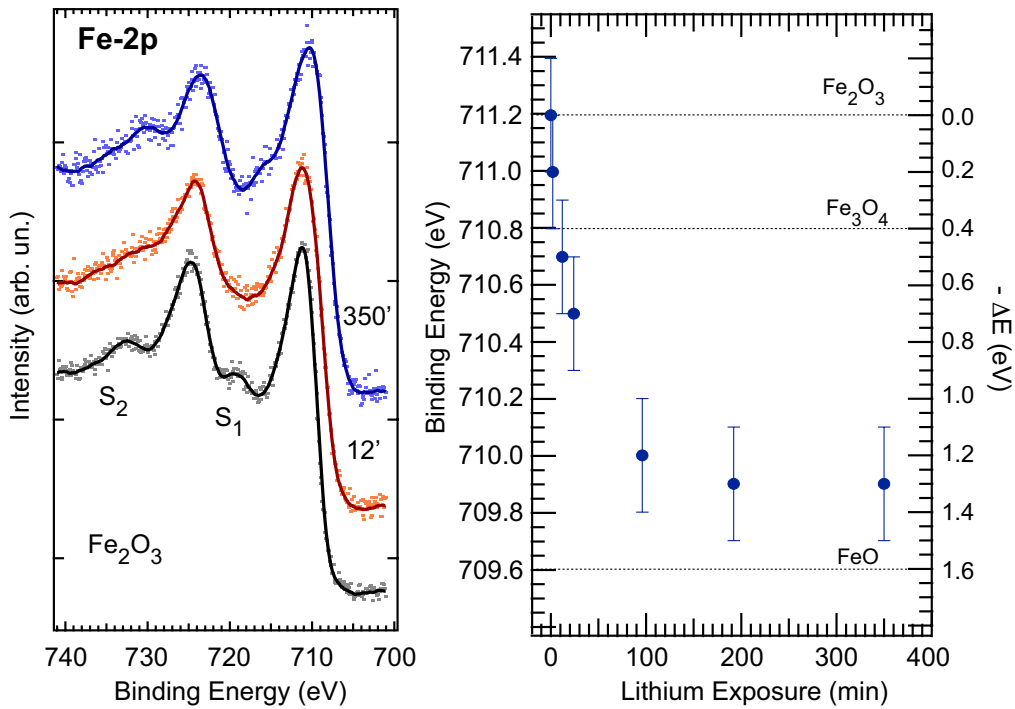
Figure 4.8: Fe-$2p$ (left panel) core-levels evolution at significant lithium exposure steps. Fe-$2p_{3/2}$ energy shift as function of lithium exposure (right panel).

The XPS Fe-$2p$ core-level spectra for the nanowires, deposited on HOPG, upon lithium exposure are presented in Fig. 4.8 at significant exposure steps. The spectral evolution of Fe core-levels follows the same trend of that observed for the nanowires deposited on Cu. The Fe-$2p$ core-levels for the clean sample present the characteristic lineshape of Fe_2O_3 compound with the Fe-$2p_{3/2}$ and Fe-$2p_{1/2}$ core-levels separated by spin-orbit interaction, at 711.2 and 724.6 eV respectively, and the associated satellites S_1 and S_2 located at ≈ 8 eV higher

binding energy. At low exposure the Fe-$2p_{3/2}$ presents a 0.2 eV shift and the satellites are not visible, at this step the nanowires achieve the Fe_3O_4 configuration. At higher exposure steps the shift increases up to 1.3 eV and the lineshape shows the characteristic features of the FeO compound, in agreement with the results obtained on Cu substrate. This steps is considered the saturation point for the nanowires because at higher exposure the lineshape does not present any change or shift.
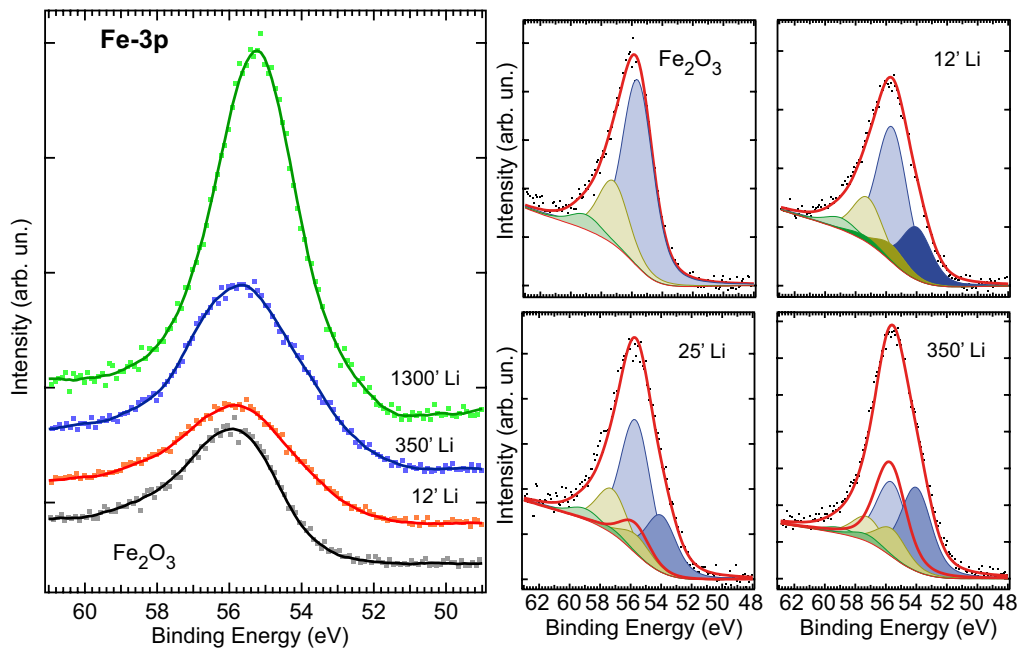
Figure 4.9: XPS of the Fe-3p and Li-1s core levels as a function of Li deposition time. Left panel: XPS data, stacked along the vertical axes for clarity (rough data, dots; smoothed data, continuous lines). Right panel: four panels with the data on the clean NWs/HOPG and at four selected steps of Li exposure; experimental data (black dotted curves) and total fitting curves (red continuous lines), along with the deconvolution with contributions associated to the Fe^{3+} (light shadowed curves), Fe^{2+} (darker shadowed curves) oxidation states, and to the Li-$1s$ peak (red curve).

The spectra of the nanowires deposited on HOPG substrate, in the energy range of Fe-$3p$ core-levels, present a different and interesting behavior with respect to the spectra of the nanowires deposited on Cu. The spectrum of the nanowires before lithium exposure (Fig. 4.9) presents the characteristic features presented in the previous chapter with a broadened peak centered at 56 eV (bottom spectrum) related to the Fe^{3+} configuration in the system. Upon

lithium deposition, the Fe-3p core-levels follows the same trend observed for the nanowires on Cu; the new component of Fe^{2+} emerges at lower BE (red spectrum in Fig. 4.9 left panel), in agreement with that expected at 54 eV for Fe^{2+} reduced ions[61,65]. Differently from the results obtained on Cu, for the nanowires on HOPG at higher lithium exposure we observe a huge increase of spectrum intensity in energy range between 50 and 60 eV; this behavior cannot be attributed to a Fe reduction but can be explained considering the formation of Li_xO compounds that present the Li-1s core-level at 55.7 eV BE, superimposed to the Fe-3p peaks.

In order to evaluate the Fe^{3+} and Fe^{2+} components, the spectra were fitted with three Voigt functions for each species (light and darker curves respectively) as performed in the previous section, all presenting the same Gaussian width (GW=1.8 eV) and Lorentzian width (LW= 1.0 eV); at high deposition steps an additional Voigt curve was introduced in order to estimate the Li-1s component due to the Li_xO in the spectra. The fitting procedure has been carried out at each Li coverage step, leaving the relative intensity of each manifold and the energy as free parameters. The experimental data along with the resulting fitting curves, and the single components de-convoluted of Fe-3p and Li-1s core levels as a function of lithium exposure are reported in Fig. 4.9, for significant selected steps of Li deposition. At the first two steps the Li_xO component is not visible because the very low photon-excitation cross-section of the Li-1s (0.7912 kBarn) with respect to the Fe-3p (22.35 kBarn), at higher deposition time the Li-1s becomes more relevant and detectable. The Li-1s peak is found at 55.7 eV BE and is fitted with a LW=1.0 eV and the same GW=1.8 eV of the other structures, the GW being basically associated to the experimental resolution. A slight binding energy shift of the of Li-1s peak takes place at the maximum exposure, associated to the Li oxidation, as expected.

The intensity ratio between the Fe^{3+} and Fe^{2+} content and of the Li up-take in the nanowires on HOPG as a function of Li deposition time, as estimated from the fitting components, are shown in Fig. 4.10. At low lithium exposure the ratio between Fe^{2+} and Fe^{3+} is 70:30 ($\approx$2,3) in agreement with the formation of the Fe$_3$O$_4$ compound as observed in Fe-2p core levels; increasing the exposure the percentage of Fe^{2+} becomes higher and achieves a final configuration with a ratio of 35:65 between Fe^{2+} and Fe^{3+}. The results obtained are in agreement with the progressive release of oxygen and reduction of iron ions from Fe$_2$O$_3$ to
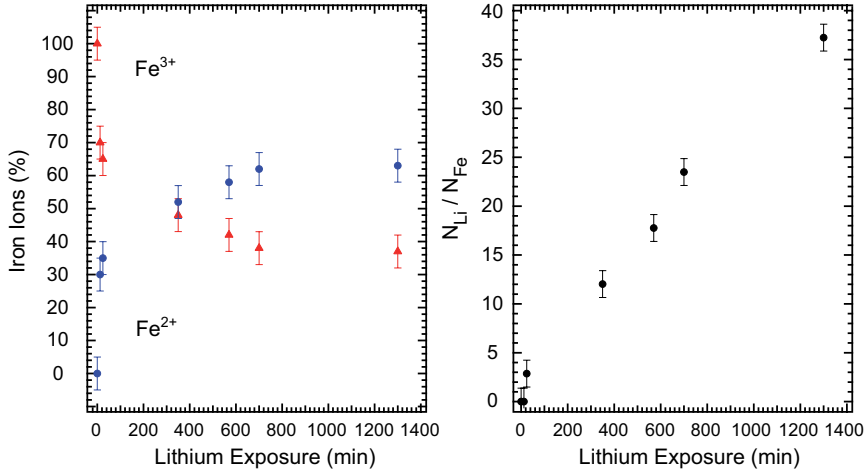
Figure 4.10: Evaluation of content of Fe^{3+} and Fe^{2+} oxidation state (left panel) and of the Li up-take (right panel) in the iron-oxide NWs deposited onto HOPG, as a function of deposition time. Intensity estimations as obtained from the fitting of the XPS experimental data (see text): Fe^{3+} (red triangles, left) and Fe^{2+} (blue dots, left) content of Fe ions; Li content *per* Fe atoms (black dots, right).

Fe_3O_4 and FeO. While the iron ions are reduced, the Li content increases, as shown in the right panel of Fig. 4.10, where the number of Li atoms *per* Fe atoms estimated from the fitting procedure, as a function of Li exposure, is drawn.

The Li/Fe intensity ratio is reported after a normalization factor taking into account the excitation cross-sections for the Li-1s and Fe-3p core levels, 0.7912 kBarn and 22.35 kBarn, respectively[200]. At Li saturation coverage, for the nanowires deposited on HOPG we observe more than 35 Li ions *per* Fe ion. Stoichiometrically, in the Lithiation process of Fe_2O_3, six Li atoms should be involved to obtain the complete reduction of the Fe ions ($6Li + Fe_2O_3 \rightarrow 2Fe + 3Li_2O$[29,203]). Actually, a prevalence of divalent Fe ions at saturation of the Fe-related signal is observed, with both the 2p and 3p spectral signals characteristic of a prevalent divalent Fe configuration but not a complete reduction to neutral iron.

Comparing the obtained results for nanowires deposited on Cu and on HOPG substrates we can observe that, exposing the two systems at the same amount of Li, the Li content in the second system is much higher than expected and than observed in the first one. These results clearly suggest that graphite strongly favors the alkali metal intercalation, thus allocating a huge amount of Li atoms into the HOPG planes, without affecting the ionic state of Fe.

4.3   Bulk-like microparticles

The reduction process in the γ-Fe_2O_3 nanowires due to the thermal treatment or lithium exposure can be compared with the behavior of α-Fe_2O_3 bulk-like microparticles under the same conditions in order to clarify if the different size and shape of the nanowires could induce the reduction with different kinetics from bulk-like systems.
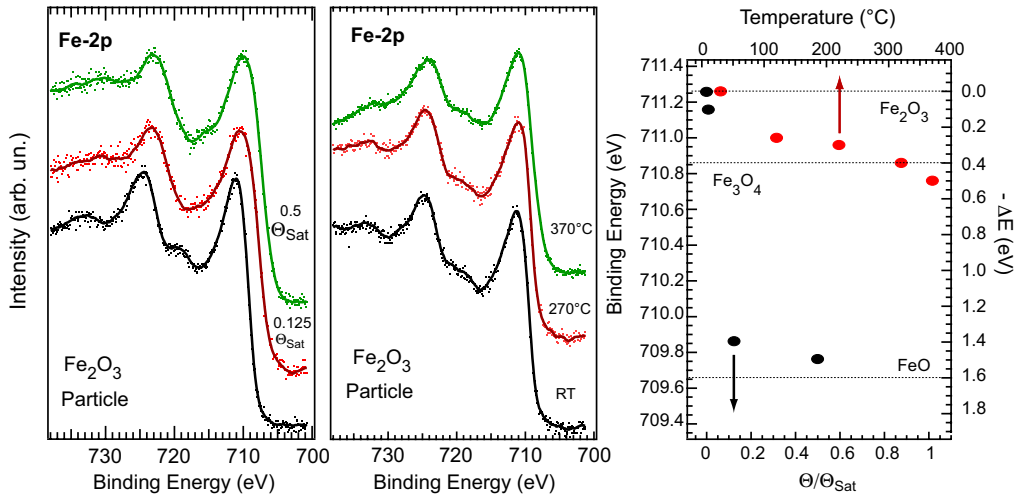
Figure 4.11: Fe-$2p$ core-levels evolution in bulk-like microparticles at significant lithium exposure (left panel) and temperature steps (central panel).Fe-$2p$ energy shift as function of lithium and temperature (right panel).

The XPS data for the bulk-like microparticles upon the lithiation process and thermal treatment are shown in Fig. 4.11. The spectra of the clean samples (black bottom spectra) present the characteristic feature of Fe_2O_3 compound as analyzed in the previous paragraphs.

The spectral evolution at significant temperatures is reported in Fig. 4.11 (central panel) with the evaluation of the Fe-$2p_{3/2}$ energy shift during thermal treatment (red point in right panel). Heating the microparticles a maximum energy shift of 0.5 eV is achieved. The shift is in agreement with the formation of Fe_3O_4 compound. Otherwise, the Fe-$2p$ core-levels lineshape presents the characteristic satellites of Fe_2O_3 compound up to 270°C while between 270 °C and 370 °C, the quenched satellite features and the observed 0.5 eV shift suggest the co-existence of a mixed $Fe^{2+/3+}$ phase and a typical lineshape of Fe_3O_4, compatible with the expected Fe ion reduction of a bulk material.[199]. We can conclude that

the nanometric size of nanowires induced the transition from Fe_2O_3 to Fe_3O_4 at lower temperature (170°C) respect to the bulk-like microparticles (300°C).

The lineshape evolution of the Fe-$2p$ core-levels of the micro-grains as a function of Li exposure (Fig. 4.11 left panel) reflects what observed in the case of the nanowires. However the Li saturation coverage (Θ_{sat}) still corresponds to the saturation of the Fe core-levels lineshape under Li exposure, though the exposure time, thus the consequent Li content, must be normalized to the density of Fe_2O_3 ions on the surface. For the microparticles, the saturation signal is achieved with much lower Li exposure, a factor 2.2 in the same deposition conditions, with respect to the nanowires.

This result shows that the microparticles can absorb less Li atoms than the nanowires because to the lower surface area available for electron exchange. This brings to light the higher capacity of Li adsorption for the nanowires than for the bulk-like microparticles.

4.4 Final Considerations

The results obtained for γ-Fe_2O_3 nanowires under thermal treatment and lithiation exposure emphasize the role and the importance of the nanometric size of this new system. The reduction processes are correlated to the size of the system. In particular, an interesting reduction process, from Fe_2O_3 to Fe_3O_4, was observed analyzing the heated nanowires at *moderate temperature* (under 200 °C) in contrast with the expected behavior of the α-Fe_2O_3 bulk-like microparticles system where the transition temperature is in agreement with that expected for 3D materials (over 300°C). The analysis of the reduction process of the nanowires upon lithium vapor exposure in UHV emphasizes how the lithium vapors, deposited on the system, react with the first layers of the nanowires and can intercalate in the internal part of the bundles' structures. This points out how the different amount of lithium storage achieved between the nanowires and the microparticles can be attributed to the nanometric size and shape of the nanowires. Furthermore the results obtained with HOPG underline the fundamental role of the substrate and in particular of the carbon-based supports that favor the alkali metal intercalation between the HOPG planes. This suggests that an accurate analysis of behavior of carbon-based substrates (Graphite *vs* Graphene) is necessary.

Chapter 5

Carbon-based Substrate

The substrate plays a crucial role in the lithium storage process. In the previous chapter it is shown how the HOPG substrate can store more lithium than a Cu foil due to the interaction of lithium ions with carbon atoms and the intercalation between graphite planes. The maximum storage for graphite is limited by surface and density of edges that could promote the intercalation and interaction of lithium ions. An alternative to HOPG substrate can be a carbon substrate with separated single carbon planes, *i.e.* graphene, that can accommodate more lithium ions. In this chapter, an analysis and a comparison of the intercalation of lithium ions in Graphite and Graphene substrates is presented.

5.1 Graphite Substrate

The intercalation of lithium ions in graphite was studied from the theoretical and experimental point of view[118,204–213]. The results show different configuration of Li atoms and different Li-C final compound; at different amount of lithium the possible configurations achieved are LiC_2, LiC_3, LiC_6, LiC_{27}. The higher density configuration is LiC_2 where one lithium atom is disposed at the center of the hexagonal structure of graphite cell.

Differently from the experiment of Mordkovich[208], in order to simulate the behavior as anode in lithium batteries, the HOPG graphite was exposed to lithium vapor in UHV; in this condition the system achieves the maximum possible configuration without any external forces. A selection of C-1s and Li-1s core-levels at significant lithium exposure steps is presented in Fig. 5.1 (left and right panel respectively). The C-1s core-level for the clean HOPG presents a single peak centered at 284.2 eV BE characteristic for the carbon atoms in graphite

compounds. Upon exposure to Li in UHV, the C-1s XPS signal associated to
graphite is influenced and a chemical shift towards higher BE is observed. The
C-1s core-level reaches a value of 284.5 eV BE at maximum exposure, accom-
panied by an intensity reduction. At the same saturation point the Li-1s XPS
signal presents a well defined peak at 55.7 eV BE associated with intercalated
lithium.
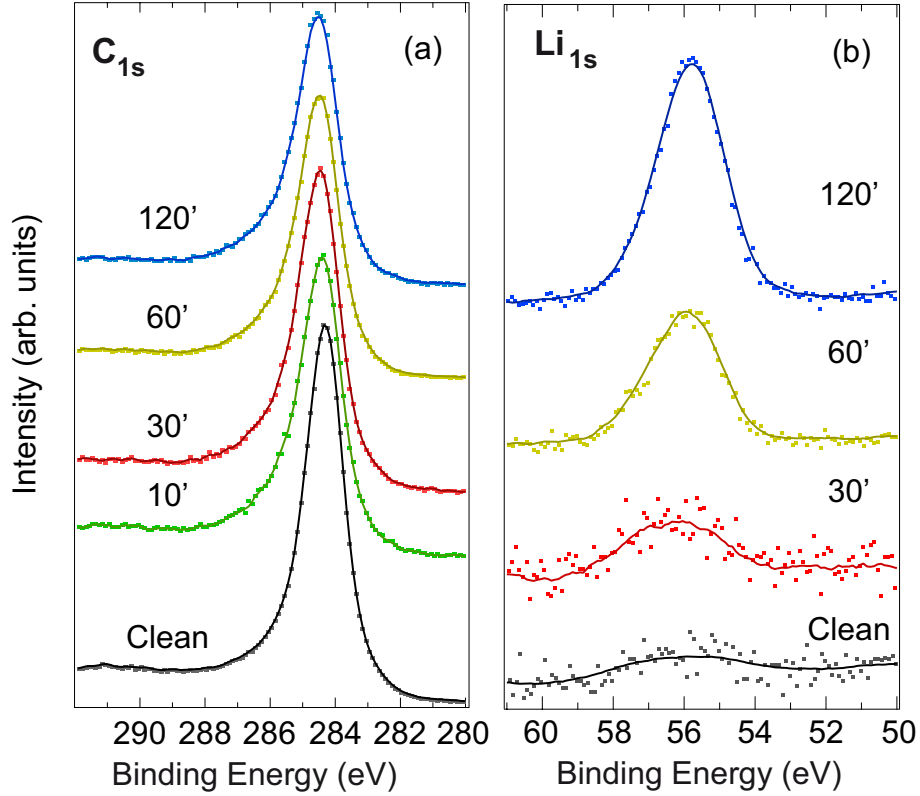
Figure 5.1: XPS evolution of C-1s (left panel) and Li-1s core-level lineshapes upon
Li deposition in HOPG system.

This spectroscopic behavior is consistent with the intercalation of the in-
teracting Li ions among the graphite planes. In particular, by taking into ac-
count the photo-excitation cross-section of the Li-1s and the C-1s photoemission
peaks[200], we can estimate a stoichiometry corresponding to $\approx LiC_6$, i.e., about
one Li ion *per* six C atoms of the graphite substrate. This result is in agreement
with the electrochemical results and corresponds with a theoretical capacity of
370 $mAhg^{-1}$.

5.2 Graphene Substrate

In a perfect graphite anode the storage of lithium ions occurs on the first layer of graphite; defects, edges and flakes contribute to increase the lithium storage. Anyway the crystal structure of graphite limits the amount of lithium that can be stored as observed in the previous section. In order to increase the amount of stored lithium (*i.e.* the capacity if lithium batteries) a pristine graphene substrate is proposed. The standard graphite anode can intercalate a maximum of one lithium ion *per* six C atoms, giving a stoichiometry of LiC_6, to which corresponds a theoretical capacity of 370 $mAhg^{-1}$, the graphene can in principle accommodate lithium on both sides, LiC_3, this doubling the specific capacity up to 740 $mAhg^{-1}$.[214]

In this section the morphologic and spectroscopic characterization of a graphene based anode and a study of the intercalation process of lithium ions, in comparison with that obtained for HOPG, are reported.

5.2.1 Graphene Characterization
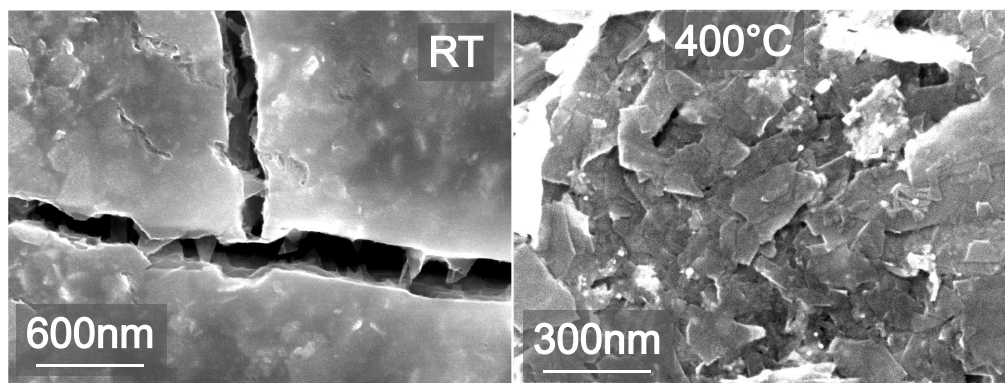
Figure 5.2: SEM images of graphene system at room temperature (RT, left panel) and after thermal treatment (400°C, right panel).

The pristine graphene was produced by exfoliating graphite by chemical wet dispersion and in order to obtain graphitic flakes with small lateral size, after the exfoliation process, the as-prepared dispersion is purified via ultracentrifugation, exploiting the sedimentation-based separation (as described in Chap. **??**). The graphene ink produced after ultracentrifugation was deposited on Cu substrate (see Chap. 2. The SEM image taken on the pristine system at RT left panel in Fig. 5.2, evidences the graphene flakes in a region with evident defects.

The flakes present a size of the order of hundreds of nm but show a smeared appearance, probably associated with the solvent used for depositing graphene. In order to clean the graphene flakes from any contamination, the sample was annealed at 400 °C under UHV. The SEM image of the thermal treated sample (Fig. 5.2 right panel) shows that the graphene flakes present much sharper edges while maintaining their hundreds of nm size, suggesting that thermal treatment is indeed beneficial for improving the morphology of the graphene flakes by cleaning them of solvent-related impurities.
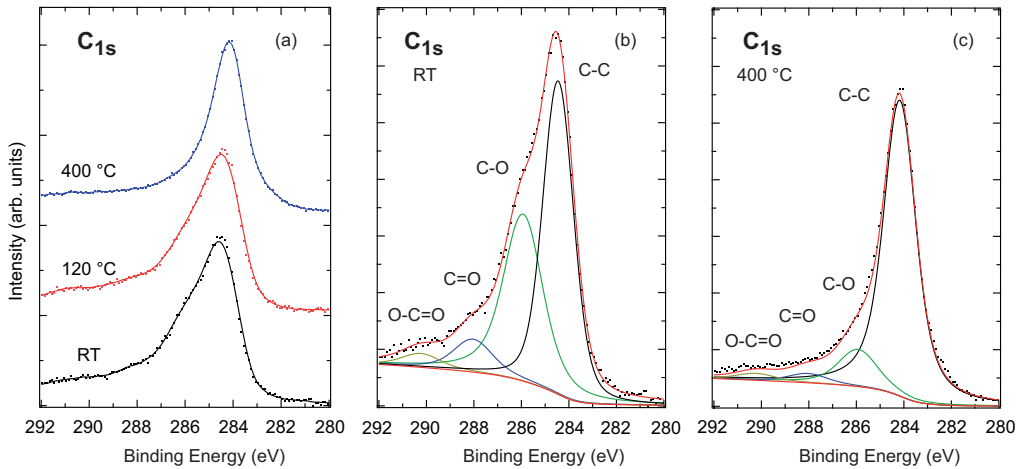
Figure 5.3: XPS evolution of C-1s at significant thermal steps (A). Fit result (red line) of C-1s core-level data of graphene at room temperature (B) and after 400°C (C). The fit was performed with four different Voigt peaks after the subtraction of Shirley background: C-C (black line), C-O (green line), C=O (blue line) and O-C=O (dark yellow line).

In order to determine the chemical quality of the graphene flakes, an XPS analysis was done on both samples (as-deposited and annealed one), focusing on the C-1s core-level. The C-1s core-level taken from pristine-graphene as-deposited on Cu and after subsequent steps of increasing annealing temperatures, is reported in Fig. 5.3 (left panel). The C-1s lineshape of the as-deposited graphene flakes at RT shows the main peak associated to the planar covalent C-C bond at 284.5 eV BE, with less intense shoulders at about 286 eV, 288 eV and 290 eV BE, respectively. While the BE of the main peak is clearly related to the C-1s signal of graphene, the main shoulder corresponds to C-O bonds, and the higher BE weaker bumps may be associated to C=O and O-C=O bonds.[215] In order to estimate the percentage of the impurities, the

experimental data was fitted with Voigt functions (lorentzian-gaussian peaks) taking into consideration the intrinsic linewidth (lorentzian contribution) and the experimental resolution (gaussian contribution). An example of the main component and of the three lower intensity peaks along with the total fitting curve, for the RT and 400 °C annealed samples, is reported in Fig. 5.3 central and right panel, respectively. The intensity of the C-to-O related structures is reduced from 50% to 13% upon annealing, while the clean graphene component shifts to 284.1 eV BE and increases from 50% to 83%, thus suggesting that the thermal treatment definitely improves the graphene flake purity.[216]

Analogous higher BE feature have been recently observed in graphene-oxide after high-temperature thermal treatment in H_2 ambient or in Ar ambient, as they are present in untreated graphite platelets associated to oxygen contamination. In our data, though, the remnant signals at RT of these typical spectral features coming from C-to-O bonds are much lower in intensity than the typical graphene-oxide signals , thus these features are attributed to impurities present in the solvent during the deposition procedures, which also cause the washed appearance of the flakes in the SEM microscopy images. Upon annealing in UHV conditions, the XPS impurity-related shoulders are progressively reduced and the intense and narrow C-C peak characteristic of graphene emerges as the dominant spectral signature at 284.1 eV, assessing its very good quality.

5.2.2 Lithium Intercalation in Graphene

The annealed graphene was exposed to lithium vapor and the evolution of C-$1s$ and Li-$1s$ core-levels lineshape is reported in Fig. 5.4. The C-$1s$ core-level (Fig. 5.4-a) presents a chemical shift towards higher BE and reduction of intensity. The C-$1s$ core-level reaches a value of 284.5 eV BE at Li saturation coverage; the saturation point is attributed to 120' of exposure when the C-$1s$ core-level presents the maximum energy shift. The XPS signal of the Li-$1s$ core-level presents a peak at 55.7 eV BE associated with the intercalated lithium, as for graphite. Differently from graphite, in the graphene system, by taking into account the photo-excitation cross-section of the Li-$1s$ and the C-$1s$ photoemission peaks, the final stoichiometry is $\approx LiC_2$, i.e., about one Li ion per two C atoms of the graphene mesh, comparable to what can be expected in super-dense lithium-graphite system on the basis of theoretical estimations. The evolution of ratio between number of Li ions (N_{Li}) and C atoms (N_C) is reported in Fig.

5.5; the growth confirms the saturation point of the system.
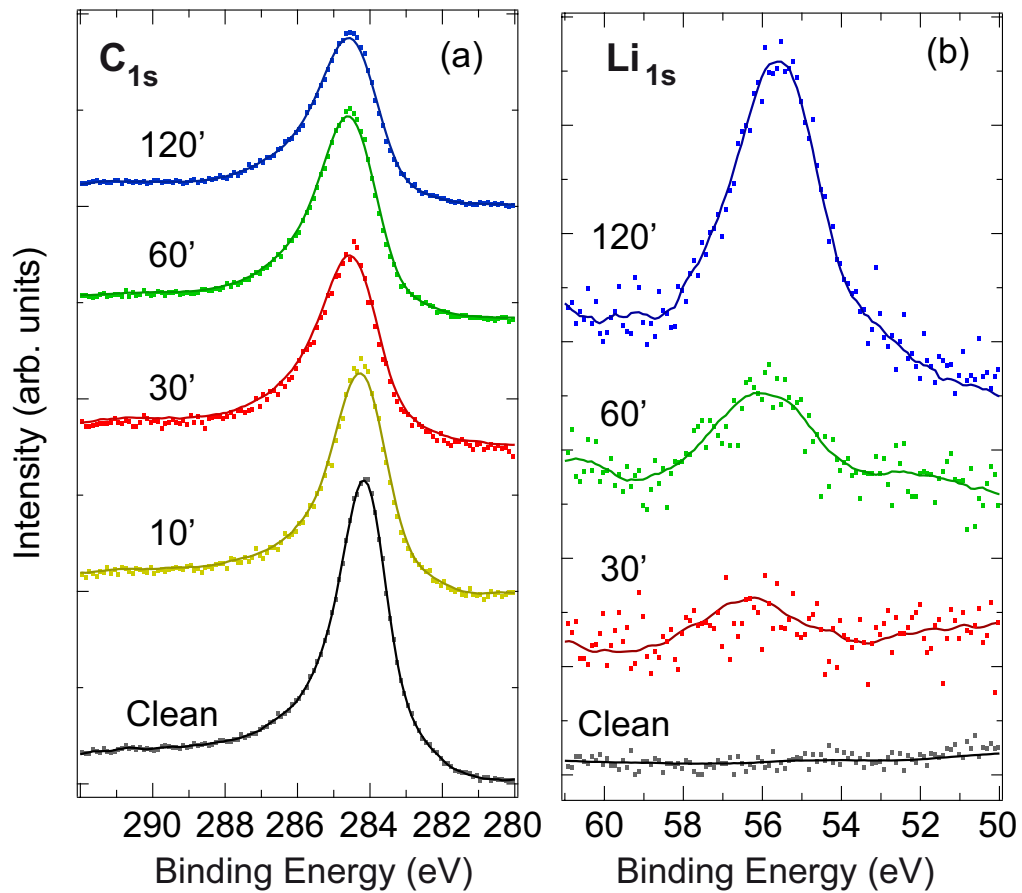
Figure 5.4: XPS evolution of C-$1s$ and Li-$1s$ core-levels under lithium exposure at significant evaporation steps.

This very high density of Li ions is fully consistent with the adsorption on the two sides of the graphene sheet, and on the enormous dispersion of carbon sheets due to the presence of independent graphene flakes, with a size of tens of nm and with high density of edges. This result is in good agreement with that observed with the electrochemical results that indicates a capacity of 740 $mAhg^{-1}$ for this system.
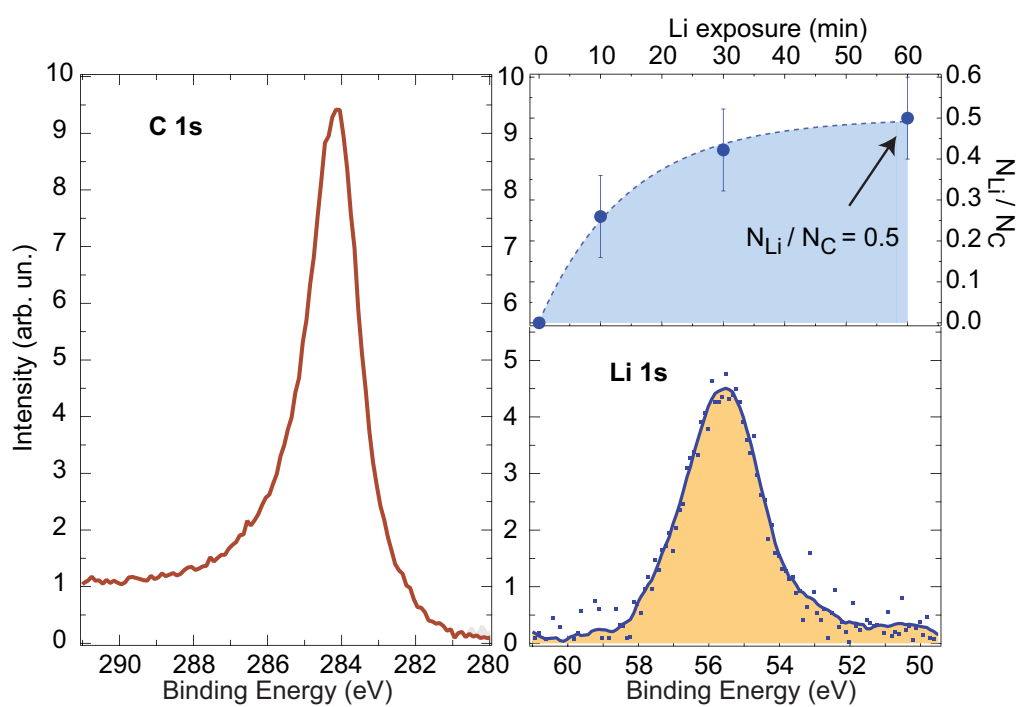
Figure 5.5: Left panel: C-$1s$ core-level of clean graphene, Right Bottom panel: Li-$1s$ core-level at maximum exposure , Right Top panel: evolution of N_{Li} vs. N_C at different exposure steps. The C-$1s$ and L-$1s$ core-levels peaks have been normalized taking into account the different excitation cross-sections.

Conclusion

The growing necessity of energy is pushing research towards the study and development of new energy storage and conversion tools with high efficiency. Particularly, Li-based rechargeable batteries, benefiting by high specific energy (high voltage joined with high specific capacity), high rate capability, high safety and low cost, offer the most promising option to support renewable energy plants. In order to increase the specific capacity and lifetime of Li-ion batteries, in the last few years, a generation of new anode material were proposed as alternative to standard graphite. In particular, the high surface/volume ratio in nanostructured systems can make even more stable and efficient batteries, optimizing capability, limited by transport of both lithium ions and electrons at the electrodes.

In this work, a new generation of nanostructured systems for Li-ion batteries anode has been studied. Among the possible alternatives Metal-Oxides, and, in particular, Iron (III) oxides Fe_2O_3 is attracting an increasing interest, for its good electrochemical properties, and low-cost and eco-sustainable characteristics. In particular, Iron-Oxide nanowires, produced following hard-template method, and Graphene nanoflakes, produced by ultrasonication of graphite, have been proposed. The systems have been completely characterized from morphological (with *Scanning Electron Microscopy* and *Atomic Force Microscopy* techniques) and spectroscopical (with *X-Ray Photoemission Spectroscopy* and *Near Edge X-Ray Absorption Fine Structure* techniques) point of view. The hard-template method guarantees to control size and shape of nanostructures and ad-hoc designed structures may lead to iron-oxides with significantly improved performances both in terms of specific capacity and of rate capability.

The microscopical analysis, performed on the Iron-Oxide nanowires, show bundle structures, that present an average width of $400 \ nm$ and with a variable

length from hundreds nanometers to several microns. This $thick-bundles$ are composed by $micro-bundles$ composed themselves by aggregated and ordered parallel nanowires. The size of the nanowires has been estimated trough a statistical analysis of the SEM images; the results show a average size of 8 nm, in excellent agreement with the expected size of the hard-template. The combined analysis of XPS and NEXAFS measurements gives informations about the oxidation state of the iron ions and about the crystal phase of the nanowires. The Fe-2p core-levels data and the NEXAFS measurement at the Fe-L$_{23}$ edges show characteristic spectra of iron (III) (Fe^{3+} ions) configuration; these results attribute a Fe$_2$O$_3$ state at the system. The absorption spectrum of Oxygen K-edge distinguish the crystal phase of the nanowires; in particular the features observed in the range between 530 and 534 eV confirm the γ-cubic phase (γ-Fe$_2$O$_3$) of the nanowires.

The role and the importance of the nanometric size of this new system have been emphasized by the results obtained for the reduction processes under thermal treatment and lithiation exposure. An interesting reduction process, from Fe$_2$O$_3$ to Fe$_3$O$_4$, was observed analyzing the heated nanowires at $moderate\ temperature$ (under 200 °C) in contrast with the expected behavior of the α-Fe$_2$O$_3$ bulk-like microparticles system where the transition temperature is in agreement with that expected for 3D materials (over 300°C). The crucial role of the nanometric size have been also highlighted studying the reduction process upon lithium vapor exposure in UHV. The lithium vapors, deposited on the system, react with the first layers of the nanowires and can intercalate in the internal part of the bundles' structures; the different amount of lithium storage achieved (2:1 ratio) between the nanowires and the microparticles can be attributed to the nanometric size and shape of the nanowires.

In order to improve the specific capacity and lifetime of the Li-ion batteries different substrates have been analyzed. The γ-Fe$_2$O$_3$ nanowires were deposited onto Cu and graphite (HOPG). The Cu substrate does not react with deposited lithium ions whereas with HOPG an increases in stored lithium ions due to the interaction with carbon atoms and the intercalation between graphite planes. This result suggests the importance of the carbon-based anode and substrates. An alternative to HOPG substrate can be graphene, that can accommodate more lithium ions due to the large amount of separated single carbon planes. Graphene nanoflake ink, prepared via low-power ultrasonication of graphite, has

been characterized with XPS technique before and after exposure to lithium vapor. The results obtained on the non-treated ink show the characteristic peak of C-C bond and additional less intense peaks due to single and double C-O bonds associated to impurities on the sample. After a annealing at 400°C in UHV condition, there is an reduction of intensity of the peaks related to the impurities and a shift in the position of the C-C peak to 284.1 eV. This features confirm the very good quality of the pristine graphene. The annealed graphene was exposed to lithium vapor in order to quantify the lithium atoms that the system can accommodate. The XPS results on the C-1s and Li-1s core-levels confirm the higher capacity of the pristine graphene ink than the HOPG with a final stoichiometry of $\approx LiC_2$ for graphene and $\approx LiC_6$ for HOPG, in good agreement with the electrochemical results.

In conclusion, with the hard-template method, Iron Oxides (γ-Fe$_2$O$_3$) ordered nanowires, with controlled size, have been obtained. The morphological and spectroscopical characterizations evidence the thermal stability and high capacity that make this system very interesting as anode material in Lithium-ion batteries. High quality graphene, obtained via ultrasonication of HOPG, presents high capacity and cycling properties that are fundamental factors to improve the lithium-ions batteries' performances. A natural prosecution of this work is to extend the studies to new Iron Oxide-Graphene structures in order to find the best configuration to combine the high capability and cycles lifetime of the two systems.

Bibliography

[1] M Armand and J-M Tarascon. Building better batteries. *Nature*, 451(7179):652–7, February 2008.

[2] Bruno Scrosati and Jürgen Garche. Lithium batteries: Status, prospects and future. *Journal of Power Sources*, 195(9):2419–2430, May 2010.

[3] Bruno Scrosati, Jusef Hassoun, and Yang-Kook Sun. Lithium-ion batteries. A look into the future. *Energy & Environmental Science*, 4(9):3287, August 2011.

[4] J M Tarascon and M Armand. Issues and challenges facing rechargeable lithium batteries. *Nature*, 414(6861):359–67, November 2001.

[5] P Poizot, S Laruelle, S Grugeon, L Dupont, and J M Tarascon. Nano-sized transition-metal oxides as negative-electrode materials for lithium-ion batteries. *Nature*, 407(6803):496–9, September 2000.

[6] Yunhai Ding, Jiaxin Li, Yi Zhao, and Lunhui Guan. Direct synthesis of iron oxide nanoparticles on an iron current collector as binder-free anode materials for lithium-ion batteries. *Materials Letters*, 81:105–107, August 2012.

[7] D. Larcher, C. Masquelier, D. Bonnin, Y. Chabre, V. Masson, J.-B. Leriche, and J.-M. Tarascon. Effect of Particle Size on Lithium Intercalation into α-Fe2O3. *Journal of The Electrochemical Society*, 150(1):A133, 2003.

[8] Jordi Cabana, Laure Monconduit, Dominique Larcher, and M Rosa Palacín. Beyond intercalation-based Li-ion batteries: the state of the art and challenges of electrode materials reacting through conversion reactions. *Advanced Energy Materials*, 22(35):E170–92, October 2010.

[9] Jingjing Zhang, Tao Huang, Zhaolin Liu, and Aishui Yu. Mesoporous Fe2O3 nanoparticles as high performance anode materials for lithium-ion batteries. *Electrochemistry Communications*, 29:17–20, April 2013.

[10] Jinping Liu, Yuanyuan Li, Hongjin Fan, Zhihong Zhu, Jian Jiang, Ruimin Ding, Yingying Hu, and Xintang Huang. Iron Oxide-Based Nanotube Arrays Derived from Sacrificial Template-Accelerated Hydrolysis: Large-Area Design and Reversible Lithium Storage. *Chemistry of Materials*, 22(1):212–217, January 2010.

[11] Y.X. Chen, L.H. He, P.J. Shang, Q.L. Tang, Z.Q. Liu, H.B. Liu, and L.P. Zhou. Micro-sized and Nano-sized Fe3O4 Particles as Anode Materials for Lithium-ion Batteries. *Journal of Materials Science & Technology*, 27(1):41–45, January 2011.

[12] Zhiyu Wang, Deyan Luan, Srinivasan Madhavi, Chang Ming Li, and Xiong Wen David Lou. α-Fe2O3 nanotubes with superior lithium storage capability. *Chemical communications (Cambridge, England)*, 47(28):8061–3, July 2011.

[13] P L Taberna, S Mitra, P Poizot, P Simon, and J-M Tarascon. High rate capabilities Fe3O4-based Cu nano-architectured electrodes for lithium-ion battery applications. *Nature materials*, 5(7):567–73, July 2006.

[14] Hao Bin Wu, Jun Song Chen, Huey Hoon Hng, and Xiong Wen David Lou. Nanostructured metal oxide-based materials as advanced anodes for lithium-ion batteries. *Nanoscale*, 4(8):2526–42, April 2012.

[15] Shu-Lei Chou, Jia-Zhao Wang, Zhi-Xin Chen, Hua-Kun Liu, and Shi-Xue Dou. Hollow hematite nanosphere/carbon nanotube composite: mass production and its high-rate lithium storage properties. *Nanotechnology*, 22(26):265401, July 2011.

[16] Zhiyu Wang, Liang Zhou, and Xiong Wen David Lou. Metal Oxide Hollow Nanostructures for Lithium-ion Batteries. *Advanced Materials*, 24(14):1903–1911, April 2012.

[17] Qiumei Zhang, Zhicong Shi, Yuanfu Deng, Jun Zheng, Guichang Liu, and

Guohua Chen. Hollow Fe3O4/C spheres as superior lithium storage materials. *Journal of Power Sources*, 197:305–309, January 2012.

[18] Bonil Koo, Hui Xiong, Michael D Slater, Vitali B Prakapenka, Mahalingam Balasubramanian, Paul Podsiadlo, Christopher S Johnson, Tijana Rajh, and Elena V Shevchenko. Hollow iron oxide nanoparticles for application in lithium ion batteries. *Nano Letters*, 12(5):2429–35, May 2012.

[19] Jongnam Park, Kwangjin An, Yosun Hwang, Je-Geun Park, Han-Jin Noh, Jae-Young Kim, Jae-Hoon Park, Nong-Moon Hwang, and Taeghwan Hyeon. Ultra-large-scale syntheses of monodisperse nanocrystals. *Nature materials*, 3(12):891–5, December 2004.

[20] Pratap M Rao and Xiaolin Zheng. Unique magnetic properties of single crystal γ-Fe2O3 nanowires synthesized by flame vapor deposition. *Nano Letters*, 11(6):2390–5, June 2011.

[21] Gajendra K Pradhan and K M Parida. Fabrication, growth mechanism, and characterization of α-Fe(2)O(3) nanorods. *ACS applied materials & interfaces*, 3(2):317–23, February 2011.

[22] Amanda L Willis, Nicholas J Turro, and Stephen O'Brien. Spectroscopic Characterization of the Surface of Iron Oxide Nanocrystals. *Chemistry of Materials*, 17(24):5970–5975, November 2005.

[23] U. P. Deshpande, T. Shripathi, D. Jain, a. V. Narlikar, S. K. Deshpande, and Y. Y. Fu. Analysis of vertical alignment and bending of crystalline α-Fe2O3 nanowires using normal and grazing incidence x-ray diffraction intensities. *Journal of Applied Physics*, 101(6):064304, 2007.

[24] B. Tian, X. Liu, H. Yang, S. Xie, C. Yu, B. Tu, and D. Zhao. General Synthesis of Ordered Crystallized Metal Oxide Nanoarrays Replicated by Microwave-Digested Mesoporous Silica. *Advanced Materials*, 15(16):1370–1374, August 2003.

[25] M. V. Reddy, T. Yu, C. H. Sow, Z. X. Shen, C. T. Lim, G. V. Subba Rao, and B. V. R. Chowdari. α-Fe2O3 Nanoflakes as an Anode Material for Li-Ion Batteries. *Advanced Functional Materials*, 17(15):2792–2799, October 2007.

[26] EunJoo Yoo, Jedeok Kim, Eiji Hosono, Hao-shen Zhou, Tetsuichi Kudo, and Itaru Honma. Large reversible Li storage of graphene nanosheet families for use in rechargeable lithium ion batteries. *Nano letters*, 8(8):2277–82, August 2008.

[27] Nitin a. Kaskhedikar and Joachim Maier. Lithium Storage in Carbon Nanostructures. *Advanced Materials*, 21(25-26):2664–2680, July 2009.

[28] Xiao Huang, Zhiyuan Zeng, Zhanxi Fan, Juqing Liu, and Hua Zhang. Graphene-based electrodes. *Advanced Materials*, 24(45):5979–6004, November 2012.

[29] Bui Thi Hang, Izumi Watanabe, Takayuki Doi, Shigeto Okada, and Jun-Ichi Yamaki. Electrochemical properties of nano-sized Fe2O3-loaded carbon as a lithium battery anode. *Journal of Power Sources*, 161(2):1281–1287, October 2006.

[30] Wei-Ming Zhang, Xing-Long Wu, Jin-Song Hu, Yu-Guo Guo, and Li-Jun Wan. Carbon Coated Fe 3 O 4 Nanospindles as a Superior Anode Material for Lithium-Ion Batteries. *Advanced Functional Materials*, 18(24):3941–3946, December 2008.

[31] Arava Leela Mohana Reddy, Manikoth M Shaijumon, Sanketh R Gowda, and Pulickel M Ajayan. Coaxial MnO2/carbon nanotube array electrodes for high-performance lithium batteries. *Nano letters*, 9(3):1002–6, March 2009.

[32] Gang Wu, Xiaoyan Tan, Guiying Li, and Changwei Hu. Effect of preparation method on the physical and catalytic property of nanocrystalline Fe2O3. *Journal of Alloys and Compounds*, 504(2):371–376, August 2010.

[33] Guangmin Zhou, Da-wei Wang, Feng Li, Lili Zhang, Na Li, Zhong-shuai Wu, Lei Wen, Gao Qing (Max) Lu, and Hui-ming Cheng. Graphene-Wrapped Fe 3 O 4 Anode Material with Improved Reversible Capacity and Cyclic Stability for Lithium Ion Batteries. *Chemistry of Materials*, 22(18):5306–5313, September 2010.

[34] Jisun Kim, Min K. Chung, Bok H. Ka, Jun H. Ku, Sangjin Park, Jiheon Ryu, and Seung M. Oh. The Role of Metallic Fe and Carbon Matrix in

Fe[sub 2]O[sub 3]/Fe/Carbon Nanocomposite for Lithium-Ion Batteries. *Journal of The Electrochemical Society*, 157(4):A412, 2010.

[35] Yuqin Zou and Yong Wang. Sn @ CNT Nanostructures Rooted in Graphene with High and Fast Li-Storage Capacities. *ACS Nano*, 5(10):8108–8114, 2011.

[36] Xiyan Li, Yongqian Lei, Xiaona Li, Shuyan Song, Cheng Wang, and Hongjie Zhang. Morphology-controlled synthesis of α-Fe2O3 nanostructures with magnetic property and excellent electrocatalytic activity for H2O2. *Solid State Sciences*, 13(12):2129–2136, December 2011.

[37] Dongyun Chen, Ge Ji, Yue Ma, Jim Yang Lee, and Jianmei Lu. Graphene-encapsulated hollow Fe3O4 nanoparticle aggregates as a high-performance anode material for lithium ion batteries. *ACS applied materials & interfaces*, 3(8):3078–83, August 2011.

[38] Qunting Qu, Shubin Yang, and Xinliang Feng. 2D sandwich-like sheets of iron oxide grown on graphene as high energy anode material for supercapacitors. *Advanced materials (Deerfield Beach, Fla.)*, 23(46):5574–80, December 2011.

[39] Chien-Te Hsieh, Jia-Yi Lin, and Chung-Yu Mo. Improved storage capacity and rate capability of Fe3O4graphene anodes for lithium-ion batteries. *Electrochimica Acta*, 58:119–124, December 2011.

[40] Si-Hwa Lee, Vadahanambi Sridhar, Jung-Hwan Jung, Kaliyappan Karthikeyan, Yun-Sung Lee, Rahul Mukherjee, Nikhil Koratkar, and Il-Kwon Oh. Graphene–nanotube–iron hierarchical nanostructure as lithium ion battery anode. *ACS nano*, 7(5):4242–51, May 2013.

[41] Sheng Guo, Gaoke Zhang, Yadan Guo, and Jimmy C. Yu. Graphene oxideFe2O3 hybrid material as highly efficient heterogeneous catalyst for degradation of organic contaminants. *Carbon*, 60:437–444, August 2013.

[42] Gang Wang, Hui Wang, Shaobo Cai, Jintao Bai, Zhaoyu Ren, and Jinbo Bai. Synthesis and evaluation of carbon-coated Fe2O3 loaded on graphene nanosheets as an anode material for high performance lithium ion batteries. *Journal of Power Sources*, 239:37–44, October 2013.

[43] Bo Jin, An-Hui Liu, Guang-Yin Liu, Zhi-Zheng Yang, Xiao-Bin Zhong, Xin-Zhou Ma, Mo Yang, and Hui-Yuan Wang. Fe3O4pyrolytic graphite oxide composite as an anode material for lithium secondary batteries. *Electrochimica Acta*, 90:426–432, February 2013.

[44] Raju Prakash, Katharina Fanselau, Shuhua Ren, Tapan Kumar Mandal, Christian Kübel, Horst Hahn, and Maximilian Fichtner. A facile synthesis of a carbon-encapsulated Fe 3 O 4 nanocomposite and its performance as anode in lithium-ion batteries. *Beilstein Journal of Nanotechnology*, 4:699–704, October 2013.

[45] Hongbin Zhao, Lanying Pan, Siyi Xing, Jun Luo, and Jiaqiang Xu. Vanadium oxidesreduced graphene oxide composite for lithium-ion batteries and supercapacitors with improved electrochemical performance. *Journal of Power Sources*, 222:21–31, January 2013.

[46] C. Kuhrs, Y. Arita, W. Weiss, W. Ranke, and R. Schlögl. Understanding heterogeneous catalysis on an atomic scale: a combined surface science and reactivity investigation for the dehydrogenation of ethylbenzene over iron oxide catalysts. *Topics in Catalysis*, 14(1-4):111–123, December 2000.

[47] M. Muhler. The nature of the iron oxide-based catalyst for dehydrogenation of ethylbenzene to styrene 2. Surface chemistry of the active phase. *Journal of Catalysis*, 138(2):413–444, December 1992.

[48] Emerson H. Lee. Iron Oxide Catalysts for Dehydrogenation of Ethylbenzene in the Presence of Steam. *Catalysis Reviews*, 8(1):285–305, January 1974.

[49] R M Cornell and U Schwertmann. *The Iron Oxides*. Second edi edition, 2003.

[50] Chenjie Xu, Keming Xu, Hongwei Gu, Rongkun Zheng, Hui Liu, Xixiang Zhang, Zhihong Guo, and Bing Xu. Dopamine as a robust anchor to immobilize functional molecules on the iron oxide shell of magnetic nanoparticles. *Journal of the American Chemical Society*, 126(32):9938–9, August 2004.

[51] Lin X. Chen, Tao Liu, Marion C. Thurnauer, Roseann Csencsits, and Tijana Rajh. Fe 2 O 3 Nanoparticle Structures Investigated by X-ray Absorption Near-Edge Structure, Surface Modifications, and Model Calculations. *The Journal of Physical Chemistry B*, 106(34):8539–8546, August 2002.

[52] Hongwei Gu, Zhimou Yang, Jinhao Gao, C K Chang, and Bing Xu. Heterodimers of nanoparticles: formation at a liquid-liquid interface and particle-specific surface modification by functional molecules. *Journal of the American Chemical Society*, 127(1):34–5, January 2005.

[53] Desheng Wang, Jibao He, Nista Rosenzweig, and Zeev Rosenzweig. Superparamagnetic Fe 2 O 3 BeadsCdSe/ZnS Quantum Dots CoreShell Nanocomposite Particles for Cell Separation. *Nano Letters*, 4(3):409–413, March 2004.

[54] Ansil Dyal, Katja Loos, Mayumi Noto, Seung W Chang, Chiara Spagnoli, Kurikka V P M Shafi, Abraham Ulman, Mary Cowman, and Richard A Gross. Activity of Candida rugosa lipase immobilized on gamma-Fe2O3 magnetic nanoparticles. *Journal of the American Chemical Society*, 125(7):1684–5, February 2003.

[55] J. Manuel Perez, Terence O'Loughin, F. Joseph Simeone, Ralph Weissleder, and Lee Josephson. DNA-Based Magnetic Nanoparticle Assembly Acts as a Magnetic Relaxation Nanoswitch Allowing Screening of DNA-Cleaving Agents. *Journal of the American Chemical Society*, 124(12):2856–2857, March 2002.

[56] Omid Veiseh, Conroy Sun, Jonathan Gunn, Nathan Kohler, Patrik Gabikian, Donghoon Lee, Narayan Bhattarai, Richard Ellenbogen, Raymond Sze, Andrew Hallahan, Jim Olson, and Miqin Zhang. Optical and MRI multifunctional nanoprobe for targeting gliomas. *Nano Letters*, 5(6):1003–8, June 2005.

[57] Nathan Kohler, Glen E Fryxell, and Miqin Zhang. A bifunctional poly(ethylene glycol) silane immobilized on metallic oxide-based nanoparticles for conjugation with cell targeting agents. *Journal of the American Chemical Society*, 126(23):7206–11, June 2004.

[58] Young-Wook Jun, Yong-Min Huh, Jin-Sil Choi, Jae-Hyun Lee, Ho-Taek Song, Sungjun Kim, Sarah Yoon, Kyung-Sup Kim, Jeon-Soo Shin, Jin-Suck Suh, and Jinwoo Cheon. Nanoscale size effect of magnetic nanocrystals and their utilization for cancer diagnosis via magnetic resonance imaging. *Journal of the American Chemical Society*, 127(16):5732–3, April 2005.

[59] J Manuel Perez, F Joseph Simeone, Yoshinaga Saeki, Lee Josephson, and Ralph Weissleder. Viral-induced self-assembly of magnetic nanoparticles allows the detection of viral particles in biological media. *Journal of the American Chemical Society*, 125(34):10192–3, August 2003.

[60] T Fujii, F M F De Groot, G A Sawatzky, F. C. Voogt, T. Hibma, and K. Okada. In situ XPS analysis of various iron oxide films grown by NO 2 -assisted molecular-beam epitaxy. *Physical Review B*, 59(4):3195–3202, 1999.

[61] N. S. McIntyre and D. G. Zetaruk. X-ray photoelectron spectroscopic studies of iron oxides. *Analytical Chemistry*, 49(11):1521–1529, September 1977.

[62] R. P. Gupta and S. K. Sen. Calculation of multiplet structure of core p-vacancy levels. II. *Physical Review B*, 12(1), 1975.

[63] J. P. Crocombette, M. Pollak, F. Jollet, N. Thromat, and M. Gautier-Soyer. X-Ray-absorption spectroscopy at the Fe L23 threshold in iron Oxides. *Physical Review B*, 52(5):3143, 1995.

[64] Paul S Bagus, H J Freund, T Minerva, G Pacchioni, and F Parmigiani. Charge transfer effects and photoemission in transition metal oxides. *Chemical Physics Letters*, 251:90, 1996.

[65] P. Mills and J. L. Sullivan. A study of the core level electrons in iron and its three oxides by means of x-ray photoelectron spectroscopy. *J.Phys. D: Appl. Phys.*, 16:723, 1983.

[66] Kiiti Siratori, Shigemasa SUGA, Masaki Taniguchi, Kazuo Soda, Shigeyuki Kimura, and Akira Yanese. Photoemission Study of Fe3O4. *Journal of the Physics Society Japan*, 55(2):690, 1986.

[67] A. Fujimori, M. Saeki, N. Kimizuka, M Taniguchi, and S. Suga. Photoemission satellites and electronic structure of Fe_{2}O_{3}. *Physical Review B*, 34(10):7318–7328, November 1986.

[68] A Fujimori, N Kimizuka, M Taniguchi, and Wustite Fe. Electronic structure of FexO. *Physical Review B*, 36(12):6691–6694, 1987.

[69] C. Colliex. Electron-energy-loss-pectroscopy near-edge fine structures in the iron-oxygen system. *Physical Review B*, 44(20), 1991.

[70] C.R Brundle, T.J Chuang, and K Wandelt. Core and valence level photoemission studies of iron oxide surfaces and the oxidation of iron. *Surface Science*, 68(null):459–468, November 1977.

[71] RJ Hill, JR Craig, and GV Gibbs. Systematics of the Spinel Structure Type. *Physics and Chemistry of Minerals*, 339, 1979.

[72] Z Zhangl, C Boxall, and G H Kelsall. Photoelectrophoresis of colloidal iron oxides 1 . Hematite (a-Fe2O3). *Colloids and Surfaces A: Physicochemical and Engineering Aspects*, 13:145–163, 1993.

[73] DM Sherman. The electronic structures of Fe3+ coordination sites in iron oxides: Applications to spectra, bonding, and magnetism. *Physics and Chemistry of Minerals*, 12:161–175, 1985.

[74] S Giovannini, F Boscherini, R Carboni, L Signorini, L Pasquini, N Mahne, A Giglia, M Pedio, and S Nannarone. Multiple Scattering Analysis of O K-Edge NEXAFS in Iron Oxides. *Physica Scripta*, T115:424, 2005.

[75] R. P. Gupta and S. K. Sen. Calculation of multiplet strucutre of core p-vacancy levels. *Physical Review B*, 10(1):71, 1974.

[76] V. L. Jacobs, J. Davis, Balazs F. Rozsnyai, and John. W. Cooper. Multiple ionization and x-ray emission accompanying the cascade decay of inner-shell vacancies in Fe. *Physical Review A*, 21(6):1917, 1980.

[77] V. L. Jacobs and Balazs F. Rozsnyai. Multiple ionization and x-ray line emission resulting from inner-shell electron ionization. *Physical Review A*, 34(1):216, 1986.

[78] J. Zaanen, A Sawatzky, and J. W. Allen. Band Gaps and Electronic Structure of Transition-Metal Compounds. *Physical Review Letters*, 55(4):418, 1985.

[79] Chun-Jiang Jia, Ling-Dong Sun Sun, Feng Luo, Xiao-Dong Han, Laura J Heyderman, Zheng-Guang Yan, Chun-Hua Yan, Kun Zheng, Ze Zhang, Mikio Takano, Naoaki Hayashi, Matthias Eltschka, Mathias Kläui, Ulrich Rüdiger, Takeshi Kasama, Lionel Cervera-Gontard, Rafal E Dunin-Borkowski, George Tzvetkov, and Jörg Raabe. Large-scale synthesis of single-crystalline iron oxide magnetic nanorings. *Journal of the American Chemical Society*, 130(50):16968–77, December 2008.

[80] Suyuan Zeng, Kaibin Tang, and Tanwei Li. Controlled synthesis of alpha-Fe2O3 nanorods and its size-dependent optical absorption, electrochemical, and magnetic properties. *Journal of colloid and interface science*, 312(2):513–21, August 2007.

[81] Hirokazu Miyoshi and Hiroshi Yoneyama. Photochemical properties of iron oxide incorporated in clay interlayers. *Journal of the Chemical Society, Faraday Transactions 1: Physical Chemistry in Condensed Phases*, 85(7):1873, January 1989.

[82] F. Bentivegna, M. Nyvlt, J. Ferre, J. P. Jamet, A. Brun, S. Visnovsky, and R. Urban. Magnetically textured γ-Fe[sub 2]O[sub 3] nanoparticles in a silica gel matrix: Optical and magneto-optical properties. *Journal of Applied Physics*, 85(4):2270, February 1999.

[83] Claudius Kormann, Detlef W. Bahnemann, and Michael R. Hoffmann. Preparation and characterization of quantum-size titanium dioxide. *The Journal of Physical Chemistry*, 92(18):5196–5201, September 1988.

[84] A.D. Yoffe. Low-dimensional systems: quantum size effects and electronic properties of semiconductor microcrystallites (zero-dimensional systems) and some quasi-two-dimensional systems. *Advances in Physics*, 42(2):173–262, April 1993.

[85] Takayuki Abe, Yukio Tachibana, Takeshi Uematsu, and Masakazu Iwamoto. Preparation and characterization of Fe2O3 nanoparticles in

mesoporous silicate. *Journal of the Chemical Society, Chemical Communications*, (16):1617, January 1995.

[86] Jusef Hassoun, Stefania Panero, Priscilla Reale, and Bruno Scrosati. A New, Safe, High-Rate and High-Energy Polymer Lithium-Ion Battery. *Advanced Materials*, 21(47):4807–4810, December 2009.

[87] Martin Winter and È O Besenhard. Electrochemical lithiation of tin and tin-based intermetallics and composites. *Electrochimica Acta*, 45:31—-50, 1999.

[88] J. Hassoun, A. Fernicola, M.a. Navarra, S. Panero, and B. Scrosati. An advanced lithium-ion battery based on a nanostructured SnC anode and an electrochemically stable LiTFSi-Py24TFSI ionic liquid electrolyte. *Journal of Power Sources*, 195(2):574–579, January 2010.

[89] Jusef Hassoun, Gaelle Derrien, Stefania Panero, and Bruno Scrosati. A Nanostructured Sn-C Composite Lithium Battery Electrode with Unique Stability and High Electrochemical Performance. *Advanced Materials*, 20(16):3169–3175, August 2008.

[90] J Hassoun, G Derrien, S Panero, and B Scrosati. The role of the morphology in the response of SbC nanocomposite electrodes in lithium cells. *Journal of Power Sources*, 183(1):339–343, August 2008.

[91] Naichao Li, Charles R. Martin, and Bruno Scrosati. Nanomaterial-based Li-ion battery electrodes. *Journal of Power Sources*, 97-98:240–243, July 2001.

[92] J. Hassoun, S. Panero, and B. Scrosati. Metal Alloy Electrode Configurations For Advanced Lithium-Ion Batteries. *Fuel Cells*, 9(3):277–283, June 2009.

[93] Pier Paolo Prosini, Maria Carewska, Stefano Loreti, Carla Minarini, and Stefano Passerini. Lithium iron oxide as alternative anode for li-ion batteries. *International Journal of Inorganic Material*, 2:365–370, 2000.

[94] Xiuyun Zhao, Dingguo Xia, and Kun Zheng. An Fe3O4FeOFe@C composite and its application as anode for lithium-ion battery. *Journal of Alloys and Compounds*, 513:460–465, February 2012.

[95] Xiayin Yao, Changlin Tang, Guoxia Yuan, Ping Cui, Xiaoxiong Xu, and Zhaoping Liu. Porous hematite (α-Fe2O3) nanorods as an anode material with enhanced rate capability in lithium-ion batteries. *Electrochemistry Communications*, 13(12):1439–1442, September 2011.

[96] a. M. Wilson, B. M. Way, J. R. Dahn, and T. van Buuren. Nanodispersed silicon in pregraphitic carbons. *Journal of Applied Physics*, 77(6):2363, 1995.

[97] Yan Yu, Lin Gu, Abirami Dhanabalan, Chun-Hua Chen, and Chunlei Wang. Three-dimensional porous amorphous SnO2 thin films as anodes for Li-ion batteries. *Electrochimica Acta*, 54(28):7227–7230, December 2009.

[98] Nikolay Dimov, Satoshi Kugino, and Masaki Yoshio. Carbon-coated silicon as anode material for lithium ion batteries: advantages and limitations. *Electrochimica Acta*, 48(11):1579–1587, May 2003.

[99] J Sarradin, A Guessous, and M Ribes. Synthesis and characterization of lithium intercalation electrodes based on iron oxide thin films. *Journal of power sources*, 7753(October 1995), 1996.

[100] Suqing Wang, Jingying Zhang, and Chunhua Chen. Fe3O4 submicron spheroids as anode materials for lithium-ion batteries with stable and high electrochemical performance. *Journal of Power Sources*, 195(16):5379–5381, August 2010.

[101] Yanna NuLi, Rong Zeng, Peng Zhang, Zaiping Guo, and Huakun Liu. Controlled synthesis of α-Fe2O3 nanostructures and their size-dependent electrochemical properties for lithium-ion batteries. *Journal of Power Sources*, 184(2):456–461, October 2008.

[102] Yanna NuLi, Peng Zhang, Zaiping Guo, P. Munroe, and Huakun Liu. Preparation of α-Fe2O3 submicro-flowers by a hydrothermal approach and their electrochemical performance in lithium-ion batteries. *Electrochimica Acta*, 53(12):4213–4218, May 2008.

[103] Yunhua Xu, Guoqiang Jian, Yihang Liu, Yujie Zhu, Michael R. Zachariah, and Chunsheng Wang. Superior electrochemical performance and structure

evolution of mesoporous Fe2O3 anodes for lithium-ion batteries. *Nano Energy*, 3:26–35, January 2014.

[104] L. Wang, H.W. Xu, P.C. Chen, D.W. Zhang, C.X. Ding, and C.H. Chen. Electrostatic spray deposition of porous Fe2O3 thin films as anode material with improved electrochemical performance for lithiumion batteries. *Journal of Power Sources*, 193(2):846–850, September 2009.

[105] AS Aricò, Peter Bruce, and Bruno Scrosati. Nanostructured materials for advanced energy conversion and storage devices. *Nature materials*, 4(May):366, 2005.

[106] Hongyu Mi, Youlong Xu, Wei Shi, Hyun-deog Yoo, Oh B. Chae, and Seung Mo Oh. Flocculant-assisted synthesis of Fe2O3/carbon composites for superior lithium rechargeable batteries. *Materials Research Bulletin*, 47(1):152–155, January 2012.

[107] L. Wang, Y. Yu, P.C. Chen, D.W. Zhang, and C.H. Chen. Electrospinning synthesis of C/Fe3O4 composite nanofibers and their application for high performance lithium-ion batteries. *Journal of Power Sources*, 183(2):717–723, September 2008.

[108] Yang He, Ling Huang, Jin-Shu Cai, Xiao-Mei Zheng, and Shi-Gang Sun. Structure and electrochemical performance of nanostructured Fe3O4/carbon nanotube composites as anodes for lithium ion batteries. *Electrochimica Acta*, 55(3):1140–1144, January 2010.

[109] Zhong-shuai Wu, Wencai Ren, Lei Wen, Libo Gao, Jinping Zhao, Zongping Chen, Guangmin Zhou, Feng Li, and Hui-ming Cheng. Graphene anchored with co(3)o(4) nanoparticles as anode of lithium ion batteries with enhanced reversible capacity and cyclic performance. *ACS nano*, 4(6):3187–94, June 2010.

[110] Yukun Wang, Lichun Yang, Renzong Hu, Liuzhang Ouyang, and Min Zhu. Facile Synthesis of Fe2O3-graphite Composite with Stable Electrochemical Performance as Anode Material for Lithium Ion Batteries. *Electrochimica Acta*, 125:421–426, April 2014.

[111] Ying Zhou and George V Franks. Flocculation mechanism induced by cationic polymers investigated by light scattering. *Langmuir : the ACS journal of surfaces and colloids*, 22(16):6775–86, August 2006.

[112] Guanglei Cui, Yong-Sheng Hu, Linjie Zhi, Dongqing Wu, Ingo Lieberwirth, Joachim Maier, and Klaus Müllen. A one-step approach towards carbon-encapsulated hollow tin nanoparticles and their application in lithium batteries. *Small (Weinheim an der Bergstrasse, Germany)*, 3(12):2066–9, December 2007.

[113] Bui Thi Hang, Takayuki Doi, Shigeto Okada, and Jun-ichi Yamaki. Effect of carbonaceous materials on electrochemical properties of nano-sized Fe2O3-loaded carbon as a lithium battery negative electrode. *Journal of Power Sources*, 174(2):493–500, December 2007.

[114] Bui Thi Hang, Shigeto Okada, and Jun-ichi Yamaki. Effect of binder content on the cycle performance of nano-sized Fe2O3-loaded carbon for use as a lithium battery negative electrode. *Journal of Power Sources*, 178(1):402–408, March 2008.

[115] K S Novoselov, a K Geim, S V Morozov, D Jiang, Y Zhang, S V Dubonos, I V Grigorieva, and a a Firsov. Electric field effect in atomically thin carbon films. *Science (New York, N.Y.)*, 306(5696):666–9, October 2004.

[116] A K Geim and K S Novoselov. The rise of graphene. *Nature materials*, 6(3):183–91, March 2007.

[117] Meryl D Stoller, Sungjin Park, Yanwu Zhu, Jinho An, and Rodney S Ruoff. Graphene-based ultracapacitors. *Nano letters*, 8(10):3498–502, October 2008.

[118] Arava Leela Mohana Reddy, Anchal Srivastava, Sanketh R Gowda, Hemtej Gullapalli, Madan Dubey, and Pulickel M Ajayan. Synthesis of nitrogen-doped graphene films for lithium battery application. *ACS nano*, 4(11):6337–42, November 2010.

[119] Xuan Wang, Linjie Zhi, and Klaus Müllen. Transparent, conductive graphene electrodes for dye-sensitized solar cells. *Nano letters*, 8(1):323–7, January 2008.

[120] Jung-Hwan Jung, Jin-Han Jeon, Vadahanambi Sridhar, and Il-Kwon Oh. Electro-active grapheneNafion actuators. *Carbon*, 49(4):1279–1289, April 2011.

[121] F Schedin, a K Geim, S V Morozov, E W Hill, P Blake, M I Katsnelson, and K S Novoselov. Detection of individual gas molecules adsorbed on graphene. *Nature materials*, 6(9):652–5, September 2007.

[122] Mauricio Terrones, Olga Martín, María González, Javier Pozuelo, Berna Serrano, Juan C. Cabanelas, Sofía M. Vega-Díaz, and Juan Baselga. Interphases in Graphene Polymer-based Nanocomposites: Achievements and Challenges. *Advanced Materials*, 23(44):5302–5310, November 2011.

[123] Vadahanambi Sridhar and Il-Kwon Oh. A coagulation technique for purification of graphene sheets with graphene-reinforced PVA hydrogel as byproduct. *Journal of colloid and interface science*, 348(2):384–7, August 2010.

[124] Changgu Lee, Xiaoding Wei, Jeffrey W Kysar, and James Hone. Measurement of the elastic properties and intrinsic strength of monolayer graphene. *Science (New York, N.Y.)*, 321(5887):385–8, July 2008.

[125] Francesco Bonaccorso, Antonio Lombardo, Tawfique Hasan, Zhipei Sun, Luigi Colombo, and Andrea C. Ferrari. Production and processing of graphene and 2d crystals. *Materials Today*, 15(12):564–589, December 2012.

[126] Chaohe Xu, Binghui Xu, Yi Gu, Zhigang Xiong, Jing Sun, and X. S. Zhao. Graphene-based electrodes for electrochemical energy storage. *Energy & Environmental Science*, 6(5):1388, April 2013.

[127] Guoxiu Wang, Xiaoping Shen, Jane Yao, and Jinsoo Park. Graphene nanosheets for enhanced lithium storage in lithium ion batteries. *Carbon*, 47(8):2049–2053, July 2009.

[128] Peng Guo, Huaihe Song, and Xiaohong Chen. Electrochemical performance of graphene nanosheets as anode material for lithium-ion batteries. *Electrochemistry Communications*, 11(6):1320–1324, June 2009.

[129] Seung-min Paek, Eunjoo Yoo, and Itaru Honma. Enhanced cyclic performance and lithium storage capacity of SnO2/graphene nanoporous electrodes with three-dimensionally delaminated flexible structure. *Nano letters*, 9(1):72–5, January 2009.

[130] Elad Pollak, Baisong Geng, Ki-Joon Jeon, Ivan T Lucas, Thomas J Richardson, Feng Wang, and Robert Kostecki. The interaction of Li+ with single-layer and few-layer graphene. *Nano letters*, 10(9):3386–8, September 2010.

[131] Peichao Lian, Xuefeng Zhu, Shuzhao Liang, Zhong Li, Weishen Yang, and Haihui Wang. Large reversible capacity of high quality graphene sheets as an anode material for lithium-ion batteries. *Electrochimica Acta*, 55(12):3909–3914, April 2010.

[132] Hailiang Wang, Li-Feng Cui, Yuan Yang, Hernan Sanchez Casalongue, Joshua Tucker Robinson, Yongye Liang, Yi Cui, and Hongjie Dai. Mn3O4-graphene hybrid as a high-capacity anode material for lithium ion batteries. *Journal of the American Chemical Society*, 132(40):13978–80, October 2010.

[133] Kara Evanoff, Alexandre Magasinski, Junbing Yang, and Gleb Yushin. Nanosilicon-Coated Graphene Granules as Anodes for Li-Ion Batteries. *Advanced Energy Materials*, 1(4):495–498, July 2011.

[134] Hailiang Wang, Yuan Yang, Yongye Liang, Li-Feng Cui, Hernan Sanchez Casalongue, Yanguang Li, Guosong Hong, Yi Cui, and Hongjie Dai. LiMn(1-x)Fe(x)PO4 nanorods grown on graphene sheets for ultrahigh-rate-performance lithium ion batteries. *Angewandte Chemie (International ed. in English)*, 50(32):7364–8, August 2011.

[135] Haegyeom Kim, Sung-Wook Kim, Jihyun Hong, Hee-Dae Lim, Hyung Sub Kim, Jung-Keun Yoo, and Kisuk Kang. Graphene-Based Hybrid Electrode Material for High-Power Lithium-Ion Batteries. *Journal of The Electrochemical Society*, 158(8):A930, August 2011.

[136] Seong-Min Bak, Kyung-Wan Nam, Chang-Wook Lee, Kwang-Heon Kim, Hyun-Chul Jung, Xiao-Qing Yang, and Kwang-Bum Kim. Spinel

LiMn2O4/reduced graphene oxide hybrid for high rate lithium ion batteries. *Journal of Materials Chemistry*, 21(43):17309, October 2011.

[137] Hailiang Wang, Yuan Yang, Yongye Liang, Joshua Tucker Robinson, Yanguang Li, Ariel Jackson, Yi Cui, and Hongjie Dai. Graphene-wrapped sulfur particles as a rechargeable lithium-sulfur battery cathode material with high capacity and cycling stability. *Nano letters*, 11(7):2644–7, July 2011.

[138] Oscar Vargas, Álvaro Caballero, Julián Morales, Giuseppe Antonio Elia, Bruno Scrosati, and Jusef Hassoun. Electrochemical performance of a graphene nanosheets anode in a high voltage lithium-ion cell. *Physical chemistry chemical physics : PCCP*, 15(47):20444–6, December 2013.

[139] Jusef Hassoun, Francesco Bonaccorso, Marco Agostini, Marco Angelucci, Maria Grazia Betti, Roberto Cingolani, Mauro Gemmi, Carlo Mariani, Stefania Panero, Vittorio Pellegrini, and Bruno Scrosati. An advanced lithium-ion battery based on a graphene anode and a lithium iron phosphate cathode. *Nano letters*, 14(8):4901–6, August 2014.

[140] Baojun Li, Huaqiang Cao, Jin Shao, Meizhen Qu, and Jamie H. Warner. Superparamagnetic Fe3O4 nanocrystals@graphene composites for energy storage devices. *Journal of Materials Chemistry*, 21(13):5069, 2011.

[141] Yuqin Zou, Jin Kan, and Yong Wang. Fe 2 O 3 -Graphene Rice-on-Sheet Nanocomposite for High and Fast Lithium Ion Storage. *The Journal of Physical Chemistry C*, 115(42):20747–20753, October 2011.

[142] M. P. Seah and W. A. Dench. Quantitative electron spectroscopy of surfaces: A standard data base for electron inelastic mean free paths in solids. *Surface and Interface Analysis*, 1(1):2–11, 1979.

[143] S Hüfner. *Photoelectron Spectroscopy: Principles and Applications.* Springer, 2003.

[144] C. N. Berglund and W. E. Spicer. Photoemission Studies of Copper and Silver: Experiment. *Physical Review*, 136(4A):A1044–A1064, November 1964.

[145] C. Berglund and W. Spicer. Photoemission Studies of Copper and Silver: Theory. *Physical Review*, 136(4A):A1030–A1044, November 1964.

[146] R. Courths and S. Hüfner. Photoemission experiments on copper. *Physics Reports*, 112(2):53–171, October 1984.

[147] Joachim Stöhr. *NEXAFS Spectroscopy*. 1992.

[148] Guenter Schmid. Large clusters and colloids. Metals in the embryonic state. *Chemical Reviews*, 92(8):1709–1727, December 1992.

[149] Michael L. Steigerwald and Louis E. Brus. Semiconductor crystallites: a class of large molecules. *Accounts of Chemical Research*, 23(6):183–188, June 1990.

[150] A Huczko. Template-based synthesis of nanomaterials. *Applied Physics A: Materials Science & Processing*, 70(4):365–376, April 2000.

[151] Greta R Patzke, Frank Krumeich, and Reinhard Nesper. Oxidic nanotubes and nanorods–anisotropic modules for a future nanotechnology. *Angewandte Chemie (International ed. in English)*, 41(14):2446–61, July 2002.

[152] A. P. Alivisatos. Semiconductor Clusters, Nanocrystals, and Quantum Dots. *Science*, 271(5251):933–937, February 1996.

[153] PEIDONG YANG, YIYING WU, and RONG FAN. INORGANIC SEMICONDUCTOR NANOWIRES. *International Journal of Nanoscience*, 01(01):1–39, February 2002.

[154] J Hu, Li Ls, W Yang, L Manna, Wang Lw, and a P Alivisatos. Linearly polarized emission from colloidal semiconductor quantum rods. *Science (New York, N.Y.)*, 292(5524):2060–3, June 2001.

[155] V F Puntes, K M Krishnan, and a P Alivisatos. Colloidal nanocrystal shape and size control: the case of cobalt. *Science (New York, N.Y.)*, 291(5511):2115–7, March 2001.

[156] Zhiyong Tang, Nicholas a Kotov, and Michael Giersig. Spontaneous organization of single CdTe nanoparticles into luminescent nanowires. *Science (New York, N.Y.)*, 297(5579):237–40, July 2002.

[157] R Andrew McMillan, Chad D Paavola, Jeanie Howard, Suzanne L Chan, Nestor J Zaluzec, and Jonathan D Trent. Ordered nanoparticle arrays formed on engineered chaperonin protein templates. *Nature materials*, 1(4):247–52, December 2002.

[158] a.L. Rogach, D.V. Talapin, E.V. Shevchenko, a. Kornowski, M. Haase, and H. Weller. Organization of Matter on Different Size Scales: Monodisperse Nanocrystals and Their Superstructures. *Advanced Functional Materials*, 12(10):653–664, October 2002.

[159] X Peng, L Manna, W Yang, J Wickham, E Scher, A Kadavanich, and Ap Alivisatos. Shape control of CdSe nanocrystals. *Nature*, 404(6773):59–61, March 2000.

[160] C. B. Murray, C. R. Kagan, and M. G. Bawendi. Self-Organization of CdSe Nanocrystallites into Three-Dimensional Quantum Dot Superlattices. *Science*, 270(5240):1335–1338, November 1995.

[161] Ralph Ulrich, Alexander Du Chesne, Markus Templin, and Ulrich Wiesner. Nano-objects with Controlled Shape, Size, and Composition from Block Copolymer Mesophases. *Advanced Materials*, 11(2):141–146, February 1999.

[162] C A Mirkin, R L Letsinger, R C Mucic, and J J Storhoff. A DNA-based method for rationally assembling nanoparticles into macroscopic materials. *Nature*, 382(6592):607–9, August 1996.

[163] Günter Schmid, Monika Bäumle, Marcus Geerkens, Ingo Heim, Christoph Osemann, and Thomas Sawitowski. Current and future applications of nanoclusters. *Chemical Society Reviews*, 28(3):179–185, January 1999.

[164] Y. Lei, L. D. Zhang, G. W. Meng, G. H. Li, X. Y. Zhang, C. H. Liang, W. Chen, and S. X. Wang. Preparation and photoluminescence of highly ordered TiO[sub 2] nanowire arrays. *Applied Physics Letters*, 78(8):1125, 2001.

[165] L. Sun, P. C. Searson, and C. L. Chien. Electrochemical deposition of nickel nanowire arrays in single-crystal mica films. *Applied Physics Letters*, 74(19):2803, 1999.

[166] Jeremy Sloan, David M. Wright, Sam Bailey, Gareth Brown, Andrew P. E. York, Karl S. Coleman, Malcolm L. H. Green, John L. Hutchison, and Hee-Gweon Woo. Capillarity and silver nanowire formation observed in single walled carbon nanotubes. *Chemical Communications*, (8):699–700, January 1999.

[167] A. Govindaraj, B. C. Satishkumar, Manashi Nath, and C. N. R. Rao. Metal Nanowires and Intercalated Metal Layers in Single-Walled Carbon Nanotube Bundles. *Chemistry of Materials*, 12(1):202–205, January 2000.

[168] Hongjie Dai, Eric W. Wong, Yuan Z. Lu, Shoushan Fan, and Charles M. Lieber. Synthesis and characterization of carbide nanorods. *Nature*, 375(6534):769–772, June 1995.

[169] Brett E. Lewis and Vern L. Schramm. Glucose Binding Isotope Effects in the Ternary Complex of Brain Hexokinase Demonstrate Partial Relief of Ground-State Destabilization. *Journal of the American Chemical Society*, 125(16):4672–4673, April 2003.

[170] Kake Zhu, Bin Yue, Wuzong Zhou, and Heyong He. Preparation of three-dimensional chromium oxide porous single crystals templated by SBA-15. *Chemical Communications*, (1):98–99, December 2003.

[171] Zongtao Zhang, Sheng Dai, Douglas A. Blom, and Jian Shen. Synthesis of Ordered Metallic Nanowires inside Ordered Mesoporous Materials through Electroless Deposition. *Chemistry of Materials*, 14(3):965–968, March 2002.

[172] Nicholas R. B. Coleman, Niall O'Sullivan, Kevin M. Ryan, Timothy A. Crowley, M. A. Morris, Trevor R. Spalding, David C. Steytler, and Justin D. Holmes. Synthesis and Characterization of Dimensionally Ordered Semiconductor Nanowires within Mesoporous Silica. *Journal of the American Chemical Society*, 123(29):7010–7016, July 2001.

[173] Nicholas R. B. Coleman, M. A. Morris, Trevor R. Spalding, and Justin D. Holmes. The Formation of Dimensionally Ordered Silicon Nanowires within Mesoporous Silica. *Journal of the American Chemical Society*, 123(1):187–188, January 2001.

[174] Hongkyu Kang, Young-wook Jun, Jong-Il Park, Kyung-Bok Lee, and Jin-woo Cheon. Synthesis of Porous Palladium Superlattice Nanoballs and Nanowires. *Chemistry of Materials*, 12(12):3530–3532, December 2000.

[175] Atsushi Fukuoka, Yuzuru Sakamoto, Shiyou Guan, Shinji Inagaki, Nori-aki Sugimoto, Yoshiaki Fukushima, Kaori Hirahara, Sumio Iijima, and Masaru Ichikawa. Novel Templating Synthesis of Necklace-Shaped Mono- and Bimetallic Nanowires in Hybrid OrganicInorganic Mesoporous Material. *Journal of the American Chemical Society*, 123(14):3373–3374, April 2001.

[176] Kwangyeol Lee, Yong-Ho Kim, Soo Bong Han, Hongkyu Kang, Soyoung Park, Won Seok Seo, Joon T. Park, Bongsoo Kim, and Sukbok Chang. Osmium Replica of Mesoporous Silicate MCM-48: Efficient and Reusable Catalyst for Oxidative Cleavage and Dihydroxylation Reactions. *Journal of the American Chemical Society*, 125(23):6844–6845, June 2003.

[177] Yuri Plyuto, Jean-Marc Berquier, Catherine Jacquiod, and Christian Ricolleau. Ag nanoparticles synthesised in template-structured mesoporous silica films on a glass substrate. *Chemical Communications*, (17):1653–1654, January 1999.

[178] Zheng Liu, Yasuhiro Sakamoto, Tetsu Ohsuna, Kenji Hiraga, Osamu Terasaki, Chang Hyun Ko, Hyun June Shin, and Ryong Ryoo. TEM Studies of Platinum Nanowires Fabricated in Mesoporous Silica MCM-41. *Angewandte Chemie*, 39(17):3107–3110, September 2000.

[179] Michael H. Huang, Amer Choudrey, and Peidong Yang. Ag nanowire formation within mesoporous silica. *Chemical Communications*, (12):1063–1064, January 2000.

[180] Yong-Jin Han, Ji Man Kim, and Galen D. Stucky. Preparation of Noble Metal Nanowires Using Hexagonal Mesoporous Silica SBA-15. *Chemistry of Materials*, 12(8):2068–2069, August 2000.

[181] Chang Hyun Ko and Ryong Ryoo. Imaging the channels in mesoporous molecular sieves with platinum. *Chemical Communications*, (21):2467, January 1996.

[182] Michal Kruk, Mietek Jaroniec, Ryong Ryoo, and Sang Hoon Joo. Characterization of Ordered Mesoporous Carbons Synthesized Using MCM-48 Silicas as Templates. *The Journal of Physical Chemistry B*, 104(33):7960–7968, August 2000.

[183] An-hui Lu, Wolfgang Schmidt, Akira Taguchi, Bernd Spliethoff, Bernd Tesche, and Ferdi Schüth. Taking Nanocasting One Step Further: Replicating CMK-3 as a Silica Material. *Angewandte Chemie International Edition*, 41(18):3489–3492, September 2002.

[184] J. Yin and Z. Wang. Ordered Self-Assembling of Tetrahedral Oxide Nanocrystals. *Physical Review Letters*, 79(13):2570–2573, September 1997.

[185] Taeghwan Hyeon, Su Seong Lee, Jongnam Park, Yunhee Chung, and Hyon Bin Na. Synthesis of Highly Crystalline and Monodisperse Maghemite Nanocrystallites without a Size-Selection Process. *Journal of the American Chemical Society*, 123(51):12798–12801, December 2001.

[186] Stephen O'Brien, Louis Brus, and Christopher B. Murray. Synthesis of Monodisperse Nanoparticles of Barium Titanate: Toward a Generalized Strategy of Oxide Nanoparticle Synthesis. *Journal of the American Chemical Society*, 123(48):12085–12086, December 2001.

[187] Karin Moller and Thomas Bein. Inclusion Chemistry in Periodic Mesoporous Hosts. *Chemistry of Materials*, 10(10):2950–2963, October 1998.

[188] Bozhi Tian, Xiaoying Liu, Chengzhong Yu, Feng Gao, Qian Luo, Songhai Xie, Bo Tu, and Dongyuan Zhao. Microwave assisted template removal of siliceous porous materialsElectronic supplementary information (ESI) available: syntheses, XRD patterns, SEM image, Pb2+ extraction images, 29Si MAS NMR and TG curves. See http://www.rsc.org/suppdata/cc/b2/b202180c/. *Chemical Communications*, (11):1186–1187, May 2002.

[189] Onofrio M Maragó, Francesco Bonaccorso, Rosalba Saija, Giulia Privitera, Pietro G Gucciardi, Maria Antonia Iatì, Giuseppe Calogero, Philip H Jones, Ferdinando Borghese, Paolo Denti, Valeria Nicolosi, and Andrea C Ferrari. Brownian motion of graphene. *ACS nano*, 4(12):7515–23, December 2010.

[190] Mustafa Lotya, Yenny Hernandez, Paul J King, Ronan J Smith, Valeria Nicolosi, Lisa S Karlsson, Fiona M Blighe, Sukanta De, Zhiming Wang, I T McGovern, Georg S Duesberg, and Jonathan N Coleman. Liquid phase production of graphene by exfoliation of graphite in surfactant/water solutions. *Journal of the American Chemical Society*, 131(10):3611–20, March 2009.

[191] Yenny Hernandez, Valeria Nicolosi, Mustafa Lotya, Fiona M Blighe, Zhenyu Sun, Sukanta De, I T McGovern, Brendan Holland, Michele Byrne, Yurii K Gun'Ko, John J Boland, Peter Niraj, Georg Duesberg, Satheesh Krishnamurthy, Robbie Goodhue, John Hutchison, Vittorio Scardaci, Andrea C Ferrari, and Jonathan N Coleman. High-yield production of graphene by liquid-phase exfoliation of graphite. *Nature nanotechnology*, 3(9):563–8, September 2008.

[192] Felice Torrisi, Tawfique Hasan, Weiping Wu, Zhipei Sun, Antonio Lombardo, Tero S Kulmala, Gen-Wen Hsieh, Sungjune Jung, Francesco Bonaccorso, Philip J Paul, Daping Chu, and Andrea C Ferrari. Inkjet-printed graphene electronics. *ACS nano*, 6(4):2992–3006, April 2012.

[193] A. C. Ferrari, J. C. Meyer, V. Scardaci, C. Casiraghi, M. Lazzeri, F. Mauri, S. Piscanec, D. Jiang, K. S. Novoselov, S. Roth, and A. K. Geim. Raman Spectrum of Graphene and Graphene Layers. *Physical Review Letters*, 97(18):187401, October 2006.

[194] Toru Yamashita and Peter Hayes. Analysis of XPS spectra of Fe2+ and Fe3+ ions in oxide materials. *Applied Surface Science*, 254(8):2441–2449, February 2008.

[195] D.-Q. Yang and E Sacher. Characterization and Oxidation of Fe Nanoparticles Deposited onto Highly Oriented Pyrolytic Graphite, Using X-ray Photoelectron Spectroscopy. *The Journal of Physical Chemistry C*, 113(16):6418–6425, April 2009.

[196] J. Zaanen, C. Westra, and G. A. Sawatzky. Determination of the electronic structure of transition-metal compounds: 2p x-ray photoemission spectroscopy of the nickel dihalides. *Physical Review B*, 33(12):8060, 1986.

[197] F. M. F. de Groot, J. C. Fuggle, B. T. Thole, G. A. Sawatzky, and H.Petersen. Oxygen 1s x-ray-absorption edges of transition-metal oxides. *Physical Review B*, 40(8):5715–5723, 1989.

[198] Z Y Wu, S. Gota, F. Jollet, M. Pollak, M. Gautier-Soyer, and C. R. Natoli. Characterization of iron oxides by x-ray absorption at the oxygen K edge using a full multiple-scattering approach. *Physical Review B*, 55(4):2570–2577, 1997.

[199] Guido Ketteler, Werner Weiss, Wolfgang Ranke, and Robert Schlögl. Bulk and surface phases of iron oxides in an oxygen and water atmosphere at low pressure. *Physical Chemistry Chemical Physics*, 3(6):1114–1122, 2001.

[200] J Yeh and I Lindau. Atomic subshell photoionization cross sections and asymmetry parameters. *Atomic Data and Nuclear Data Tables*, 32(1):1–155, 1985.

[201] Lucile Martin, Hervé Martinez, Delphine Poinot, Brigitte Pecquenard, and Frédéric Le Cras. Comprehensive X-ray Photoelectron Spectroscopy Study of the Conversion Reaction Mechanism of CuO in Lithiated Thin Film Electrodes. *The Journal of Physical Chemistry C*, 117(9):4421–4430, March 2013.

[202] Ryan Thorpe, Sylvie Rangan, Mahsa Sina, Frederic Cosandey, and Robert A Bartynski. Conversion Reaction of CoO Polycrystalline Thin Films Exposed to Atomic Lithium. *The Journal of Physical Chemistry C*, 117:14518, 2013.

[203] D. Larcher, D. Bonnin, R. Cortes, I. Rivals, L. Personnaz, and J.-M. Tarascon. Combined XRD, EXAFS, and Mossbauer Studies of the Reduction by Lithium of α-Fe2O3 with Various Particle Sizes. *Journal of The Electrochemical Society*, 150(12):A1643, 2003.

[204] N. Holzwarth, S. Rabii, L. Girifalco, and Number Io. Theoretical study of lithium graphite. I. Band structure, density of states, and Fermi-surface properties. *Physical Review B*, 18(10):5190–5205, November 1978.

[205] Z. Hu, A. Ignatiev, and P Hu. Lithium adsorption on the graphite (0001) surface. *Physical Review B*, 30(8):4856–4859, October 1984.

[206] G.K. Wertheim, P.T.Th.M. Van Attekum, and S. Basu. Electronic structure of lithium graphite. *Solid State Communications*, 33(11):1127–1130, 1980.

[207] S. Basu, C. Zeller, P.J. Flanders, C.D. Fuerst, W.D. Johnson, and J.E. Fischer. Synthesis and properties of lithium-graphite intercalation compounds. *Materials Science and Engineering*, 38(3):275–283, 1979.

[208] V.Z. Mordkovich. Synthesis and XPS investigation of superdense lithium-graphite intercalation compound, LiC2. *Synthetic Metals*, 80(3):243–247, July 1996.

[209] R.I.R Blyth, H Buqa, F.P Netzer, M.G Ramsey, J.O Besenhard, P Golob, and M Winter. XPS studies of graphite electrode materials for lithium ion batteries. *Applied Surface Science*, 167(1-2):99–106, October 2000.

[210] N. Holzwarth, L. Girifalco, S. Rabii, and Numerical Methods. Theoretical study of lithium graphite. II. Spatial distribution of valence electrons. *Physical Review B*, 18(10):5206–5216, November 1978.

[211] Tsutomu Ohzuku. Formation of Lithium-Graphite Intercalation Compounds in Nonaqueous Electrolytes and Their Application as a Negative Electrode for a Lithium Ion (Shuttlecock) Cell. *Journal of The Electrochemical Society*, 140(9):2490, September 1993.

[212] GN Bondarenko, VA Nalimova, and OV Fateev. Vibrational spectra of superdense lithium graphite intercalation compounds. *Carbon*, 36(7):1107–1112, 1998.

[213] R. Yazami and Ph. Touzain. A reversible graphite-lithium negative electrode for electrochemical generators. *Journal of Power Sources*, 9(3):365–371, 1983.

[214] J. R. Dahn, T. Zheng, Y. Liu, and J. S. Xue. Mechanisms for Lithium Insertion in Carbonaceous Materials. *Science*, 270(5236):590–593, October 1995.

[215] Nam Han, Tran Viet Cuong, Min Han, Beo Deul Ryu, S Chandramohan, Jong Bae Park, Ji Hye Kang, Young-jae Park, Kang Bok Ko, Hee Yun

Kim, Hyun Kyu Kim, Jae Hyoung Ryu, Y S Katharria, Chel-jong Choi, and Chang-hee Hong. Improved heat dissipation in gallium nitride light-emitting diodes with embedded graphene oxide pattern. *Nature Communications*, 4:1452–1458, 2013.

[216] Silvano Lizzit, Guillermo Zampieri, Luca Petaccia, Rosanna Larciprete, Paolo Lacovig, EmileD.L. Rienks, Gustav Bihlmayer, Alessandro Baraldi, and Philip Hofmann. Band dispersion in the deep 1s core level ofgraphene. *Nature Physics*, 6(5):345–349, March 2010.